University of São Paulo | University of Stuttgart
Institute of Physics | Institute for Theoretical Physics I

Quantum cooling:
thermodynamics and information

Rodolfo R. Soldati

Doctoral thesis submitted in cotutelle to the University of São Paulo and the University of Stuttgart in partial fulfillment of the requirements for the degree of Doctor of Natural Sciences.

University of Stuttgart

Main reviewer: Prof. Dr. Eric Lutz

Co-reviewer: Prof. Dr. Maria Daghofer

Prof. Dr. Tilman Pfau

University of São Paulo

Co-reviewer: Prof. Dr. Gabriel Teixeira Landi

Prof. Dr. André de Pinho Vieira

Dr. Alessio Belenchia

Date of defense: 9th of October 2023

2023

FICHA CATALOGRÁFICA
Preparada pelo Serviço de Biblioteca e Informação
do Instituto de Física da Universidade de São Paulo

Abstract

The theory of cooling is an important corner of thermodynamics, under-
lying many modern technological applications. As the field of quantum
thermodynamics advances, refrigeration techniques must keep pace to fuel
the innovations of quantum technologies. We study quantum cooling from
its foundations to laboratory implementations within the specific paradigm
of heat bath algorithmic cooling. Our study includes a detail modeling of
experimental imperfections and establishes the fundamental cooling limits
of the model, consolidating the algorithm as a viable quantum refrigeration
method. Next, by developing the notion of virtual qubits, we demonstrate
a cooling-boost protocol fueled by quantum coherences which is robust
to experimental implementations. Aiming at aiding in the progress of
refrigeration technologies, we conclude by studying the zero temperature
equilibrium properties of a many-body system that can accommodate an
autonomous quantum absorption refrigerator, and calculate its entanglement
and critical properties, two features that, like quantum coherences, promise
to improve the performance of quantum coolers.

Keywords: Heat-bath Algorithmic Cooling; Quantum coherences; Virtual
qubits; Dicke model; Entanglement.

Resumo

A teoria do refrigeração é um importante pilar da termodinâmica, subjacente a muitas aplicações tecnológicas modernas. Conforme o campo da termodinâmica quântica avança, as técnicas de refrigeração devem acompanhar o ritmo para impulsionar as inovações das tecnologias quânticas. Estudamos o resfriamento quântico desde suas bases até as implementações em laboratório, começando pela técnica de heat-bath algorithmic cooling. Esse estudo inclui modelagem de imperfeições experimentais, estabelecendo os limites de resfriamento conhecidos que se aplicam a esse regime e consolidando o algoritmo como um método de refrigeração eficiente. Em seguida, ao desenvolver a noção de qubits virtuais, demonstramos um protocolo, robusto contra implementações experimentais, que melhora técnicas usuais de arrefecimento e é provido por coerências quânticas. Com o objetivo de contribuir para o avanço das tecnologias de refrigeração, concluímos estudando as propriedades de equilíbrio a temperatura zero de um sistema de muitos corpos que pode acomodar um refrigerador de absorção quântica autônomo, e calculamos suas propriedades críticas e de emaranhamento, dois traços que, assim como coerência quântica, podem ser usados no aprimoramento da performance de refrigeradores quânticos.

Palavras-chave: Arrefecimento algorítmico; Coerências quânticas; Qubits virtuais; Emaranhamento.

Deustche Zusammenfassung

Die Theorie des Kühlens ist eine wichtige Säule der Thermodynamik und bildet die Grundlage für viele moderne technologische Anwendungen. Mit dem Fortschreiten der Quantenthermodynamik müssen Kälte- und Kühlungstechniken Schritt halten, um Innovationen in den Quantentechnologien voranzutreiben. Wir untersuchen die Quantenkühlung von ihren Grundlagen bis hin zu Implementierungen im Labor, innerhalb des Paradigmas des Wärmebadkühlens. Unsere Arbeit beinhaltet ein detailierte Modellierung experimenteller Unvollkommenheiten und etabliert dabei bereits bekannte Schranken des Kühlens womit wir den Algorithmus als eine praktikable Quantenkühlmethode etablieren. Indem wir dann das Konzept von virtuellen Qubits entwickeln, demonstrieren wir anschließend ein Kühl-Boost-Protokoll, das durch Quantenkoherenzen getrieben wird und zudem robust gegenüber experimentellen Unvollkommenheiten ist. Mit dem Ziel, den Fortschritt der Kältetechnologien zu unterstützen, schließen wir dann mit der Untersuchung der Gleichgewichtseigenschaften eines Vielteilchensystems am Temperaturnullpunkt, das über eine autonome quantenmechanische Absorptionskühlmaschine verfügt. Wir berechnen die Verschränkungs- und kritischen Eigenschaften, zwei Merkmale, die wie Quantenkoherenzen Aussichten haben, die Leistung von quantenmechanischen Kühlsystemen zu verbessern.

Acknowledgements

A special thank you to Monika, for being a constant and always kind and friendly presence in the institute; for making the hardships of being a Brazilian living in Germany more manageable, more than simply navigating the bureaucracy but in being *the* human side in the cold of university administration. Your commitment to your principles is inspiring.

Finally, I am exceptionally grateful for my partner and significant other, Bruna, with whom I have spent most of my time during my Ph.D., and hopefully with whom I will share my time for many years to come. I am thankful for your friendship, your great personality, your support, your intuition, your ability in physics, your engagement; for being a part in all the contexts I have mentioned above; and for all the other things we share, both describable and indescribable.

Contents

vi

Contents

List of Figures

List of Tables

Chapter 0

Introduction

Background and motivation

The preparation of pure states is paramount to make quantum technologies functional, and in particular for quantum computers [1–3]. Achieving high fidelity initialization of a multiqubit register to the computational state $|00\ldots0\rangle$ is the first step towards computation, and is important to the extent of being classified as one of the main drives towards the construction of large-scale quantum computers, e.g. summarized in the second of DiVincenzo's criteria [1]. These efforts happen concurrently to the engineering of computation taking place away from error-inducing dynamics in decoherence-free subspaces [4–7], or inside noiseless subsystems [8–10], and in addition to the active implementation of quantum error-correction [11, 12].

In DiVincenzo's criteria [1] and subsequent characterizations [3], cooling in various forms is explicitly mentioned as principal approaches on the

way to the goal of producing low entropy fiducial states. Refrigeration is thus the backdrop for the realization of experiments at large, as we now recognize its necessity in modern cutting-edge applications, and notice its presence in the drive for more precise clocks [13], preparation of cold and ultracold many-body states for simulations or otherwise general use in precision control and measurement of quantum states [14–19].

A quantum refrigerator that is in special connection to the development of quantum computers is algorithmic cooling, first introduced in [20, 21]. At the same time it can be framed as a quantum thermal machine, it is inherently an algorithmic procedure and thus, in a sense, a computational task itself. Furthermore, it is an experimentally realizable procedure [22, 23].

Originally proposed in the advent of NMR ensemble quantum computing proposal [20–22], algorithmic cooling aimed at preparing an effective lower dimensional quantum subsystem, from the large thermal bath state, that would be closer to the ground state and amenable to be used in quantum computing tasks. It was later realized that for this approach to work, it would necessitate a large supply of these effective qubits in low enough temperatures, and for them to be stored away from decoherence effects.

Fault-tolerance estimates placed heavy constrains and were an impediment to this approach. The ability to refrigerate multiqubit registers on-the-fly seemed more promising, as was later demonstrated [24, 25]. In this installment, termed heat-bath algorithmic cooling (HBAC), the cooling takes place over a cycle of operations involving an environment that is separately arranged. The computational qubits are the target of a unitary gate that has heat-bath qubits also as inputs, but that are then discarded in preparation for the next cycle; in this sense, the cooling of the target happens in an open-systems setting. This stands in contrast to the original proposal, where bulk refrigeration of the ensemble of qubits (e.g. the liquid-state

NMR ensemble) was followed by a unitary that initialized the target qubits. Experimental realizations of HBAC [26, 27] face naturally occurring difficulties matching with the idealized model. Motivated by these efforts, we enrich these studies by modelling the algorithm with realistic imperfections taken into account, and we use this opportunity to find ways to enhance its performance as a refrigerator.

Moving on from the focus on controlling quantum systems, we will consider an autonomous quantum refrigerator [28–31]. In contrast to the design of controlled systems such as HBAC, an absorption refrigerator, working autonomously, evolves and performs cooling on a cold heat bath free of external interactions besides the ones required to set up the platform in the first place. The first designs of an absorption refrigerator dates back two centuries, and a notable following improvement is due to Einstein and Szilárd, for an absorption refrigerator with no moving parts [32], and later in refs. [33–35], which are early contributions to quantum thermodynamics. The working principle behind such as system is the exchange of a work source (the external control device, such as a knob at the hand of the experimentalist that tunes a laser), for a third heat bath to be placed in addition to the cold bath, from where the heat is extracted, and the hot both, to where that heat is being transferred. This extra heat bath, termed the work reservoir that typically seats at a temperature even higher than the hot bath, is used as the system induces the cold-to-hot heat transport by coupling this process to concomitant transport of heat from the work reservoir to the hot bath. The motivation behind working with autonomous systems, particularly coolers, is both to provide better accounting of the thermodynamic costs of these devices, and to discard "moving parts" in the engineering of these devices, which are precisely the sources of noise and error as they are made smaller and thus more subject to fluctuations.

Experimental implementations of a quantum absorption refrigerator have only now started to appear [28, 29], and are constrained to few-body physics. To advance the field further, particularly in the direction of large scale devices, and the search and exploit of quantum advantage, we will study a many-body model displaying interesting quantum matter features in this thesis.

Outline of the thesis. We start with chapter 1, based on [36], describing fairly general cooling limits, focusing on a particular implementation of algorithmic cooling, known as Heat-Bath Algorithmic Cooling (HBAC). Algorithmic cooling is a particularly minimal implementation of a refrigerator that allows one to keep track of many controllable parameters as it acts on qubits. By being initially defined in terms of two-level systems, it is suited for studies of quantum state preparation, highlighting its usefulness for quantum computing devices and related technologies. In this first chapter we do a thermodynamic analysis of HBAC, more comprehensive than what has been done in the past [37], and on top of an actual experimental implementation of its minimal version in an NV center setup.

In chapter 2, following [38], we extend this description uncovering the virtual qubit nature of the resources used for cooling the target qubit in algorithmic cooling. With this understanding, we propose how to include genuinely quantum resources, and we suggest a conservative procedure to use up these resources with the goal of taking the target system even closer to the ground state, thus showing how to circumvent the original idea of previously proposed universal cooling limits.

Next, in chapter 3, from [39], we end the thesis by moving our focus to the more intricate platform of interacting spin-boson systems, where collective behavior, phases of matter and many-body physics are key underlying

concepts. The well-established Dicke model, often useful in quantum optics and atomic physics [40–42], will serve us in a study of equilibrium properties of a system amenable to the autonomous absorption refrigerator design. The Dicke model originally consists of a large number of d-level systems collectively coupled to a single bosonic mode. We will analyze an extension of it that includes a new bosonic mode coupled to a new degree-of-freedom of the already existing d-level systems. At the thermodynamic limit we show that the collective coupling can be simplified in a mean-field approach to a system of three interacting harmonic oscillators. This extended model enjoys the same properties at equilibrium as the original model, now with two independent normal-to-superradiant phase transitions. In addition, we show that the region separating the two superradiant phases breaks a continuous symmetry and thus gives rise to a gapless, Goldstone mode. We end devise a correlation profile of the system at equilibrium, where multipartite entanglement is present.

Chapter 1

Quantum cooling, algorithmically

1.1 Introduction to heat-bath algorithmic cooling

One of the main tasks for which algorithmic cooling was designed is to prepare the states in a multiqubit register as close as possible to the computational state $|00\ldots0\rangle$, where $|0\rangle$ is the ground state of each qubit. The algorithm receives as input a string of mixed two-level states ρ_s, and outputs a second string of mixed states ρ'_s in higher fidelity to $|00\ldots0\rangle$. This procedure entails in purification of the states of the composite register towards the ground state, or in other words, cooling.

We distinguish in this process the target system ρ_s, to be cooled, and the resources that will be used to that end. One of the main resources in the

algorithm is an ensemble of qubits drawn from a heat bath, ρ_a, which will be termed *reset* or *ancilla* qubits. The scaling of both resource and performance with the number of qubits (heat bath or target) is of great importance, but we focus on the minimal working example in this introduction, and leave the discussion of these resources to the end of this section. Our main result in this chapter also concerns the three-qubit minimal model, which is the building block for the larger models. We thus restrict ourselves for the moment to heat-bath algorithmic cooling with one target qubit and two ancilla qubits.

In the minimal HBAC, the input is the single-qubit state $\rho_s = \rho_1$, for the target qubit, and the algorithm uses as resource the state ρ_2 and ρ_3 for the ancillas. Jointly they form a global uncorrelated state $\rho_{123} = \rho_1 \otimes (\rho_2 \otimes \rho_3)$.[a] A unitary channel $\mathcal{U}$ that compresses entropy and energy from the target qubit to the ancilla qubits determines one cycle of refrigeration that ends with a reset of the ancilla states. The joint entropy of these three states is maintained in this process but the target qubit is cooled, at the same time the ancillas are heated.

For the purpose of explaining the algorithm, it is sufficient to consider the effects of the algorithm on the population of each of the qubit's state, namely the diagonal components of their density matrices in a certain basis. Looking forward to actual physical implementations where these states are thermal, we assume the density matrices to be diagonal and written in the energy eigenbasis:

$$\rho_b = \begin{pmatrix} p_{b(0)} & 0 \\ 0 & p_{b(1)} \end{pmatrix}, \tag{1.1}$$

where 0 indicates the ground state and 1 the excited state of each of the

---

[a]We will sometimes omit partition subscripts such as 123 when referring to global states.

$b = 1, 2, 3$ qubits.

The goal with heat-bath algorithmic cooling is to dynamically take the population of the target qubit, $p_{b(0)}$, as close as possible to its ground-state value of 1 (as $p_{b(1)}$ goes to 0). As we could expect from the third law of thermodynamics, we will see that this approach is limited; we will quantify this limitation and analyze the resources that need to be taken into account for better performance.

The choice of compression unitary channel $\mathcal{U}$ enjoys some freedom. The algorithmic nature of this protocol can be made explicit by treating the finite-dimensional three-qubit state as an array of numbers. Let us for now assume that the ancilla qubits share the same population, indicated by q_0 and q_1, and take the target population to be given by p_0 and p_1. A standard choice of constructing the global state gives, for the diagonal elements of ρ_{123},

$$\rho_{123} = \mathrm{diag}(p_i q_j q_k), \tag{1.2}$$

where the matrix is arranged in lexicographic order.[b]

The thermodynamic assumption that the target system, to be cooled, is initially in a temperature at least equal to that of the ancilla qubits, and that every temperature is positive, applies here. In terms of the populations, this means that we have the following order at step $n = 0$:

$$0 < q_1(0) \leq p_1(0) < p_0(0) \leq q_0(0), \tag{1.3}$$

meaning that the reset qubits start in a state comparatively chiller than the target. From this, the question that algorithmic cooling addresses is: what sorting of the numbers $p_i q_j q_k$ can be made such that, upon updating the

---

[b]Lexicographic order: $000, 001, 010, 011, 100, 101, 110, 111$.

p value, we get $p_0(n) \lesssim p_0(n+1)$? The answer to this question is then encoded in the compression unitary channel $\mathcal{U}$, that takes the shape of a permutation matrix.

We remark here that it is not necessary to restrict the unitary channel to be equal for every sorting step, but for our purposes of studying the minimal HBAC implementation, this simplifying assumption can be made and is desirable from an implementation perspective.

The purpose of this step, that we identify as a thermodynamic cycle of a refrigerator, is to draw resources from the heat bath to cool the target, as we increase its ground state population. In terms of the array of numbers $p_i q_j q_k$, we want to increase the array entries for which $i = 0$, that defines the new target ground state:

$$p_{i'}(n+1) = \sum_{j',k' \in \{0,1\}} p_{i'j'k'}(n+1), \qquad (1.4)$$

where $p_{i'j'k'}(n+1) = p_{i'}(n)q_{j'}q_{j'}$ and $i'j'k' = u(ijk)$ is given by the permutation u implemented through the action of $\mathcal{U}$ on ρ_{123}. This statement has then the clear interpretation in quantum mechanics as

$$\rho_1(n+1) = \text{tr}_{23}\{U\rho_{123}(n)U^\dagger\}, \qquad (1.5)$$

where U are the unitary operators defining the channel as $\mathcal{U}(\rho) = U\rho U^\dagger$. The reset qubits are similarly affected in this process, with their state evolving as $\tilde{\rho}_{23} = \text{tr}_1\{U\rho_{123}(n)U^\dagger\}$, with updated populations $\tilde{q}_0$ and $\tilde{q}_1$.

The simplest unitary that achieves the goal of cooling the target qubit implements the transition $|011\rangle\langle100| + \text{h.c.}$ The implemented permutation exchanges the smaller value $p_0(n)q_1^2$ for the larger $p_1(n)q_0^2$, given the hierarchy eq. (1.3). In updating the state of the target qubit for the next
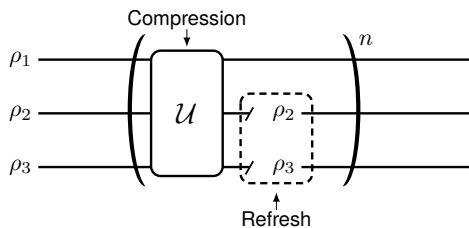
Figure 1.1: Circuit diagram for the minimal HBAC.

cycle, $\rho_1(n) \mapsto \rho_1(n+1)$, the new ground state population is given by eq. (1.4) and thereby increased.

In fig. 1.1 we show a circuit diagram of the minimal heat bath algorithmic cooling. The input mixed states and their evolution are represented in full lines, and unitary gates (for us, the compression unitary), are shown in blocks. What was described above determines what happens within a single cycle of refrigeration. The conditions, however, can be applied repeatedly, as the updated state can still satisfy them. To finalize the description of the algorithm we introduce the refresh operation, shown in fig. 1.1 inside a dashed block, which is what distinguishes it. This channel is non-unitary, and responsible for the possibility of concatenating the cycles.

After updating the target qubit populations, the reset step exchanges the now heated ancilla qubits for a fresh new set of qubits prepared identically to the previous ones, now discarded. The resulting map is $\tilde{q}_j \mapsto q_j$. This reset then creates a new array of numbers that defines the global updated state at the nth cycle $\rho_{123}(n+1)$.

The repeated application of compression and refresh over the three-qubit state finally defines all steps of HBAC. At each iteration, the target is cooled if the conditions (1.3) apply. This dynamical evolution reaches a steady

state, where the target qubit is no longer cooled, with its population reaching a fixed point, meaning that the update that follows the permutation keeps p_i unaffected. At this point the cooling limit of HBAC has been reached.

Cooling limits. The lowest temperatures achieved depend on defining parameters of instances of the algorithm, even though the algorithm can in principle be implemented in various physical platforms. In our example, these parameters appear in the number of reset qubits and in their initial populations, but not the choice of compression unitary. For instance, another unitary that could be applied in the explained setting would be one where other permutations take place among the numbers $0jk$. Although this changes the dynamics, the steady state is maintained.

The cooling limit has been determined and refined in many instances [25, 43–46], and are believed to be general in the regime of classical thermal states (i.e. in the absence of quantum coherences) [47, 48]. In addition to what has been studied here, these results also include memory qubits[c] [46, 49], which are also cooled but stand in contrast to the target in that they are cooled to a lesser extent in a cascading decreasing order.

These limits can be measured in terms of the polarization of the qubits, namely the quantity

$$\varepsilon = \mathrm{tr}(Z\rho), \quad -1 \leq \varepsilon \leq 1, \tag{1.6}$$

where $Z = \left(\begin{smallmatrix} 1 & 0 \\ 0 & -1 \end{smallmatrix}\right)$ is the diagonal Pauli matrix, which relates to the ground state population through the equality $\varepsilon = 2p_0 - 1$. In terms of polarizations, the cooling limit for a target qubit refrigerated by the application of heat-bath algorithmic cooling with m memory qubits and r reset qubits with reset

---

[c]Also known as scratch qubits.

polarization ε_a is [45]

$$\varepsilon_s(\infty) = \frac{(1+\varepsilon_a)^{2^m r} - (1-\varepsilon_a)^{2^m r}}{(1+\varepsilon_a)^{2^m r} + (1-\varepsilon_a)^{2^m r}}, \tag{1.7}$$

in particular, for the minimal HBAC, the cooling limit is

$$\varepsilon_1(\infty) = \frac{2\varepsilon_a}{1+\varepsilon_a^2}, \tag{1.8}$$

where $m = 0$ and $r = 2$. Also recall that $\rho_s = \rho_1$.

In this few qubit setting, temperature can be mapped to the polarization measure. Assuming a Hamiltonian $H = -\omega Z/2$, a thermal state has a diagonal form in the energy eigenbasis, and can be written in terms of ε:

$$\rho = \frac{e^{-\beta H}}{\mathrm{tr}\, e^{-\beta H}} = \frac{1}{2}\begin{pmatrix} 1+\varepsilon & 0 \\ 0 & 1-\varepsilon \end{pmatrix}, \tag{1.9}$$

for the inverse temperature $\beta = 1/T$. In this parametrization, infinite temperature is the limit $\varepsilon \to 0$, and the ground state indicates zero temperature at $\varepsilon = 1$. The domain of negative temperatures [50–52], such as in population inversion phenomena, is tied to negative polarization, $\varepsilon < 0$; we will not deal with this regime in this thesis. The functional relation between polarization and temperature is given by

$$\varepsilon(\beta) = \tanh\left(\frac{\beta\omega}{2}\right), \quad \text{or} \quad \beta(\varepsilon) = \omega^{-1}\ln\left(\frac{1+\varepsilon}{1-\varepsilon}\right). \tag{1.10}$$

The corresponding temperature limits are then [45]

$$T_1(\infty) = \frac{1}{2^m r}\frac{\omega_1}{\omega_a}T_a, \tag{1.11}$$

where ω_1 is the gap of the target qubit and ω_a and T_a are the gap of the reset qubits, and respectively the temperature of the heat bath from which they are drawn.

To conclude this introduction we draw out a comparison of algorithmic cooling with what is known in the literature as the swap engine [53–56]. The swap engine is based on the swap unitary gate S, common in quantum computing applications. The gate acts on two qubits by simple exchange of states: $S(\rho(T_h)\otimes\rho(T_c))S^\dagger = \rho(T_c)\otimes\rho(T_h)$. The principle of refrigeration, in this case, is that the first system, starting at temperature $T_h > T_c$, is exchanged by the second system at a lower temperature. Refrigeration here is limited to temperatures of the available cold bath T_c. Heat-bath algorithmic cooling works very similarly to this engine, but then a question arises: why are the temperatures reached by HBAC lower than the provided fresh temperatures of the ancillas? The answer, as we will show in the next chapter, lies in the presence of the availability of two ancilla qubits, instead of the single cold qubit of the swap engine. This can be seen as a justification to why, for HBAC, the "minimal model" starts at three qubits. Before we elaborate on this further, we now describe our results concerning an experimental implementation of this minimal model, and its thermodynamic analysis.

Outline of the chapter. Heat-bath algorithmic cooling will be our focus on this chapter. Since it has been first proposed, it has been the subject of an extensive body of research considering its operational and fundamental limits in a variety of settings [20–26, 37, 43–49, 57–65]. We start with the next section by elaborating on the principles behind algorithmic cooling on a technical level, the observable quantities and parameters which have been studied previously in the literature and the type of system on which it is

applied. We end that section with a discussion of one of its most important measures of performance, the cooling limit, which answers the question: what are the lowest temperatures achieved by the ensuing dynamics?

We add our contribution to the literature and recent progress of algorithmic cooling starting in section 1.2 [36]. In this study, we analyze a recent experimental implementation of HBAC in a nitrogen-vacancy center that achieves and demonstrates the cooling limit for a minimal model [27] for many iterations. The dynamics of HBAC is solved analytically, with the physical sources of dissipation from an experiment taken into account; we thus generalize the cooling limit results to new parameter regimes.

Moreover, we analyze the algorithm as a refrigerator and compute thermodynamic figures of merit, namely the coefficient of performance and power, therefore going beyond what can be concluded from the cooling limit alone. We show that, as a refrigerator, the algorithm converges to the Carnot bound in the steady state, which is achieved after a few cycles. By uncovering the experimental sources of dissipation, we determine that the experimental implementation achieves the expected fundamental cooling limits despite being away from the idealized unitary regime in which the limits were determined. We thus establish that heat-bath algorithmic cooling is an efficient thermal machine that operates with high performance with currently available technology.

1.2 Algorithmic cooling and its thermodynamics

Towards a realistic model in a nitrogen-vacancy center. Cooling has been an important application of thermodynamics since its foundation. Refrigeration generically occurs when heat is extracted from a system, leading to a decrease of its entropy and a reduction of its temperature below that of the environment [66]. Efficient cooling methods are essential for the study of low-temperature quantum phenomena, from the physics of atoms and molecules [67, 68] to novel states of matter [69, 70] and the development of quantum technologies [71, 72].

As elaborated in the introduction, heat-bath algorithmic cooling is a method that allows to cool target qubits with the help of standard logic gates and reset qubits that pump entropy out of the target into a bath, which acts as an entropy sink [24, 25, 37, 43, 45, 60, 61, 73–77]. An algorithmic cooling cycle consists of a succession of (i) compression steps that cool the (slow-relaxing) target system and heat up the (fast-relaxing) reset ancillas, and of (ii) refresh steps during which the reset system quickly relax back to the bath temperature (fig. 1.2).

Algorithmic cooling refrigerators share similarities with conventional quantum refrigerators: they cyclically transfer heat from the cold spins to the hot bath by consuming work done by the quantum gates. Such analogy makes a comparison between the two refrigerators possible. However, their underlying cooling mechanisms are intrinsically different and the finite size of the target qubit results in a cycle that is not closed in the thermodynamic sense, since its state is not the same at the beginning and at the end of one cycle. Cyclic algorithmic cooling operation has recently been demonstrated experimentally for a minimal system of three qubits, using nuclear magnetic
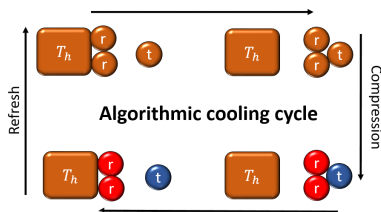
Figure 1.2: Schematic illustration of the minimal three-qubit algorithmic cooling cycle: in a first (compression) step, heat is extracted from the target qubit (t), cooling it down while heating up the two reset qubits (r). In a second (refresh) step, the reset qubits are rethermalized to the bath temperature T_h. Contrast this with the circuit diagram fig. 1.1. Here, we make explicit the coupling management of the physical bodies that house the qubits, and represent in color the temperature changes of each step, with the exception that the refresh simply redefines the output target state to be the new input state, with no further change of temperature.

resonance [26, 57, 78, 79] and nitrogen-vacancy centers in diamond [27].

Motivated by these experiments, we here make heat-bath algorithmic cooling composed of one target spin and of two reset spins [26, 27, 57, 78, 79] into a more realistic model and investigate its thermodynamic performance. We determine its fundamental limits in parallel to those of standard quantum refrigerators [31, 55, 80, 81].[d]

Conventional refrigerators cyclically pump heat from a cold to a hot macroscopic system (both considered as heat baths) by consuming work [66]. Two central figures of merit of such refrigerators are the cooling power that characterizes the rate of heat removal, ΔQ, and the coefficient of performance ζ, or COP, defined as the ratio of heat extracted from the target and work supplied, $\zeta = |Q|/W$.

The COP captures the energetic efficiency by measuring the amount of

---

[d]An information-theoretic analysis of the performance of heat-bath algorithmic cooling, viewed from the perspective of feedback cooling, has been presented in ref. [82].

heat extracted against the energy expenditure of work done on the system. In contrast to the efficiency (and its ultimate Carnot bound), the COP can attain values which are larger than 1. It is still however bounded from above: the maximum value of the COP is given, in the reversible limit, by the ideal Carnot expression, $\zeta_C = T_c/(T_h - T_c)$, where T_c and T_h are the respective temperatures of the cold and hot baths [66].

The Carnot bound can be derived for the present model starting from the definition of the coefficient of performance, $\zeta = |Q|/W$, and taking the heat to be the (quantum) average energy extracted from the target qubit, whereas the work is the total energy change of the target and ancilla systems over the controlled interaction. That is,

$$\zeta(n) = \frac{-\Delta\langle H_1 \rangle}{\Delta\langle H_1 \rangle + \Delta\langle H_a \rangle}, \tag{1.12}$$

where H_1 and H_a are the target and ancilla Hamiltonians and Δ is the forward difference of the averages over states $\rho(n+1)$ and $\rho(n)$ during the evolution. Here, we have defined heat and work as $Q(n) = \Delta\langle H_1 \rangle(n)$ (with the target average energy extracted being negative) and $W(n) = \Delta\langle H_1 \rangle(n) + \Delta\langle H_a \rangle(n)$, respectively. We also assume that both systems are at thermal equilibrium, i.e. are at a Gibbs states at temperature β_1 and β_a.

The fundamental assumption of the Carnot limit is that the process is reversible. This can be stated in terms of entropy production, defined by

$$\Sigma = \Delta S(\rho_1) + \beta_a Q_a, \tag{1.13}$$

where $S(\rho) = -\operatorname{tr}\{\rho \ln \rho\}$ is the von Neumann entropy and $Q_a = \Delta\langle H_a \rangle$ is the heat flowing into the bath from which the ancillas are extracted. The

process is then reversible when entropy production vanishes, which implies that

$$\Delta S(\rho_1) = -\beta_a Q_a. \tag{1.14}$$

In addition to the assumption of reversibility, we can then use the following identity[e] to rewrite the coefficient of performance:

$$\Delta \langle H \rangle_1 = T_1(n)[\Delta S(\rho_1) + S(\rho_1(n+1)||\rho_1(n))], \tag{1.15}$$

where and $S(\rho||\rho') = \text{tr}\{\rho(\ln \rho - \ln \rho')\}$ is the relative entropy between the two given states. Plugging this identity and then applying (1.14) we get for the COP

$$\zeta(n) = \frac{-T_1(n)[-\beta_a Q_a + S(\rho_1(n+1)||\rho_1(n))]}{T_1(n)[-\beta_a Q_a + S(\rho_1(n+1)||\rho_1(n))] + Q_a}, \tag{1.16}$$

which can finally be rewritten as

$$\zeta(n) = \frac{T_1(n) + T_1(n)\, T_a\, S(\rho_1(n+1)||\rho_1(n))/Q_a}{T_a - T_1(n) + T_1(n)\, T_a\, S(\rho_1(n+1)||\rho_1(n))/Q_a}. \tag{1.17}$$

This is the Carnot bound, given that $T_c = T_1(n \to \infty)$ and $T_h = T_a$, and provided that $S(\rho_1(n+1)||\rho_1(n))/Q_a \xrightarrow{n \to \infty} 0$. In practice, both $S(\rho_1(n+1)||\rho_1(n))$ and Q_a vanish at the steady state, but we can expect that the ratio will indeed converge to zero, since larger systems typically converge to the steady state at a slower rate than smaller ones, and by design the ancilla system in heat-bath algorithmic cooling is larger than the target. This is also what we will verify later in this chapter through explicit

---

[e]This identity can be verified by writing the entropy definitions explicitly for a thermal state.

calculations. We concluded that

$$\zeta_C = \zeta(\infty) = \frac{T_1(\infty)}{T_a - T_1(\infty)}. \tag{1.18}$$

The performance of thermal machines coupled to finite baths with finite heat capacities may be conveniently analyzed with cycle-dependent quantities [83–88]. In the following, we compute COP, cooling power and polarization of the target qubit per cycle for an arbitrary number of cycle iterations. We employ Liouville space techniques [89] to exactly solve the full nonstationary dynamics of the system. While heat-bath algorithmic cooling has been mostly studied in the unitary limit and under steady-state conditions [37, 43, 45, 73, 74, 76], we explicitly account for experimentally relevant external damping of the target qubit and for nonideal activation of logic gates [26, 27, 57, 78, 79], for arbitrary cycles numbers including the transient regime. We obtain explicit expressions for the fundamental upper bounds for COP and cooling power in the ideal reversible limit and compare the former to the ideal Carnot COP of a quantum refrigerator [31, 55, 80, 81]. We finally experimentally determine the performance of the minimal algorithmic cooling refrigerator using three qubits in a nitrogen-vacancy (NV) center in diamond [27] and obtain values of COP and cooling power that are close to their fundamental bounds.

1.2.1 Quantum algorithmic cooling refrigerator: modeling gate errors

We consider the minimal three-qubit heat-bath algorithmic cooling refrigerator. We take each qubit's Hamiltonian to be $H_i = -\omega_i Z^i/2$, $i = 1, 2, 3$, where ω_i is the energy gap between the energy eigenstates of the diagonal

Pauli operator $Z^i = \left(\begin{smallmatrix} 1 & 0 \\ 0 & -1 \end{smallmatrix}\right)$ of the ith qubit, leading to the full Hamiltonian, which is the sum of the individual ones, $H = \sum_i H_i$. Qubit 1 is the target spin while qubits 2 and 3 are the two reset spins. Motivated by the experiments, we restrict to all energy gaps being equal and equal to unit, $\omega_i = 1$. Finally, the machine starts in a separable state of the three qubits,

$$\rho(0) = \rho_1(0) \otimes \rho_2(0) \otimes \rho_3(0), \qquad (1.19)$$

with respective density matrices

$$\rho_i(0) = \frac{I}{2} + \frac{\varepsilon_i(0)}{2} Z^i = \frac{1}{2} \begin{pmatrix} 1 + \varepsilon_i(0) & 0 \\ 0 & 1 - \varepsilon_i(0) \end{pmatrix}, \qquad (1.20)$$

and polarizations $\varepsilon_i(0) = \operatorname{tr} Z^i \rho_i(0)$.

The algorithm consists of two stages for each cycle, which is the typical engineering of the heat bath version [24, 37, 43, 45, 60, 61, 73–76]. The first is the compression unitary[f]

$$U = \begin{pmatrix} I_3 & & & \\ & 0 & -i & \\ & -i & 0 & \\ & & & I_3 \end{pmatrix} \qquad (1.21)$$

$$= -i(|011\rangle\langle100| + \text{h.c.}) + \sum_{ijk \neq 011,100} |ijk\rangle\langle ijk|,$$

after which we denote the qubit states by $\tilde{\rho}_i(n)$ at the nth iteration. For instance, $\tilde{\rho}_2(0) = \operatorname{tr}_{13}\{U\rho(0)U^\dagger\}$. The compression is then followed by

[f]That can also be written as $I_3 \oplus (-iX_{011}^{100}) \oplus I_3$, where X_{011}^{100} is the X Pauli matrix in that three-qubit subspace.

the refresh step of qubits 2 and 3, at which point we define the next cycle, with updated state

$$\begin{aligned} \rho(n+1) &= \mathcal{R}[\tilde{\rho}(n)] \\ &= \text{tr}_{23}\{\tilde{\rho}(n)\} \otimes \rho_2(0) \otimes \rho_3(0) \\ &= \tilde{\rho}_1(n) \otimes \rho_2(0) \otimes \rho_3(0). \end{aligned} \tag{1.22}$$

Notice that from this follows that $\rho_1(n+1) = \tilde{\rho}_1(n)$, since the refresh step does not affect the target. Using similar notation for the polarizations, we get that $\varepsilon_1(n+1) = \tilde{\varepsilon}_1(n)$, but most importantly that $\varepsilon_2(n) = \varepsilon_2(0)$, by the definition of the refresh, even though $\tilde{\varepsilon}_2(n+1) \neq \tilde{\varepsilon}_2(n)$ (and similarly for qubit 3). To simplify notation, we set $\varepsilon_2(0) = \varepsilon_2$ and $\varepsilon_3(0) = \varepsilon_3$.

We next identify the heat $Q(n)$ extracted during round n with the average energy change of the target qubit, $Q(n) = \text{tr}\{\omega_1 Z^1[\rho_1(n+1) - \rho_1(n)]\}$. We further associate the work performed by the logic gates on the system with the corresponding mean energy variation before the refresh, $W(n) = \sum_{i=2,3} \text{tr}\{\omega_i Z^i[\tilde{\rho}_i(n) - \rho_i(n)]\}$ [37]. The COP per cycle, $\zeta(n)$, is then defined as the ratio of pumped heat and applied work, while the cooling power per cycle, $J(n)$, is given (in units of the cycle time) as the discrete derivative (or forward difference) of the heat:

$$\zeta(n) = \frac{-Q(n)}{W(n)} \quad \text{and} \quad J(n) = Q(n+1) - Q(n). \tag{1.23}$$

These are the principal quantities of our investigation.

We shall examine the thermodynamic properties of heat-bath algorithmic cooling in the general case where compression is implemented with imperfect gates and the (slow-relaxing) target spin is subjected to

irreversible energy dissipation.[g] We will discard irreversible losses of the reset spins because of their much faster relaxation. For each round n of the cooling protocol, we accordingly describe the evolution of the system with the help of three quantum channels [71]. We first account for energy dissipation of the target qubit via an amplitude damping channel $\mathcal{D}$ with decay rate γ [71],

$$\mathcal{D}[\rho] = \sum_{j=1,2} \Gamma_j \rho \Gamma_j^\dagger, \tag{1.24}$$

with the two Kraus damping operators,

$$\Gamma_1 = \begin{pmatrix} 1 & 0 \\ 0 & \sqrt{1-\gamma} \end{pmatrix} \quad \text{and} \quad \Gamma_2 = \begin{pmatrix} 0 & \sqrt{\gamma} \\ 0 & 0 \end{pmatrix}. \tag{1.25}$$

We further characterize the imperfect compression stage with the channel $\tilde{\rho}(n) = \mathcal{K}[\rho(n-1)]$, such that,

$$\mathcal{K}[\rho] = \sum_{\mu=1,2} K_\mu \rho K_\mu^\dagger, \tag{1.26}$$

where we have introduced the two quantum operators,

$$K_1 = \frac{I}{\sqrt{2}} - \frac{1}{\sqrt{2}}(|011\rangle\langle 011| + |100\rangle\langle 100|) - i\sin(\theta)(|011\rangle\langle 100| + \text{h.c.}),$$

$$\tag{1.27a}$$

$$K_2 = \frac{I}{\sqrt{2}} + \left(\cos\theta - \frac{1}{\sqrt{2}}\right)|011\rangle\langle 011| + \left(\cos\theta - \frac{1}{\sqrt{2}}\right)|100\rangle\langle 100|.$$

$$\tag{1.27b}$$

---

[g]An abstract error analysis of heat-bath algorithmic cooling has been performed in ref. [75].

Here $|0\rangle$ and $|1\rangle$ are the eigenstates of the spin operators Z^i (the ground and excited states of the Hamiltonian) and I denotes the identity operator in non-exchange subspace. The angle θ quantifies the failure probability of the compression step to take place. When $\theta = \pi/2$, we recover the ideal compression which swaps the desired diagonal elements of the density matrix, and where we take to stem from a generating interaction Hamiltonian, $U = \exp(-i\pi H_{123}/2)$ with $H_{123} = |100\rangle\langle 011| + |011\rangle\langle 100|$ [45], that is turned on and off at the appropriate times. The compression operation is commonly implemented experimentally with Toffoli or CNOT gates with imperfect fidelity, which leads θ to deviate from the ideal value $\pi/2$ [26, 27, 57, 78, 79]. The composition of the above two channels, plus the refresh $\mathcal{R}$, yields the combined quantum operation $\mathcal{C}$ which corresponds to one round of the refrigeration algorithm.

In the definition of the probabilistically activated compression, given by channel $\mathcal{K}$, one further assumption is made. Acting on energy-diagonal states, $\mathcal{K}$ can also take the operator-sum form with Kraus operators $\tilde{K}_1 = \cos(\theta)I$ and $\tilde{K}_2 = \sin(\theta)U$, which is an unital channel formed by the convex combination of unitaries I and U with probability distribution $(\cos^2\theta, \sin^2\theta)$. However, the form given above ignores initial coherences in the qubit states. That our results match the experimental numbers can then be seen as a further indication that the imperfect channel implementation also depletes initially present coherences in the setup (see section 1.3.3 for more details).

1.2.2 Main analytical results: dynamics, cooling power and coefficient of performance

We analytically solve the dynamics generated by the quantum channel $\mathcal{C}$ for an arbitrary number n of algorithmic cooling cycles, using vectorization techniques in Liouville space [89], also known as natural representation [90]. In this approach, a density matrix ρ is mapped one-to-one to the vector vec ρ (often called supervector). In terms of bras and kets, vectorization is defined as the following map:

$$\rho = \sum_{i,j} \rho_{ij} \,|i\rangle\langle j| \mapsto \mathrm{vec}(\rho) = \sum_{i,j} \rho_{ij} \,|i\rangle|j\rangle, \tag{1.28}$$

where the index i is varied first, and vec ρ now has the shape of a column matrix. As a shorthand, we also introduce the notation $\vec{\rho} = \mathrm{vec}\,\rho$. A generic quantum channel, with operator-sum representation $\mathcal{E}[\rho] = \sum_\mu E_\mu \rho E_\mu^\dagger$, will then act on the state through left matrix multiplication, being represented by[h]

$$\Phi_\mathcal{E} = \sum_\mu E_\mu \otimes (E_\mu^\dagger)^\mathsf{T}. \tag{1.29}$$

To recover the original representation, the compatibility correspondence is used: $\mathcal{E}[\rho] = \mathrm{unvec}(\Phi_\mathcal{E}\,\mathrm{vec}(\rho))$.

The advantage of the Liouville space representation is that n iterations of the cooling cycle may be simply evaluated by computing $\Phi_\mathcal{E}^n$; in contrast, in the bras and kets representation, the repeated evolution involves following all n-fold permutations of repeated applications of the Kraus operators, $E_\alpha E_\beta \dots E_\delta$, acting on both sides of the density matrix, and generating the

---

[h]The tensor product symbol and the transposition $(|i\rangle\langle j|)^\mathsf{T} = |j\rangle\langle i|$ are the same ones used in the usual algebra of bras and kets.

stochastic trajectories (see appendix A). Using this formalism, we obtain explicit expressions for the polarization of the target qubit, as well as for heat and work, from which we deduce COP and cooling power (1.23) for each cycle, for arbitrary initial polarizations of the three qubits (see section 1.3.2).

The two figures of merit, COP and cooling power, have closed analytical expression for any set of parameters γ and θ, and initial conditions $(\varepsilon_1(0), \varepsilon_2(0) = \varepsilon_3(0) = \varepsilon)$. We show below these expressions for the experimentally relevant case of $\varepsilon_1(0) = 0$ [26, 27, 57, 78, 79], corresponding to a state at large temperatures. The COP is given by

$$\zeta(n) = \frac{A(\varepsilon, \gamma, \theta)e^{-ng(\theta,\gamma)}}{B(\varepsilon, \gamma, \theta)e^{-ng(\theta,\gamma)} + 16(1 + \varepsilon)^2\gamma\sin^2\theta} \tag{1.30}$$

where

$$A(\varepsilon, \gamma, \theta) = [2\gamma(1 + \cos^2\theta) - 2\varepsilon(2 + \gamma\varepsilon)\sin^2\theta][(1 - \gamma)f(\theta) - 4]$$
$$B(\varepsilon, \gamma, \theta) = [(\gamma - 1)(f(\theta) + 4(\varepsilon^2 + 1)\sin^2\theta) + 4]$$
$$\times [\gamma f(\theta) + 2\varepsilon(\cos(2\theta) - 1)]$$

$$\tag{1.31}$$

given

$$f(\theta) = 3 + (1 + \varepsilon^2)\cos(2\theta) - \varepsilon^2. \tag{1.32}$$

The cooling power is given by

$$J(n) = \frac{1}{16}[(\gamma - 1)f(\theta) + 4][4\varepsilon\sin^2\theta - \gamma f(\theta)]e^{-ng(\theta,\gamma)}, \tag{1.33}$$

where we have defined the decay factor $g(\theta, \gamma) = \ln[4/((1 - \gamma)f(\theta))]$.

The maximal value for these figures of merit are reached for zero

damping, $\gamma = 0$. The COP is unaffected by the mixing angle θ, with

$$\zeta(n) \xrightarrow{\gamma=0} \zeta_{\max}(n) = 1. \tag{1.34}$$

The cooling power, on the other hand, changes, and we introduce a protocol θ_n aiming at maximizing the heat extracted at each step, with $\theta_n = \pi/2$ for $n < 2$, $\varepsilon < 1/\sqrt{3}$ and

$$\theta_n = \frac{1}{2} \arccos \left[\frac{2\varepsilon^2 + n\varepsilon^2 + n - 6}{(2+n)(1+\varepsilon^2)} \right] \tag{1.35}$$

otherwise.[i] With this, the reversible limit for the cooling power is

$$J(n) \xrightarrow[\theta=\theta_n]{\gamma=0} J_{\max}(n) = \frac{\varepsilon}{2}(1+\varepsilon^2)e^{-ng(\theta_n,0)}. \tag{1.36}$$

Results for general polarizations are given in the next sections.

Figure 1.3(ab) represent $\zeta(n)$ and $J(n)$ as a function of the cycle number n for various values of the decay rate γ and of the mixing angle θ. We first note that both quantities reach their fundamental maximum values in the undamped limit $\gamma = 0$. In this unitary, reversible regime, the COP $\zeta(n)$ is equal to one, implying that the extracted heat is precisely given by the work supplied by the gate operations, $-Q(n) = W(n)$ (when $\gamma = 0$). The value of $\zeta_{\max}(n)$ is moreover independent of the cycle number n and of the angle θ. This interesting point reveals that the probabilistic activation of the unitary compression does not affect the maximum efficiency of the algorithmic cooling refrigerator, only reducing the power $J_{\max}(n)$. We further observe that the cooling power generically decays exponentially to zero with increasing cycle iterations, as the asymptotic temperature is

---

[i]See section 1.3.2 for a full characterization.

reached and no more heat can be extracted from the target qubit—a behavior also exhibited by $\zeta(n)$ in the presence of irreversible losses. Figure 2b additionally shows that $J(n)$ is mostly affected by the angle θ and not so much by the decay rate γ in the experimentally relevant range $\gamma < 0.01$. In particular, the optimal angle θ_n in $J_{\max}(n)$ depends on n for $n \geq 2$.[j]

The dynamics of HBAC, as demonstrated in fig. 1.3, is of unique fixed point for any target qubit initial state. In the thermal regime, where the target is kept in a state diagonal in the energy basis at all times, the evolution from the infinite temperature state displays a transient regime at the first few cycles, $n = o(1)$, where the algorithm deviates from the classical thermodynamic interpretation of a refrigerator. Still at small n, the target qubit thermalizes to the heat bath of reset qubits, from which point onwards HBAC functions as a regular refrigerator.

Two important features of the algorithmic cooling protocol are the asymptotic polarization of the target qubit and the number of iterations needed to reach it [25, 60, 74]. Using the Liouville space solution, we find the exact expression (again for $\varepsilon_1(0) = 0$, $\varepsilon_2(0) = \varepsilon_3(0) = \varepsilon$),

$$\varepsilon_1(n) = \frac{\gamma f(\theta) + 2\varepsilon[\cos(2\theta) - 1]}{(\gamma - 1)f(\theta) + 4}[e^{-ng(\theta,\gamma)} - 1]$$

$$\xrightarrow[\theta = \pi/2]{\gamma = 0} \varepsilon_{1\max}(n) = \frac{2\varepsilon}{1 + \varepsilon^2}[1 - e^{-ng(\pi/2,0)}]. \quad (1.37)$$

The stationary value $\varepsilon_1(\infty)$ is thus approached exponentially with a rate constant given by $1/g(\theta, \gamma)$. Figure 1.3(c) displays a radically different effect of energy dissipation and of gate imperfection on the nonideal polarization of the target qubit. While the decay constant γ affects the

---

[j]The decreasing values of θ_n with the cycle number n reduce the rate of exponential decay $g(\gamma, \theta)$ of the power $J(n)$ at each step towards the steady state.
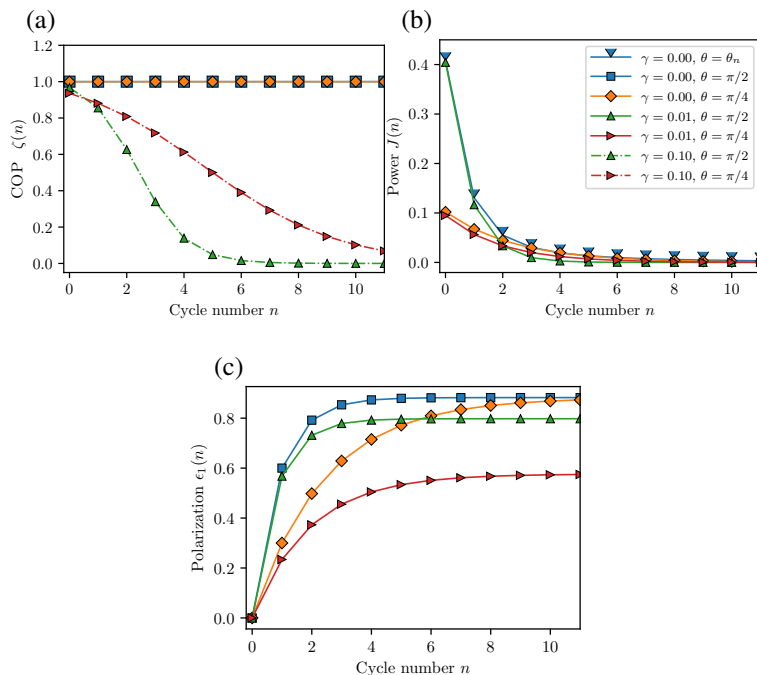
Figure 1.3: Thermodynamic performance of the algorithmic cooling refrigerator per cycle. (a) Coefficient of performance $\zeta(n)$, eq. (1.30), (b) Cooling power $J(n)$, eq. (1.33), and (c) Polarization of the target qubit $\varepsilon_1(n)$, eq. (1.37), for various values of the damping rate γ and of the mixing angle θ. These two parameters have radically different effects: whereas the decay constant affects the asymptotic value of the polarization, the mixing angle changes the convergence rate to that value. In addition, the behavior of the cooling power mostly depends on the mixing angle, while the COP depends on both variables. The fundamental upper bounds in the reversible limit ($\gamma = 0$) are shown by the blue squares. Parameters are $\varepsilon_1(0) = 0$, $\varepsilon_2(0) = \varepsilon_3(0) = \varepsilon = 0.6$.

asymptotic value of the polarization $\varepsilon_1(\infty)$, the mixing angle θ modifies the convergence rate to that value for $\gamma = 0$. As a consequence, imperfect gate operation does not prevent achieving maximum polarization in the reversible limit, it only increases the number of required iterations. This property holds for all convex combinations of the ideal compression and the identity (cf. section 1.3.3).

Let us next compare the thermodynamic performance of the algorithmic cooling refrigerator to that of a conventional quantum refrigerator [31, 55, 80, 81], whose COP is upper bounded by the Carnot formula, $\zeta_C = T_c/(T_h - T_c)$. We accordingly evaluate, for each cycle n, the temperature of the target qubit via $T_c = T_1(n) = 1/\ln[(1 + \varepsilon_1(n))/(1 - \varepsilon_1(n))]$ and $T_h = T_2(0) = T_3(0)$, determined via the ratio of the (Boltzmann distributed) populations of excited and ground states. The corresponding Carnot COP per cycle, $\zeta_C(n) = T_1(n)/[T_h - T_1(n)]$ for the algorithmic cooling refrigerator is shown, together with the COP $\zeta(n)$, eq. (1.30), in fig. 1.4. While $\zeta(n)$ is smaller than $\zeta_C(n)$ at the beginning of the refrigeration cycle, the Carnot bound is quickly approached after only a few iterations in the ideal limit ($\gamma = 0, \theta = \pi/2$). The Carnot limit is in general not attained in the presence of damping ($\gamma \neq 0$).

1.2.3 Fitting the experimental data

We finally put our theoretical framework and predictions to the test by analyzing the performance of an algorithmic cooling refrigerator made of three nuclear spins that are hyperfine coupled to the central electron spin of a NV center in diamond [27]. NV center systems offer excellent control of their states and exhibit very long spin coherence times [91]. The target spin and the two reset spins are respectively chosen to be the nitrogen ^{14}N and
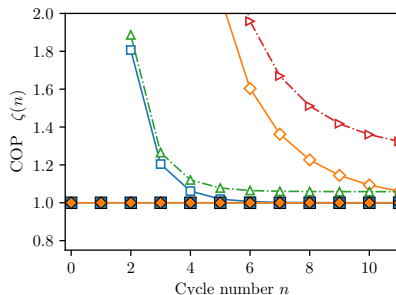
Figure 1.4: Comparison with the Carnot coefficient of performance. In the reversible regime ($\gamma = 0$), the coefficient of performance $\zeta(n)$ (full symbols) gets close to the corresponding Carnot limit $\zeta_C(n)$ (empty symbols) after a few cycles. The Carnot bound is generally not reached in the presence of losses ($\gamma \neq 0$). Same parameters as in fig. 1.3.

two carbon ^{13}C nuclear spins that are coupled to the central electron spin of the NV center with respective strengths 2.16MHz, 90kHz, and 414kHz (fig. 1.5). The central electron spin has a twofold role: it acts as (i) the heat bath and also as (ii) an ancillary spin that drives the interaction among the spins required to achieve the entropy compression on the target qubit [27]. The optical spin polarization of the central NV-spin is transferred to the two ^{13}C spins via a SWAP gate during the refresh steps (cf. appendix B). Compression is implemented by performing a non-local gate among the three nuclear spins that allow for a unitary mixing of populations in the subspace of $|011\rangle$ and $|100\rangle$ (see section 1.3.3). As the nuclear spins do not interact with each other, this three qubit Toffoli gate is mediated by the electron spin.

Typical times of each step are ~285µs for the compression step and ~285ms for the refresh step. The life-time of the nuclear spin, T_1, is of the order of seconds (corresponding to a decay rate $\gamma \approx 10^{-4}$), allowing
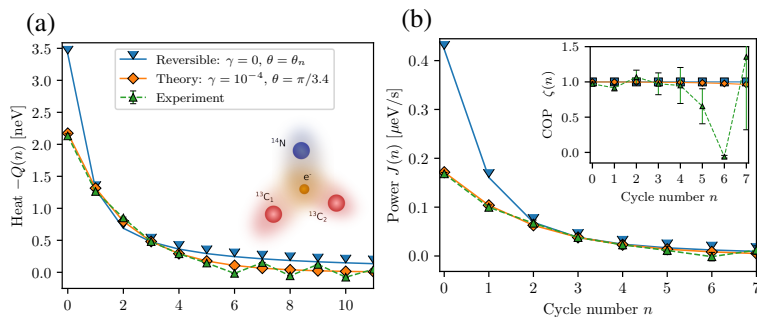
Figure 1.5: Experimental performance of the three-qubit algorithmic cooling refrigerator. (a) Experimental data for heat $Q(n)$ (green triangles) show excellent agreement with theory (orange diamond) with $\gamma = 10^{-4}$ and $\theta = \pi/3.4$. (b) Cooling power $J(n)$ and COP $\zeta(n)$ also agree very well with theory ($\zeta(n)$ becomes sensitive to measurement errors for larger n). Error bars correspond to the standard deviation.

us to perform multiple rounds of the cooling cycle. Since the refresh step periodically resets the two ^{13}C spins, their damping is not relevant over the duration of the experiment. Another source of noise, not considered in previous experiments [26, 57, 78, 79], is due to imperfect compression: the compression algorithm indeed utilizes three-qubit Toffoli gates [27], which when transpiled into the electron-nuclear spin gates, involve 5 CNOT gates and 14 single-qubit rotations. Gate imperfections, together with imperfect charge state initialization, lead to uncertain transitions between the states $|011\rangle$ and $|100\rangle$, which can be quantified by an effective mixing angle θ. The best fit in our experiment is $\theta \approx \pi/3.4$, which corresponds to an overall error of $\sim 20\%$ in the compression step. Reset is additionally implemented via an iterative SWAP gate that allows for a $\sim 99\%$ fidelity on the achievable hot spin polarization.

The initial polarizations of the two reset spins are $\varepsilon_2(0) \sim 0.58$ and $\varepsilon_3(0) \sim 0.41$. The imbalance between the polarizations comes from the different coupling strengths of the two spins to the electron spin. We measure the target spin polarization via single-shot readout with a fidelity of $\sim$97%, from which the heat $Q(n)$ and the cooling power $J(n)$ are evaluated, as well as work $W(n)$ and COP $\zeta(n)$ for each cycle.[k] We obtain excellent agreement between theory (with $\gamma = 10^{-4}$ and $\theta = \pi/3.4$) and data (fig. 1.5). We observe especially that the upper bounds $J_{\max}(n)$ and $\zeta_{\max}(n)$, given by eq. (1.30), are reached in the experiment. For $n \geq 5$, heat and work are very small. As a result, the COP becomes highly sensitive to measurement errors: it can get negative for $-Q(n)$ below zero (as for $n = 6$) or be larger than one if $W(n)$ is too close to zero (as for $n = 7$).

1.3 Methods

In this section we elaborate on the analytical solution of the dynamics of the three-qubit heat-bath algorithmic cooling refrigerator for arbitrary cycle number, mainly the target and reset qubit polarizations. We follow with the evaluation of heat, work, as well as cooling power and coefficient of performance for arbitrary initial conditions based on the exact dynamics. We then move on to discuss the general properties of the imperfect compression map, and we finalize with details on the data analysis of the thermodynamic performance of the refrigerator, and the experimental implementation of the cooling algorithm.

---

[k]With the Larmor frequency of the target spin (^{14}N) being $\sim$1.66MHz and a cycle time including compression and reset steps of about $\sim$5ms, the heat $Q(n)$ extracted per cycle is on the order of a few neV, and the power $J(n)$ is on the order of a few μeV s^{-1} or 1×10^{-26}W.

1.3.1 Full analytical solution of the dynamical model in Liouville space

This section presents the exact solution of the dynamics of the three-qubit system in Liouville space [89]. We refer to appendix C and refs. [89, 90, 92] for more details.

In order to evaluate the states of the target qubit and of the two reset qubits after an arbitrary number of refrigeration cycles n, we need to compute the matrix in Liouville space of the combined quantum channel consisting of damping $\mathcal{D}$, compression $\mathcal{K}$ and refresh $\mathcal{R}$ maps. Starting from the damping channel $\mathcal{D}[\rho] = \sum_j \Gamma_j \rho \Gamma_j^\dagger$, we can use its definition (1.25), and formula (1.29) to build the corresponding superoperator representation $\Phi_{\mathcal{D}} = \sum_j \Gamma_\mu \otimes (\Gamma_\mu^\dagger)^\intercal$, a 4-by-4 matrix acting on the target qubit subspace.

As a second step, we consider the compression channel, given by eq. (1.26). Since we are mainly interested in the evolution of the target qubit in this work, it suffices to consider the reduced compression channel

$$\mathcal{K}_{\text{red}}[\rho_1] = \text{tr}_{23}\left\{ \sum_{k=1,2} K_k\big(\rho_1 \otimes \rho_2(0) \otimes \rho_3(0)\big)K_k^\dagger\right\}, \qquad (1.38)$$

that acts on the target qubit space alone. In this procedure, the refresh channel acting on the ancillas is already taken into account when we take the tensor product with the reset qubit states, and then at the end trace them out. In fact, this reduced compression is the main body of our full cooling channel of interest as it acts on the target qubit; the only remaining part being composition with the amplitude-damping operation.

We determine the Kraus operators C_l of the operator-sum representation $\mathcal{K}_{\text{red}}[\rho] = \sum_l C_l \rho C_l^\dagger$ by extending the treatment that can be found in ref. [71], Section 8.2.3, to nonunitary operations. It involves introducing a

purification of the mixed state of reset qubits, that is, the map

$$\rho_2(0) \otimes \rho_3(0) \mapsto |\rho_2, \rho_3\rangle \in (\mathbf{H}_2 \otimes \mathbf{H}_3)^{\otimes 2}, \tag{1.39}$$

where

$$|\rho_2, \rho_3\rangle = \sum_{ij} |ij\rangle_{23} |ij\rangle_{23} \sqrt{\langle i|\rho_2|i\rangle \langle j|\rho_3|j\rangle}, \tag{1.40}$$

such that $\mathrm{tr}_{23} |\rho_2, \rho_3\rangle\langle\rho_2, \rho_3| = \rho_2(0) \otimes \rho_3(0)$, where the Hilbert space is doubled as part of the purification. By explicitly evaluating the trace and the purification, we find

$$C_{(k),ij}^{i'j'} = \langle i'j'|_{23} \langle ij|_{23} \left(K_k \otimes I \right) \sum_{rs} \sqrt{p_2^r p_3^s} |rs\rangle_{23} |rs\rangle_{23}, \tag{1.41}$$

where

$$p_2^r = \langle r|\rho_2|r\rangle, \quad p_3^s = \langle s|\rho_3|s\rangle. \tag{1.42}$$

The bras here stem from the trace while the sum over double-primed indices and their kets stem from the purified state. This leads to the operators

$$C_{(k),ij}^{i'j'} = \langle i'j'|K_k|ij\rangle \sqrt{p_2^i p_3^j}. \tag{1.43}$$

To simplify the notation, we group the indices i, j, i', j' and k, each binary, into the new index l ranging over 32 values, and thus yielding 32 operators C_l. Most of them are identically 0 through this procedure, however, with six others remaining for $k = 1$ and other four for $k = 2$. The corresponding superoperator $\Phi_{\mathcal{K}_{\mathrm{red}}}$ is again given by eq. (1.29).

The state of the target qubit, which is needed to determine every thermodynamic measure, such as heat and cooling power, of the heat-bath algorithmic cooling refrigerator, is obtained after concatenation of the two

maps $\mathcal{D}$ and $\mathcal{K}_{\mathrm{red}}$, which in vectorized form reads $\Phi_{\mathcal{K}_{\mathrm{red}}}\Phi_{\mathcal{D}}$. The target qubit states after a number n of cycles are then obtained by calculating $(\Phi_{\mathcal{K}_{\mathrm{red}}}\Phi_{\mathcal{D}})^n$. We find for arbitrary initial polarizations $\varepsilon_1(0)$, ε_2 and ε_3 that

$$\tilde{\rho}_1(n) = \mathrm{unvec}\left\{\left(\Phi_{\mathcal{K}_{\mathrm{red}}}\Phi_{\mathcal{D}}\right)^n \vec{\rho}_1(0)\right\} = \frac{1}{2}\begin{pmatrix} 1 - \varepsilon_1(n) & 0 \\ 0 & 1 + \varepsilon_1(n) \end{pmatrix},$$
(1.44)

with the polarization $\varepsilon_1(n)$ is here explicitly given by

$$\begin{aligned} \varepsilon_1(n) = \frac{1}{(\gamma-1)F(\theta)+4}\Big[& 2(\varepsilon_2 + \varepsilon_3)\sin^2\theta - \gamma F(\theta) \\ & + \big[2\sin^2\theta\big((1+\varepsilon_2\varepsilon_3)\varepsilon_1(0) - \varepsilon_2 - \varepsilon_3\big) \\ & + \gamma(1+\varepsilon_1(0))F(\theta)\big]e^{-nG(\theta,\gamma)}\Big] \end{aligned}$$
(1.45)

where

$$F(\theta) = 3 + (1+\varepsilon_2\varepsilon_3)\cos(2\theta) - \varepsilon_2\varepsilon_3 \xrightarrow{\varepsilon_2=\varepsilon_3} f(\theta),$$
(1.46a)

and

$$G(\theta,\gamma) = \ln\left(\frac{4}{(1-\gamma)F(\theta)}\right) \xrightarrow{\varepsilon_2=\varepsilon_3} g(\theta,\gamma).$$
(1.46b)

These expressions are symmetric under exchange of the initial polarizations of the two reset qubits ($\varepsilon_2 \leftrightarrow \varepsilon_3$). The ideal asymptotic polarization $2\varepsilon/(1+\varepsilon^2)$, obtained for $\gamma = 0$, $\theta = \pi/2$ and $\varepsilon_1(0) = 0$, $\varepsilon_2(0) = \varepsilon_3(0) = \varepsilon$, agrees with the one derived in Refs. [27, 45]. For different reset spin polarizations, this ideal limit gets modified to $[\varepsilon_2 + \varepsilon_3]/[1 + \varepsilon_2\varepsilon_3]$.

The quantum map $\Phi_{\mathcal{K}_{\mathrm{red}}}\Phi_{\mathcal{D}}$ is greatly simplified, both because the compression step can be reduced to act on the target qubit alone, with the help of the refresh, generating a Markovian process, and because it is

evaluated with respect to a tensor product with fixed reset states, allowing for the method of Ref. [71] to be applied and hence defining a single reduced compression map for every cycle. In summary, the superoperator is a matrix of small dimension (4-by-4), and unique over every cycle. In contrast, these simplifications do not occur when changing reset qubits are involved in the refresh operation, and when the evolution is non-Markovian.

To complete the thermodynamic analysis with the calculation of the work and the coefficient of performance, we need to deal with the extended quantum channel that acts on the three-qubit state space before refresh happens. To that end, we consider an extension $\mathcal{D}_{\text{ext}}$ of the damping channel that acts trivially (through the identity) on the reset qubits ρ_2 and ρ_3. We accordingly consider the channel $\mathcal{K} \circ \mathcal{D}_{\text{ext}}$ for the ensemble of three qubits, as

$$\tilde{\rho}(n) = \sum_k K_k \big(\mathcal{D}_{\text{ext}}[\rho(n)] \big) K_k^\dagger, \tag{1.47}$$

recalling that $\rho(n) = \rho_1(n) \otimes \rho_2(0) \otimes \rho_3(0)$. The role of the refresh operation is to keep the reset states equal to $\rho_2(0) \otimes \rho_3(0)$ for the start of each cooling cycle. The calculation of the coefficient of performance and, in turn, of the work applied during the compression stage requires the knowledge of the reset qubit states before the refresh stage. These states are given by

$$\tilde{\rho}_a(n) = \text{tr}_{1, b \neq a} \Big\{ \sum_k K_k \big(\mathcal{D}_{\text{ext}}[\rho(n)] \big) K_k^\dagger \Big\}$$
$$= \frac{1}{2} \begin{pmatrix} 1 - \tilde{\varepsilon}_a(n) & 0 \\ 0 & 1 + \tilde{\varepsilon}_a(n) \end{pmatrix}, \tag{1.48}$$

where a and b are either 2 or 3. The polarizations $\tilde{\varepsilon}_i(n)$ explicitly read

$$\tilde{\varepsilon}_a(n) = \frac{1}{(\gamma - 1)F(\theta) + 4} \left[\frac{2\Upsilon_a(\gamma)\sin^2\theta + 4\gamma(1 - \varepsilon_a(0)\cos^2\theta)}{2} \right.$$
$$+ e^{-nG(\theta,\gamma)} \frac{\sin^2\theta(1 + \varepsilon_2\varepsilon_3)}{F(\theta)}$$
$$\times \left(2\sin^2\theta((1 + \varepsilon_2(0)\varepsilon_3(0))\varepsilon_1(0) - \varepsilon_2(0) - \varepsilon_3(0))\right.$$
$$\left. \left. + \gamma(1 + \varepsilon_1(0))F(\theta)\right)\right], \quad (1.49)$$

with

$$\Upsilon_i(\gamma) = ((\gamma - 1)\varepsilon_a(0)^2 + \varepsilon_i(0) + \gamma)\varepsilon_{b \neq a}(0) - \varepsilon_a(0) + 1, \quad (1.50)$$

where we make explicit again the cycle dependence of qubits 2 and 3. The reset qubit states only change within a single stroke (before they are refreshed). Their dependence upon the $n - 1$ previous applications of the cooling cycle is implicit in the target qubit input state $\rho_1(n - 1)$. This is schematically represented as $\varepsilon_1(n) \to \varepsilon_1(n + 1)$ while $\varepsilon_{2,3}(0) \to \tilde{\varepsilon}_{2,3}(n + 1)$ during the dynamical evolution.

1.3.2 Theoretical evaluation of the thermodynamic quantities

We now turn to the evaluation of the thermodynamic quantities of the heat bath algorithmic cooling refrigerator and, in particular, of their fundamental upper bounds in the reversible limit ($\gamma = 0, \theta = \pi/2$), for arbitrary initial polarizations. The heat per cycle follows directly from the definition and

eq. (1.44), and reads

$$Q(n) = \Big[2((1 + \varepsilon_2\varepsilon_3)\varepsilon_1(0) - \varepsilon_2 - \varepsilon_3) \sin^2\theta$$
$$+ \gamma(1 + \varepsilon_1(0))F(\theta) \Big] \frac{e^{-nG(\theta,\gamma)}}{4}. \quad (1.51)$$

The corresponding cooling power is found to be

$$J(n) = Q(n+1) - Q(n) = \left[\frac{(1-\gamma)F(\theta)}{4} - 1 \right] Q(n), \quad (1.52)$$

where the reversible $(\gamma \to 0, \theta = \theta_n)$ limit is

$$J_{\max}(n) = \Big[(1 + \varepsilon_2\varepsilon_3)[\varepsilon_2 + \varepsilon_3 - \varepsilon_1(0)(1 + \varepsilon_2\varepsilon_3)]$$
$$+ \gamma \big[2\varepsilon_2 + 2\varepsilon_3 + \varepsilon_2^2\varepsilon_3^2 - 1$$
$$- (1 + \varepsilon_2\varepsilon_3)$$
$$\times \big(\varepsilon_1(0)(n - 3 + (1+n)\varepsilon_2\varepsilon_3) - n(\varepsilon_2 + \varepsilon_3) \big) \big] \Big]$$
$$\times \frac{e^{-nG(\theta_n,0)}}{2(1 - \varepsilon_2\varepsilon_3)}.$$
$$(1.53)$$

The cooling power $J(n)$ is proportional to the heat $Q(n)$ since the finite difference of an exponential is again an exponential. The fundamental upper bound $J_{\max}(n)$, eq. (1.52), generalizes eq. (1.33) to arbitrary initial polarizations $\varepsilon_i(0)$ of the three qubits. Contrary to polarization, maximum power is not achieved for $\theta \to \pi/2$. This happens because the steady state value $J(\infty)$ is reached faster in this limit due to large values of the power in the first two rounds. This then leads to a suppressed heat removal from the target qubit and a reduced power output. To maximize the

refrigeration power $J(n)$, a solution is to suppress the exponential decay in n by decreasing the angle θ (and therefore the decay coefficient $G(\theta, \gamma)$) with the number of strokes n. The optimal value of θ is

$$
\theta_n = \begin{cases} \pi/2, & n = 0 \\ \begin{cases} \pi/2, & (\varepsilon_1(0), \varepsilon_2, \varepsilon_3) \in \mathbb{J} \\ \vartheta_n, & \text{otherwise} \end{cases}, & n = 1 \\ \vartheta_n, & n \geq 2, \end{cases}
\tag{1.54}
$$

where the angle ϑ_n reads

$$
\vartheta_n = \frac{1}{2} \arccos\left(\frac{2\varepsilon_2\varepsilon_3 + n\varepsilon_2\varepsilon_3 + n - 6}{(2+n)(1+\varepsilon_2\varepsilon_3)} \right),
\tag{1.55}
$$

And the region $\mathbb{J}$ is defined by

$$
\mathbb{J} = \left\{ (\varepsilon_1(0), \varepsilon_2, \varepsilon_3) \,\middle|\, 0 \leq \varepsilon_1(0) < \frac{1}{\sqrt{3}} \right.
$$
$$
\left. \cap \left(0 \leq \varepsilon_2 < \frac{1}{3\varepsilon_1(0)} \cap 0 \leq \varepsilon_3 < \frac{1}{3\varepsilon_2} \right) \right\},
\tag{1.56}
$$

where we always assumed that $(\varepsilon_2, \varepsilon_3) \geq \varepsilon_1(0) \geq 0$.

On the other hand, using eq. (1.48) and the definition of the work done
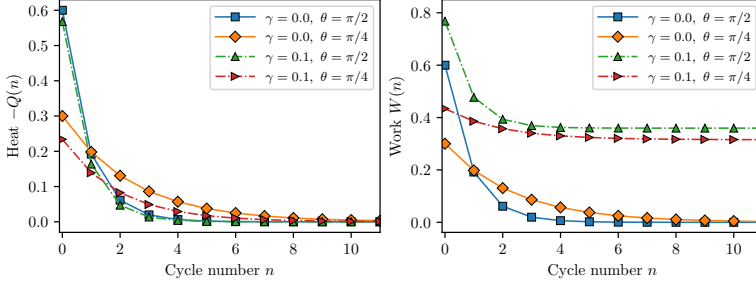
Figure 1.6: Heat $Q(n)$, eq. (1.51), and work $W(n)$, eq. (1.57), as a function of the number n of cycles, for various values of damping coefficient γ and of the mixing angle θ. Parameters are $\varepsilon_1(0) = 0$, $\varepsilon_2(0) = \varepsilon_3(0) = 0.6$.

on the qubit system, we obtain

$$
\begin{aligned}
W(n) = {} & 4\sin^2\theta \frac{(1+\varepsilon_2)(1+\varepsilon_3)}{(\gamma-1)F(\theta)+4} \\
& + \left(1 + 4\gamma\sin^2\theta \frac{(1+\varepsilon_2\varepsilon_3)(\gamma-1)}{(\gamma-1)F(\theta)+4} \right) \\
& \times \Big[2\sin^2\theta\big((1+\varepsilon_2\varepsilon_3)\varepsilon_1(0) - \varepsilon_2 - \varepsilon_3\big) \\
& + \gamma\big(1+\varepsilon_1(0)\big)F(\theta)\Big] \frac{e^{-nG(\theta,\gamma)}}{4}.
\end{aligned}
\tag{1.57}
$$

With the heat and work, the coefficient of performance eventually follows as

$$
\zeta(n) = \frac{-[(\gamma-1)F(\theta)+4]R(\theta,\gamma)e^{-nG(\theta,\gamma)}}{C(\theta,\gamma)R(\theta,\gamma)e^{-nG(\theta,\gamma)} + 16\sin^2(\theta)(1+\varepsilon_2)(1+\varepsilon_3)}
$$

$$
\tag{1.58}
$$

where

$$C(\theta, \gamma) = (\gamma - 1)F(\theta) + 4 - 4(1 + \varepsilon_2\varepsilon_3)(1 - \gamma)\sin^2(\theta) \qquad (1.59)$$

and

$$R(\theta, \gamma) = 2\sin^2(\theta)[(1 + \varepsilon_2\varepsilon_3)\varepsilon_1(0) - \varepsilon_2 - \varepsilon_3] + \gamma(1 + \varepsilon_1(0))F(\theta).$$
$$(1.60)$$

The fundamental upper bound $\zeta_{\max}(n)$, eq. (1.58), generalizes eq. (1.30) to arbitrary initial polarizations $\varepsilon_i(0)$ of the three qubits. As previously discussed, at exactly $\gamma = 0$ it is identically 1. So we indicate the formula to first order in a γ expansion, which reads

$$\begin{aligned}
\zeta_{\max}(n) = 1 &+ \frac{4\gamma}{1 + \varepsilon_2\varepsilon_3} \\
&\times \left(1 + \frac{(1 + \varepsilon_2)(1 + \varepsilon_3)}{\varepsilon_1(0) - \varepsilon_2 - \varepsilon_3 + \varepsilon_1(0)\varepsilon_2\varepsilon_3}e^{nG(\pi/2,0)}\right) \\
&+ O(\gamma^2).
\end{aligned}$$
$$(1.61)$$

Clearly a trade-off exists between the damping parameter γ and the number of cycles that can be taken into consideration before the exponential factor dominates, at which point the expression no longer makes physical sense.

Heat $Q(n)$, eq. (1.51), and work $W(n)$, eq. (1.57) are shown in fig. 1.6 as a function of the number n of cycles, for various values of decay rate γ and of the mixing angle θ. The influence of unequal initial polarizations of the reset qubits is illustrated in figs. 1.7 and 1.8 for fixed values of the damping rate $\gamma = 0.1$ and of the mixing angle $\theta = \pi/3$. Work $W(n)$ and polarization $\varepsilon_1(n)$ of the target qubit, eq. (1.45), are increased when $\varepsilon_3 > \varepsilon_2$, whereas heat $Q(n)$ is decreased. At the same time, cooling power
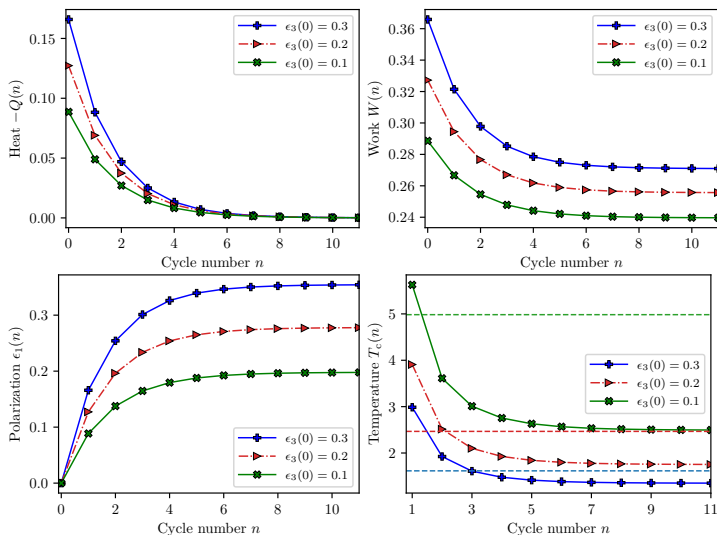
Figure 1.7: Heat $Q(n)$, eq. (1.51), work $W(n)$, eq. (1.57), and polarization of the target qubit $\varepsilon_1(n)$, eq. (1.44), as well as the corresponding temperature $T_c(n)$, as a function of the number n of cycles, for fixed values of the damping coefficient $\gamma = 0.1$ and of the mixing angle $\theta = \pi/3$, for different initial polarizations of the reset qubit 3. Parameters are $\varepsilon_1(0) = 0$, $\varepsilon_2(0) = 0.3$. Changing the initial polarization of the reset qubit may either increase or decrease the values of these thermodynamic quantities. Dashed lines in the lower right plot correspond to the respective temperatures of the reset qubits with matching colors (the red line also corresponds to the polarization $\varepsilon_2(0)$).
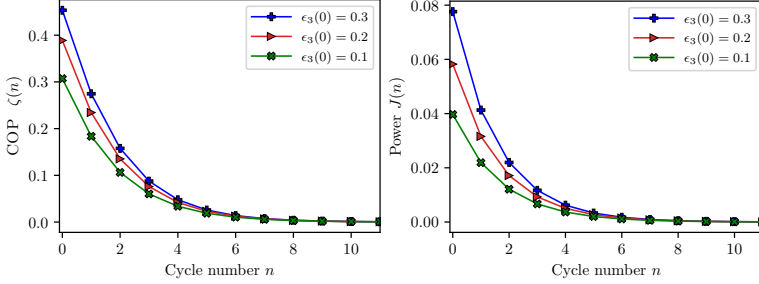
Figure 1.8: Cooling power $J(n)$, eq. (1.52), and coefficient of performance (COP) $\zeta(n)$, eq. (1.58), as a function of the number n of cycles, for fixed values of the damping coefficient $\gamma = 0.1$ and of the mixing angle $\theta = \pi/3$, for different initial polarizations of the reset qubit 3. Parameters are $\varepsilon_1(0) = 0$, $\varepsilon_2(0) = 0.3$.

$J(n)$, eq. (1.52), and COP $\zeta(n)$, eq. (1.58), are also both increased when $\varepsilon_3 > \varepsilon_2$.

1.3.3 Generality of the properties of the imperfect compression gate

The imperfect compression map $\mathcal{K}$ parametrized by the mixing angle θ slows down the convergence to the target steady state and, at the same time, preserves that steady state of perfect compression $\mathcal{K}_{\theta=\pi/2}$ for vanishing dissipation $\gamma = 0$. We show in this Section that these features generically hold for a family of imperfect compression maps given by a convex combination of two unitaries, namely the ideal compression and the identity. The structure of these generalized nonideal compression maps will provide additional physical insight into their remarkable properties.

Let us consider the trace preserving completely positive map that chooses with a probability distribution $(p_1 = \sin^2\theta, p_2 = \cos^2\theta)$ between
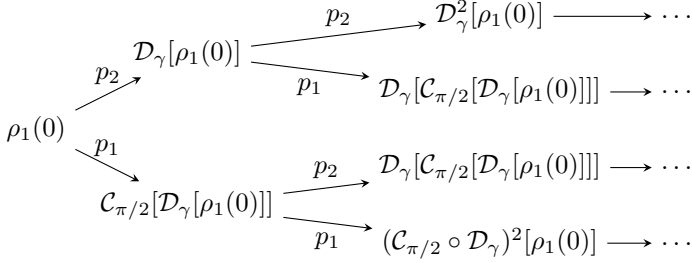
Figure 1.9: Graph representing the causal tree of possible evolution paths of fine-grained realizations of the generalized nonideal compression map (1.62) given as a convex combination of the ideal compression (with probability $p_1 = \sin^2 \theta$) and the identity map (with probability $p_2 = \cos^2 \theta$). Nonzero dissipation $\gamma \neq 0$ leads to different states of the target qubit that depend on the angle θ.

the application of the perfect compression gate and the identity (in which case nothing happens):

$$\mathcal{K}_{\text{gen}}[\rho] = \sin^2(\theta) U \rho U^\dagger + \cos^2(\theta) \rho, \tag{1.62}$$

where $U = \exp(-i\pi H_{123}/2)$ with $H_{123} = |100\rangle\langle011| + |011\rangle\langle100|$ is the unitary describing ideal compression swap. Such a convex combination of unitary operations (sometimes called random external fields map [93]) is unital by construction and thus leaves the maximally mixed state invariant [93]. The operator-sum representation of the map $\mathcal{K}_{\text{gen}}$, which is the $\tilde{K}$ form of the Kraus operators briefly encountered before, acts identically on states diagonal in the energy eigenbasis (and only on those) as the compression map $\mathcal{K}$ with Kraus operators (1.26). The random map $\mathcal{K}_{\text{gen}}$ may thus be regarded as a generalization of the compression map $\mathcal{K}$.

Let us next show that the map (1.62) preserve the steady state of the

target quit. In analogy to eq. (1.47), we introduce the concatenated three-qubit map $\mathcal{C}_\theta = \mathcal{R} \circ \mathcal{K}_{\mathrm{gen}}$ that combines compression and refresh maps (in the absence of dissipation). We denote by $\rho_{\mathrm{ss}} = \mathcal{C}^\infty_{\pi/2}(\rho_1(0))$ the steady state of $\mathcal{C}_{\pi/2}$. We then have

$$
\begin{aligned}
\lim_{n \to \infty} \mathcal{C}^n_{\pi/2}(\rho_1(0)) &= \lim_{n \to \infty} \mathcal{C}_{\pi/2}(\rho_1(n-1)) \\
&= \lim_{n \to \infty} \mathrm{tr}_{\mathrm{a}}\{U(\rho_1(n-1) \otimes \rho_{\mathrm{a}})U^\dagger\} \\
&= \mathrm{tr}_{\mathrm{a}}\{U(\rho_{\mathrm{ss}} \otimes \rho_{\mathrm{a}})U^\dagger\} \\
&\equiv \rho_{\mathrm{ss}}.
\end{aligned}
\tag{1.63}
$$

Thus, in this limit, the concatenation of dilation, unitary, and trace, acts as an identity operation on ρ_{ss}. With this property, we can prove that $\mathcal{C}_\theta$ has a steady state which in fact does not depend on θ:

$$
\begin{aligned}
\lim_{n \to \infty} \mathcal{C}_\theta(\rho_1(n-1)) &= \lim_{n \to \infty} \sin^2(\theta)\,\mathrm{tr}_{\mathrm{a}}\{U(\rho_1(n-1) \otimes \rho_{\mathrm{a}})U^\dagger\} \\
&\quad + \lim_{n \to \infty} \cos^2(\theta)\rho_1(n-1) \\
&= \sin^2(\theta)\,\mathrm{tr}_{\mathrm{a}}\{U(\rho_{\mathrm{ss}} \otimes \rho_{\mathrm{a}})U^\dagger\} + \cos^2(\theta)\rho_{\mathrm{ss}} \\
&= \rho_{\mathrm{ss}}.
\end{aligned}
$$

$$\tag{1.64}$$

In summary, at each step the map combines two states sharing the same asymptotic value. As a result, the steady state ρ_{ss} is preserved.

Physically, the angle θ interpolates between a map which implements the one-shot ideal compression at every single step ($\theta = \pi/2$), and an identity map that does nothing ($\theta = 0$). In this one-shot regime, the features of the nonideal compression may be intuitively understood: at every cycle the compression brings the state closer to its stationary value, but in some

cycles nothing happens. As a consequence, the steady state is unchanged and the convergence time increases. This property holds approximately when γ is non-zero, but very small. We also emphasize that this behavior does not depend on the number of reset qubits.

We further note that in combination with dissipation, the second line in eq. (1.64) is no longer valid. The dissipation map $\mathcal{D}$ not only modifies the overall quantum operation, it also introduces an asymmetry between each realization of the imperfect compression. Consider the graph in fig. 1.9: In contrast to the undamped case, each branch in this tree, representing the possible fine-grained paths the system can take, leads to its own steady state. The average will constitute of a typical evolution in this branch, and will thus depend on θ to the extent that this typical path depends on the weight of the probability distribution p. For $\gamma = 0$, the majority of branches will asymptotically consist of compressions and only a single branch, the uppermost one, consists of only identity operations.

1.3.4 Data analysis of the experimental thermodynamic performance

We evaluate the heat from the set of qubit polarizations $\varepsilon_1(n)$ measured using single-shot readout [27]. Recalling the definition of the heat $Q(n) = \text{tr}\{\omega_1 Z^1[\rho_1(n+1) - \rho_1(n)]\}$, we concretely have

$$Q_{\text{exp}}(n) = -[\varepsilon_1(n+1) - \varepsilon_1(n)]. \tag{1.65}$$

The cooling power $J_{\text{exp}}(n)$ follows from the finite difference $Q_{\text{exp}}(n+1) - Q_{\text{exp}}(n)$.

Since the states $\tilde{\rho}_i(n)$ of the reset qubits after the compression stage are
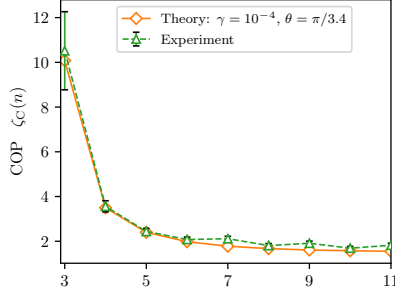
Figure 1.10: Carnot coefficient of performance (COP) $\zeta_C(n)$ as a function of the number n of cycles, for experimentally observed target qubit polarizations, and reset qubit polarization $\varepsilon_2 \sim 0.58$.

entirely determined by the target qubit polarization $\varepsilon_1(n-1)$ via eq. (1.48), the work $W(n)$ may be directly evaluated from the target polarization data (without having to measure the polarizations of the target qubits) and a non-cumulative version of eq. (1.57), where the dependence on n is implicit in using $\varepsilon_1(n)$ instead of $\varepsilon_1(0)$. That is, recalling again the original definition, $W(n) = \sum_{i=2,3} \text{tr}\{\omega_i Z^i[\tilde{\rho}_i(n) - \rho_i(n)]\}$, we have

$$W_{\text{exp}}(n) = \sin^2(\theta)\big(\gamma(\varepsilon_2\varepsilon_3 + 1) + (\gamma - 1)(\varepsilon_2\varepsilon_3 + 1)\varepsilon_1(n) + \varepsilon_2 + \varepsilon_3\big)$$
$$+ \varepsilon_1(n) - \varepsilon_1(n + 1). \quad (1.66)$$

We use the experimentally obtained values of $\varepsilon_1(n)$ to determine the work using the above relation.

Using the single-shot readout errors of the three qubits polarizations, of $\sim 3\%$ for $\varepsilon_1(n)$ and ε_2, and $\sim 1\%$ for ε_3, we estimate the relative error of $W_{\text{exp}}(n)$ as the standard deviation calculated through conventional linear propagation methods. Likewise, we estimate the relative error of $Q_{\text{exp}}(n)$

to be bounded by $\sim 3\%$ [27, 94]. The errors bars for $\zeta_{\exp}(n)$ and $J_{\exp}(n)$ follow from the definition of these quantities.

Figure 1.10 additionally shows the experimental Carnot COP $\zeta_{C\exp}(n)$ and the corresponding theoretical expectation $\zeta_C(n)$ for $\gamma = 10^{-4}$ and $\theta = \pi/3.4$. The latter are determined uniquely through the temperatures associated to the two polarizations $\varepsilon_1(n)$ and ε_2.

1.4   Summary of the chapter

We have analyzed in this chapter heat-bath algorithmic cooling, which is a simple and tractable refrigerator with promising applications in quantum technologies. The algorithm provides a clear working definition of what it means to refrigerate a quantum system, and being subject to extensive study, thereby provides a fundamental grasp on the cooling limits achievable by refrigerators.

Our contribution to this discussion is in the important front of determining heat-bath algorithmic cooling as a de facto thermal machine [36].

1. We provide novel characterization of the algorithm by studying its coefficient of performance and power: two figures of merit essential in the understanding of refrigerators.

2. We analyze a recent implementation of the minimal HBAC in a nitrogen-vacancy center [27] by solving the full model analytically. In this study we

    (a) include the experimental sources of dissipation, that could put into question whether expected limits of HBAC are realized in

practice;

(b) show that HBAC achieves the theoretically predicted cooling limits despite the experimental deviations from the ideal theoretical models;

(c) show that HBAC is a refrigerator whose performance converge to the Carnot bound in the steady state with the thermodynamic figures of merit now analytically available.

3. In the analytical solution, we include polarization damping dynamics, that by fitting to the experimental data is shown to be largely insignificant.

4. We also include the effect of "stochastic activation" of the unitary gate, that takes the shape of probabilistic success rate of the system to be affected by the gate. By fitting to the data we show how this accounts for most of the deviation of the experimental data from the ideal dynamics, and at the same with the analytical solution we demonstrate how this does not affect the cooling limits and thereby the Carnot bounds. Furthermore, the coefficient of performance is also unaffected.

Chapter 2

Virtual qubits and their coherences

2.1 Introduction to virtual qubits in cooling

Identifying virtual quantum subsystems is an important task in the engineering and control of quantum systems. These subsystems consist of subspaces and tensor-product structures defining what operators are assigned the role of local observable in respect to the operator algebra of the full system, and are not necessarily linked to physical constituents at hand in a laboratory, hence their name "virtual."

The access to these non-trivial parts of physical systems is widely used in quantum computing and, for instance, provides means to protect quantum information from detrimental influence of the surrounding environment during an information processing task. The general notion of virtual sub-

systems has found widespread use in quantum error correction [11, 95, 96], the theory of decoherence-free subspaces [6, 7, 97–99] and noiseless systems [6, 8, 10, 100], as well as in quantum computing [11, 12, 101–105]. Beyond these applications, the tensor-product structure and subspaces of a given system relate to the very definition of entanglement, our understanding of measurement through the availability of specific observables, and foundational questions [101, 106–110].

Moreover, the concept of virtual qubits [50] has also been employed in quantum thermodynamics on a foundational level to investigate the extent to which these subsystems can be leveraged in the design and optimization of small quantum thermal machines. More generally, virtual subsystems were connected to the fundamental laws and bounds of thermodynamics [111–113], where the particular case of cooling finds applications in quantum computing when preparing the relevant qubits in low-temperature states to avoid error-inducing thermal fluctuations. Virtual subspaces have provided a unifying paradigm in the context of refrigeration limits, revealing that any refrigeration process may be understood as a generalized swap operation between the state of the system to be cooled and that of a sufficiently pure virtual subsystem of the environment [112]. In applying these principles to implementations of qubit refrigeration, the cooling limits discussed in the previous chapter were shown to be related to the presence and utilization of certain virtual qubits [46–48, 114]. Heat-bath algorithmic cooling is therefore another successful story of the use of virtual subsystems to enhance a certain task.

On a technical level, a virtual subsystem consists of a decomposition of a full Hilbert space $\mathbf{H}$ into tensor factors:

$$\mathbf{H} = (\mathbf{H}_v \otimes \mathbf{H}_w) \oplus \mathbf{H}_{\text{rem}}, \tag{2.1}$$

where we consider an additional remainder Hilbert space combines to the tensor factors; this might be needed if the $\mathbf{H}$ has dimension d, with d a prime number, in which case the remainder is a trivial subspace of dimension 1, but it can be more generally desirable depending on operational requirements for this decomposition. This factorization is particularly justified in light of a possibly more evident physical factorization of $\mathbf{H}$, such as in last chapter's where the full space factorizes into three, one for each nuclear spin, $\mathbf{H} = \mathbf{H}_{^{14}N} \otimes \mathbf{H}_{^{13}C_1} \otimes \mathbf{H}_{^{13}C_2}$.

Heat-bath algorithmic cooling can be put in terms of these virtual subsystems, which sheds more light into its functionality and is the basis of what we will study in this chapter. We start by considering the main component of HBAC: the compression unitary that implements the state transitions $|011\rangle$ to $|100\rangle$, and vice-versa. Motivated by this, we may recognize a SWAP-like channel by rewriting the last two-qubit states (from the reset qubits) as the two states of one, virtual, qubit with its own Hilbert space:

$$
\begin{aligned}
|0_2 0_3\rangle &= |0_v\rangle \\
|1_2 1_3\rangle &= |1_v\rangle \\
\Longrightarrow \mathbf{H}_v &= |0_v\rangle \oplus |1_v\rangle .
\end{aligned}
\tag{2.2}
$$

At each compression cycle, the two remaining reset states $|0_2 1_3\rangle$ and $|1_2 0_3\rangle$ are not subject to control. Motivated by this, we consider the factorization

$$
\mathbf{H}_{23} = (\mathbf{H}_v \otimes \mathbb{C}) \oplus \mathbf{H}_{\mathrm{rem}},
\tag{2.3}
$$

where the span of the states that are not controlled forms the remainder subspace, and instead the second tensor factor is a trivial component.

The advantage of framing heat-bath algorithmic cooling with virtual systems is recognizing that the cooling limit reached after the repeated refrigeration cycles by the compression unitary is essentially the virtual temperature. In this case, the virtual qubit state is defined as

$$
\begin{aligned}
\rho_v \oplus 0_{\mathrm{rem}} &= \frac{P_v \rho_{23} P_v^{\dagger}}{\mathrm{tr}\, P_v \rho_{23} P_v^{\dagger}} \\
&= \frac{1}{2} \begin{pmatrix} 1 + \varepsilon_v & 0 \\ 0 & 1 - \varepsilon_v \end{pmatrix} \oplus \begin{pmatrix} 0 & 0 \\ 0 & 0 \end{pmatrix}_{\mathrm{rem}},
\end{aligned}
\tag{2.4}
$$

where $P_v = |00\rangle\langle 00| + |11\rangle\langle 11|$ is a projector onto the virtual subspace (now without the reset qubit indices for simplicity). With the virtual qubit polarization ε_v, we can find the virtual temperature, and the cooling limit doing the operation above is

$$
\varepsilon_v = \frac{\varepsilon_2 + \varepsilon_3}{1 + \varepsilon_2 \varepsilon_3},
\tag{2.5}
$$

which is the same that we found in eq. (1.37) of the previous chapter, $\varepsilon_1(\infty) = \varepsilon_v$, for the reversible limit of no dissipation ($\gamma = 0$).

Furthermore, this procedure can be understood in terms of a partial swap operation that exchanges the state of the target qubit with that of a virtual qubit. The steady-state limit of refrigeration is therefore a full swap between these states. More explicitly, recall that each cycle of algorithmic cooling starts with an input state $\rho = \rho_1(n) \otimes \rho_2 \otimes \rho_3$. The final state of the cycle, before reset, is

$$
\tilde{\rho}(n) = U(\rho_1 \otimes \rho_2 \otimes \rho_3)U^{\dagger}.
\tag{2.6}
$$

From regular algorithmic cooling we can compute $\tilde{\rho}_1(n) = \mathrm{tr}_{23}\, \tilde{\rho}(n)$. On

the other hand, we can also interpret it, in the incoherent case where ρ_v is a diagonal matrix, as a partial swap:

$$
\begin{aligned}
\rho_1'(n) &= \text{tr}_v\{S_\phi(\rho_1 \otimes \rho_v)S_\phi^\dagger\} \\
\text{where } S_\phi &= \text{i}e^{-\text{i}\phi S_{\pi/2}} = \text{i}\cos(\phi)I + \sin(\phi)S_{\pi/2},
\end{aligned}
\tag{2.7}
$$

for a partialness parameter ϕ. In essence, that HBAC can be put in swap terms with a virtual qubit, from the perspective of the target qubit, is a statement equivalent to saying that $\tilde{\rho}_1(n) = \rho_1'(n)$ has a solution for each n.

We can also have a new look at the speed at which the target qubit is taken to its steady state in the case of last chapter. Namely, by matching the two ρ_1' matrices at each iteration n we can solve for the HBAC partial swap angle:

$$
\phi_v = \frac{1}{2}\arccos(-\varepsilon_2\varepsilon_3),
\tag{2.8}
$$

We can conclude from this, for instance, that the swap speed is lower bounded by $\phi_v = \pi/4$, meaning that in the limit where the reset polarizations approach 0 (while still $\varepsilon_2, \varepsilon_3 \geq \varepsilon_1(0)$), each iteration of HBAC acts as $\sqrt{S}$, taking the target polarization halfway through the cooling limit at each step.[a] In contrast, in the limit where the virtual qubit is pure, $\varepsilon_2 = \varepsilon_3 \to 1$, HBAC is a full swap S, and the ground state is reached after a single cycle. This complements the understanding that the steady state is reached exponentially in the number of cycles [36, 45].

We see that in general the reset qubit parameters, or equivalently the bath parameters, determine both the virtual qubit and therefore the asymptotic state with its cooling limit, but also the rate at which it is reached, through

---

[a]Although this is not a limit of practical interest since it does not cool the target qubit.

the partialness measure ϕ_v. Any realistic implementation of the algorithm can only yield partial swaps of measure $\phi < \phi_v$ due to imperfections in its application [36]. Nevertheless, in this chapter, we will build on this concept to improve HBAC to the scenario where the virtual qubit has off-diagonal elements.

Outline of the chapter. So far, the consideration of virtual qubits coherences and their use has been sparse [115–117]. In this chapter, we show an explicit and clear example of how a coherence-endowed virtual qubit can enhance an experimentally realizable system [36] beyond the universal cooling bounds [47, 48] by starting from the general refrigeration viewpoint of ref. [112] where an initial qubit is fully swapped to the coherence endowed virtual qubit at the steady state.

We start on the next section by doing a large study of how an extra unitary step can use coherence as a resource to go beyond the previous limits. A geometrical approach on the Bloch sphere [71, 93, 118] of the target qubit is used to show how this process can be made robust against imprecise knowledge of the coherences and how an average unitary that is largely independent of these coherences can be applied and still yield cooling enhancement. We study limiting cases, particularly that of ground-state cooling, and address scenarios where different experimentally motivated advantages can be sought-after.

We end the discussion by showing how a robust experimental implementation of a minimal HBAC [36] fits into this description and give a simple recipe to achieve the desired improvement. Finally, we conclude by commenting on how this can be generalized to non-minimal HBACs.

2.2 Virtual qubits and cooling using quantum coherences

Boosting polarization with coherences. We now study the use of quantum coherences, in the form of linearly superposed energy eigenstates, to achieve a boost in cooling a target system. With the example goal of preparing a multiqubit register for computation, we assume as a baseline the incoherent cooling limits well-known in the literature [45, 47, 48] applied to a qubit target system.

With the intent of studying coherences, we briefly introduce the Bloch sphere representation for the qubit state space. We define this representation for an arbitrary qubit state ρ[b] as three real-valued coordinates (x, y, z), where

$$\rho = \frac{I}{2} + x\frac{X}{2} + y\frac{Y}{2} + z\frac{Z}{2}, \quad 0 \leq x^2 + y^2 + z^2 \leq 1. \qquad (2.9)$$

Recall from the last chapter that we defined the qubit Hamiltonians to be $H = -\omega Z/2$, this configures the z-axis as the energy axis, connecting the two energy eigenstates $Z|0\rangle = -|0\rangle$ and $Z|1\rangle = |1\rangle$ at the north and south pole of the Bloch sphere, respectively. We assume the target qubit to start in a thermal state, with temperature parametrized by the qubit polarization $\varepsilon = \operatorname{tr} Z\rho$. In the Bloch coordinates, the definition of polarization means that it equals the z coordinate, $z = \varepsilon$; we refrain from using z henceforth, and instead stick to ε. Moreover, states on the energy axis have $x = y = 0$. We use the variables x and y to further introduce polar coordinates (γ, α)

---

[b]To be used particularly in the case of the target qubit ρ_s

for coherences, which read:

$$x + iy = \gamma e^{i\alpha}\sqrt{1 - \varepsilon^2},$$ (2.10)

where $0 \leq \gamma \leq 1$ and $0 \leq \alpha \leq 2\pi$ defines an operator $A = \cos(\alpha)X + \sin(\alpha)Y$. The plane $Z \times A$ is then perpendicular to the $X \times Y$ plane. These polar coordinates will simplify our treatment of the coherences in what follows. In these coordinates the virtual qubit state is

$$\rho_v = \frac{1}{2}\begin{pmatrix} 1 + \varepsilon_v & \gamma e^{-i\alpha}\sqrt{1 - \varepsilon_v^2} \\ \gamma e^{i\alpha}\sqrt{1 - \varepsilon_v^2} & 1 - \varepsilon_v \end{pmatrix}.$$ (2.11)

This state, in contrast to eq. (2.4), has coherences. It will be the base of our studies in this chapter.

To set up for the following section of results, we describe geometrically the ensuing incoherent dynamics. The process starts with the thermal state at coordinates $(0, 0, \varepsilon_s(0))$ (full dot above maximally mixed state in fig. 2.1). Standard cooling protocols proceed along the energy axis [31] until it reaches the incoherent virtual qubit state, $\rho_v = (I + \varepsilon_v Z)/2$, with polarization $\varepsilon_v > \varepsilon_s(0)$. After (infinitely) many cooling cycles, the system ends in the refrigerated state $(0, 0, \varepsilon_s(\infty) = \varepsilon_v)$ (lower-height star at energy axis in fig. 2.1). The lowest possible temperature in this framework is given by our baseline cooling limits [47, 48, 115, 116].

2.2.1 Sharp polarization boosting

Improving the cooling limits so far described in the literature means accessing higher-polarized virtual qubits. We now describe another way of achieving an improvement by utilizing coherences present in the virtual
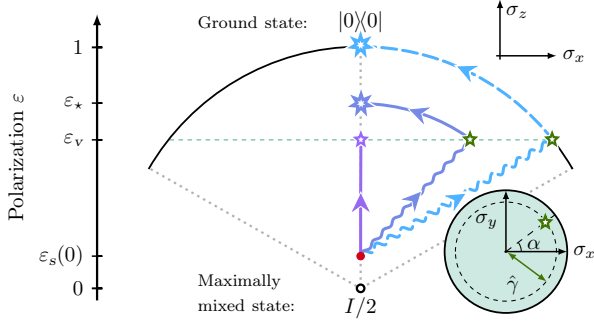
Figure 2.1: Main: cross-section of the cap of the Bloch sphere contrasting the swap dynamics of incoherent and coherent states. Inset: cross-section at the height ε_v displaying normalized coherence coordinates ($\hat{\gamma} = \gamma\sqrt{1 - \varepsilon_v^2}/2, \alpha$) of the target state.

qubit after they have been transported to the cooled target qubit. The baseline of comparison when utilizing coherences for cooling is described in fig. 2.1, where we fix the virtual qubit polarization ε_v, i.e. the latitude, in the Bloch sphere, which the first refrigeration dynamics reaches, and where the polarization boost through coherences starts.

Endowing the virtual qubit with coherence γ (with fixed polarization ε_v) increases its purity, moving the state away from the energy axis and closer to the surface of the sphere (off-axis stars in fig. 2.1). This state may be ultimately turned into better cooling by mapping it back to the energy basis (middle-height star in fig. 2.1). For this step, we only consider unitary operations that at most rotate the virtual state back to the energy axis, and thus do not change its purity. This is justified because any other resource that may further increase purity could have been used to achieve a higher virtual polarization ε_v in the first place.

In essence, we are here tasked with exactly diagonalizing the virtual qubit state. Thus, the maximal resulting polarization achievable for this operation is

$$\varepsilon_\star = \sqrt{\varepsilon_v^2 + (1 - \varepsilon_v^2)\gamma^2}, \tag{2.12}$$

given by the eigenvalues of the coherent virtual qubit. Finding the right diagonalizing unitary demands a knowledge of the two parameters: γ, the coherence amplitude, and α, the coherence phase. At fixed γ the only remaining variable to determine is α. The unitary realizing the appropriate rotation should have a rotation axis given by an operator orthogonal to A, and the angle of rotation is a function of γ in general. The axis of rotation and angle are then

$$A_\perp(\alpha) = -\sin(\alpha)X + \cos(\alpha)Y \tag{2.13a}$$

$$\chi(\gamma) = \arccos\left(\frac{\varepsilon_v}{\varepsilon_\star(\gamma)}\right), \tag{2.13b}$$

which combine in the unitary $B_{A_\perp}(\chi) = \exp(i\chi A_\perp/2)$. This equation should be interpreted as defining $\varepsilon_\star$ implicitly from γ after we do the appropriate $\chi(\gamma)$ rotation. Evidently, in the ground-state cooling scenario we have that $\varepsilon_\star(\gamma = 1) = 1$.

2.2.2 Robust cooling with confidence intervals

We now consider an ensemble of virtual states for which γ and α lie, uniformly distributed, within a confidence interval of size $\delta\gamma$ and bounds $\gamma_{\min}$ and $\gamma_{\max}$, and $\delta\alpha$ with bounds $\alpha_{\min}$ and $\alpha_{\max}$. Logical bounds exist where the density matrix is still positive semidefinite, and are $0 \leq \gamma \leq 1$, and $0 \leq \alpha \leq 2\pi$. Otherwise, we may have tighter bounds given experimentally

motivated considerations, in the attempt to build an exact state. This ensemble can be written in these terms as

$$\bar{\rho}_v = \int \mathrm{d}\alpha_v \, \gamma_v \mathrm{d}\gamma_v \, p(\gamma_v, \alpha_v) \, \rho_v(\gamma_v, \alpha_v), \qquad (2.14)$$

where $p(\gamma, \alpha) = 2/((\gamma_{\max}^2 - \gamma_{\min}^2)\delta\alpha)$ is the uniform distribution over the disk sector. The corresponding rotated state is then

$$\begin{aligned}
\bar{\rho}'(\alpha_B, \gamma_B) &= B\bar{\rho}_v B^\dagger \\
&= \int \mathrm{d}\alpha_v \, \gamma_v \mathrm{d}\gamma_v \, p(\gamma_v, \alpha_v) \, B_{(\alpha_B, \gamma_B)} \rho_v(\gamma_v, \alpha_v) B^\dagger_{(\alpha_B, \gamma_B)} \\
&= \int \mathrm{d}\alpha_v \, \gamma_v \mathrm{d}\gamma_v \, p(\gamma_v, \alpha_v) \, \rho'(\gamma_v, \alpha_v; \gamma_B, \alpha_B),
\end{aligned}$$

$$(2.15)$$

where individual stochastic realizations of the process (starting from one sampled initial state ρ_v) result in polarization values which are functions of the initial random variables ε_v, γ_v and α_v, but the parameters of the average final state are a function of only rotation variables, such as $\bar{\varepsilon}'(\alpha_B, \gamma_B)$.

Faced with these confidence intervals, we now approach the task of inexact diagonalization, where we optimize the rotation of an ensemble of states. How can we cool the target qubit on average, boosting its polarization, given we do not know how coherent it is? To tackle this problem, we distinguish the coordinates (γ_v, α_v), that define a virtual state we wish to rotate, from the reference coordinates (γ_B, α_B) that define the variables $A_\perp(\alpha_B)$ and $\chi(\gamma_B)$ of the unitary B; from this point onwards we will leave A and χ implicit and only work with α_B and γ_B to simplify notation. In the exact diagonalization scenario of last section, this implied that $(\gamma_B, \alpha_B) = (\gamma_v, \alpha_v)$. As we will soon see, a distinction arises, ultimately

implying that knowing α is in general more profitable than knowing γ from the perspective of achieving lower temperatures. We start with the case where α is sharply determined but γ is lies in a bounded interval. Thus, for this process, we fix $\alpha_B = \alpha_v$ and consider the pair of coordinates (γ_v, γ_B).

There are three possible cases to consider: (i) when γ_B also lies within the bounded interval, (ii) when $\gamma_B < \gamma_{\min}$, and (iii) when $\gamma_B > \gamma_{\max}$. In any case, the resulting state will have a polarization that reads

$$
\begin{aligned}
\varepsilon'(\varepsilon_v, \gamma_v; \gamma_B) &= \operatorname{tr}\{B_{(\alpha_v, \gamma_B)} \rho_v(\gamma_v, \alpha_v) B^\dagger_{(\alpha_v, \gamma_B)} Z\} \\
&= \frac{\varepsilon_v^2 + \gamma_v \gamma_B (1 - \varepsilon_v^2)}{\sqrt{\varepsilon_v^2 + \gamma_B^2 (1 - \varepsilon_v^2)}},
\end{aligned}
\tag{2.16}
$$

which is one resulting stochastic realization contributing to the integral in eq. (2.15). The first case is the only one for which rotations exist that will take one possible state in the ensemble to its highest possible polarization at the same time coherences are completely consumed. We leave the notation $\varepsilon_\star$ for these exactly diagonalized states, which might not be the state with higher polarization, but is always the one with vanishing coherences. Now contrast this with the second case, $\gamma_B < \gamma_{\min}$. Every physically realized virtual state $\gamma_v > \gamma_{\min}$ will have achieved an improved cooling limit $\varepsilon' > \varepsilon_v$, with polarization monotonically increasing with how large the rotation is. In this regime, the highest polarization achievable is for $\gamma_v = \gamma_{\max}$, where a maximal amount of coherence will remain. No state diagonal state achieved in this arrangement.

Finally, consider the third scenario, where $\gamma_B > \gamma_{\max}$. In this regime, the larger rotations may not imply enhanced cooling. This regime demands a second lower bound based on what states can still be cooled: a large enough rotation of a state with small enough γ_v may result in heating
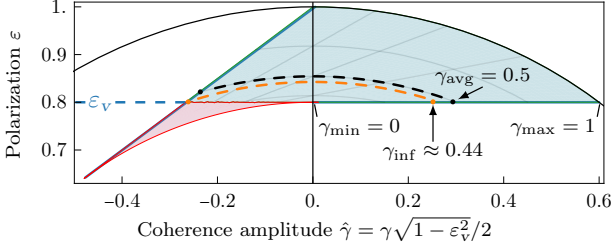
Figure 2.2: Cooling boost with maximal coherence amplitude uncertainty, showing every possible resulting state of our boosting protocol. Enhanced cooling, $\varepsilon' > \varepsilon_v$, can be achieved even if the amount of coherence γ_v is only known to be in any confidence interval, of bounding values $\gamma_{\min}$ and $\gamma_{\max}$. Moreover, improved cooling is always reached on average because, for every interval, the average coherence amplitude, γ_{avg}, lies above the $\gamma_{\inf}$ lower bound.

instead. Equating ε' to ε_v and solving for γ_v yields this second, a posteriori lower bound we denote by $\gamma_{\inf}$, marking the boundary between heating and cooling after rotation:

$$\gamma_{\inf}(\gamma_B) = \varepsilon_v \frac{\sqrt{\varepsilon_v^2 + \gamma_B^2(1 - \varepsilon_v^2)}}{\gamma_B(1 - \varepsilon_v^2)} - \frac{\varepsilon_v^2}{\gamma_B(1 - \varepsilon_v^2)}. \tag{2.17}$$

Thus, every state starting from γ_v is still cooled as long as $\gamma_v > \gamma_{\inf}$ when a rotation by $\gamma_B > \gamma_{\max}$ is implemented. This means that, in the interplay with the a priori lower bound $\gamma_{\min}$, there are two possible outcomes: if $\gamma_{\inf} < \gamma_{\min}$, then every possible state on the original interval is guaranteed to be cooled. Otherwise, in doing a rotation by γ_B, we may risk heating the target qubit. The most polarized state is again for $\gamma = \gamma_{\max}$. The worst case overall is for the pair $(\gamma_v = 0, \gamma_B = 1)$, where the state is heated to $\varepsilon_{\gamma_B=1} = \varepsilon_v^2 < \varepsilon_v$.

To conclude, we also tackle the converse problem of finding the lowest

coherent state at the boundary between heating and cooling. The solution to this problem answers the question: what is the maximal γ_B that is guaranteed to yield cooling given a lower bound $\gamma_{\min}$? This solution also branches into three cases, that translate to three regions for which this is possible. For $1/2 \leq \gamma_{\min} < \gamma_{\max}$, every γ_B cools every realization of the ensemble of states. On the lower half of the line, $\gamma_{\min} \leq 1/2$, this is true as long as the state polarization also obeys a constraint: $\varepsilon_v \leq \gamma_{\min}/(1 - \gamma_{\min})$.[c] For polarizations $\varepsilon_v > \gamma_{\min}/(1 - \gamma_{\min})$, the allowed reference coherences are upper bounded by

$$\gamma_{B+} = \frac{2\varepsilon_v^2 \gamma_{\min}}{\varepsilon_v^2 - \gamma_{\min}^2(1 - \varepsilon_v^2)}. \tag{2.18}$$

With this information, the region of heating is entirely determined for any bounds $\gamma_{\min}$ and $\gamma_{\max}$ and choice of γ_B. In fig. 2.2 we display these interval considerations for a hypothetical experiment that creates an ensemble of maximal uncertainty in the knowledge of the coherence amplitude.

2.2.3 Coherence phase confidence interval

Now we set a sharp value for γ_v, letting the angle be bounded by $\alpha_{\min} \leq \alpha_v \leq \alpha_{\max}$, and consider the associated cooling domains. In fig. 2.3 we display the surface of states achievable by all possible rotations by angles about $A_\perp$ (in orange and green, background), where the initial state has known and fixed γ_v but random α_v, uniformly distributed on the circle. In this case, although there are instances of cooling (near the top of the surface), the average outcome is heating, even for very small γ_B. This

---

[c]It may be unexpected that polarization is bounded by a coherence parameter, but this can be straightforwardly understood by realizing that, upon rotation, these quantities get mixed up.
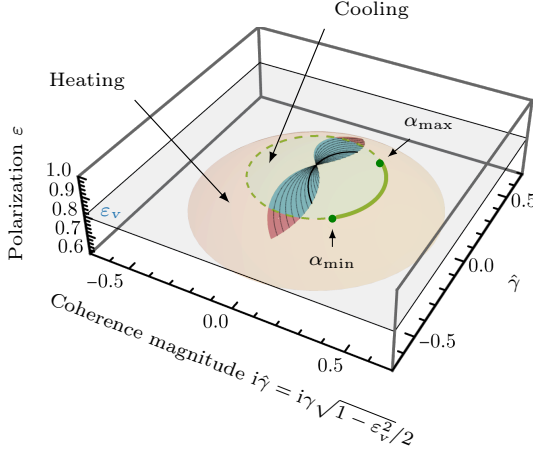
Figure 2.3: Geometric representation (full green line) of ensemble of states at $\gamma_v = 0.5$ with a confidence interval between $\alpha_{\min} = -\pi/4$ and $\alpha_{\max} = \pi/4$. The shaded region of achievable cooling (blue) and heating (red) is found by applying the unitary rotation with $\gamma_B = \gamma_v$ and $\alpha_B = \alpha_v - \pi/2$ for every point in the confidence interval (see corresponding average in fig. 2.4). The thicker black line represents the achievable polarization region for fixed $\alpha_B = (\alpha_{\max} - \alpha_{\min})/2$.

average corresponds to the geometric centroid of that surface, that lies below the plane at height ε_v. We also display an example scenario of average cooling in fig. 2.3 where a geometric representation of the initial and final ensemble of states is shown, with $\delta\alpha = \pi/2$ and $\gamma_B = \gamma_v = 0.5$. The regions of rotated states are now more complicated and there is no simple recipe, such as in the sharp α_B case, to be identified for average cooling, as a result we choose to also sample the axes of rotation from an "orthogonal interval" defined by setting $\alpha_B = \alpha_v - \pi/2$ for every possible α_v in the confidence interval. The rotated ensemble of states (in blue and red), with an average polarization above the initial value of $\varepsilon_v = 0.8$, is hashed with

curves (in black) where α_B is fixed.

The regions of average cooling are found by integrating the polarization value of the rotated ensemble of states,

$$\varepsilon'(\gamma_B, \alpha_B) = \gamma_v \sqrt{1 - \varepsilon_v^2} \sin(\alpha_v - \alpha_B) \sin(\chi(\gamma_B)) + \varepsilon_v \cos(\chi(\gamma_B)), \tag{2.19}$$

over the surface defined by α_v (which yields $\bar{\varepsilon}'$) and then α_B:

$$\begin{aligned}
\widetilde{\varepsilon}(\gamma_B) &= \int_{\alpha_{\min} - \pi/2}^{\alpha_{\max} - \pi/2} \frac{\mathrm{d}\alpha_B}{\delta\alpha} \left[\int_{\alpha_{\min}}^{\alpha_{\max}} \frac{\mathrm{d}\alpha_v}{\delta\alpha} \varepsilon' \right] \\
&= \frac{2\gamma_v \gamma_B (1 - \varepsilon_v^2)(1 - \cos(\delta\alpha)) + \delta\alpha^2 \varepsilon_v^2}{\varepsilon_v^2 + \gamma_B^2(1 - \varepsilon_v^2)},
\end{aligned} \tag{2.20}$$

where $\widetilde{\varepsilon}(\gamma_B)$ differs from $\bar{\varepsilon}'(\gamma_B)$ as we consider both the average of the random of initial states, as defined in the ensemble (2.15), and an average over correspondingly chosen axes of rotation.

We use eq. (2.20) to plot fig. 2.4, where we show the parameter space for average achievable polarization, $\overline{\varepsilon'}$, with corresponding average cooling (blue) and average heating (red) regions. We again fix the initial polarization at $\varepsilon_v = 0.8$. We observe a large cooling region (bottom part of the figure) for various values of $\delta\alpha$ and of γ_B/γ_v. Maximal uncertainty of the coherence phase ($\delta\alpha = 2\pi$) does not lead to average cooling, in contrast to what happens for incomplete knowledge of the coherence parameter γ_v discussed in the preceding section. However, enhanced average cooling is still achieved for all γ_B/γ_v when $\delta\alpha < 0.9\pi$. We also note that choosing γ_B to be smaller than its actual realizable values γ_v (that is, taking smaller ratio γ_B/γ_v) is beneficial for achieving improved average cooling with large confidence interval $\delta\alpha$, although typically one would cool less by doing so, as could also be expected from the discussion in the last section.
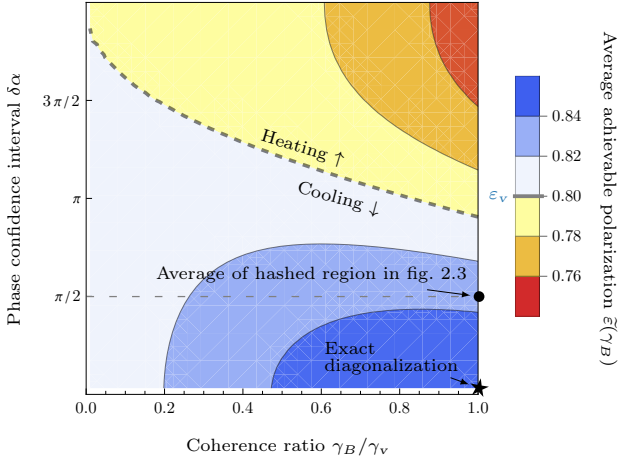
Figure 2.4: Average achievable polarizations for unknown coherence phase $\bar{\varepsilon}$ over ensemble of states, eq. (2.20), for $\gamma_B/\gamma_v < 1$ and various confidence intervals $\delta\alpha = \alpha_{\max} - \alpha_{\min}$, with $\alpha_B = \alpha - \pi/2$ and $\varepsilon_v = 0.8$. Average cooling is found for all $\gamma_B/\gamma_v < 1$ when $\delta\alpha < 0.9\pi$.

2.3 Application to heat-bath algorithmic cooling

The reversible heat-bath algorithmic cooling of last chapter is an experimentally available implementation of a refrigeration channel that is capable of accessing virtual qubit coherences as described in the last section, and is thus subject to the robust cooling boost we just devised. Despite this, the HBAC dynamics enjoys some special properties, of being ergodic (meaning it has a unique steady state), or more particularly, it is mixing: it has a unique steady state for any initial state. Furthermore, the channel is also homogenizing [119, 120], meaning that the steady state is defined by the ancilla with which the target interacts (in the particular case of HBAC, this

"ancilla" is, in fact, the virtual qubit of what we have previously called the ancillas, which are the reset qubits).
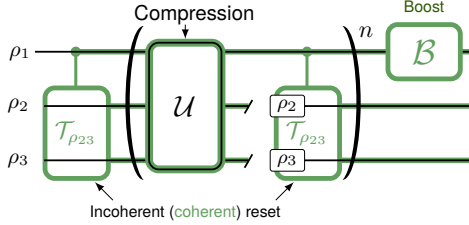
Figure 2.5: Heat-bath algorithmic cooling circuit diagram with coherent reset qubits and including the final boost rotation $\mathcal{B}$.

We use here the vectorized form of the dynamics to display the encoding of the virtual qubit into the refrigeration channel realized by algorithmic cooling. The vectorized HBAC dynamics is given by

$$\vec{\rho}_1(n) = \underbrace{\left(\Phi_{\mathrm{tr}}\Phi_{\mathcal{U}}\Phi_{\mathcal{T}}\right)^n}_{\Phi_{\mathcal{C}}}\vec{\rho}_1(0), \tag{2.21}$$

where the compression unitary is denoted by $\mathcal{U}[\rho] = U\rho U^\dagger$, and we choose to split the refresh operator $\mathcal{R}$ into two parts: the partial trace quantum map, $\mathrm{tr}_{23}\,\rho_{123} = \rho_1$, over the reset qubits, and the tensor product $\mathcal{T}_{\rho_{23}}[\rho] = \rho \otimes \rho_{23}$, where now ρ_{23} is now a nonseparable state due to the presence of coherences in the virtual qubit, in contrast to the incoherent virtual qubit usually studied in the literature and that was elaborated in the previous chapter. In fig. 2.5 we display the modified version of fig. 1.1.

At the steady state, $n \to \infty$, the cooling superoperator in the vectorized form is then $\mathcal{C}^\infty \mapsto \Phi_{\mathcal{C}}^\infty = (\vec{\rho}_v \quad 0 \quad 0 \quad \vec{\rho}_v)$, written as column matrices.
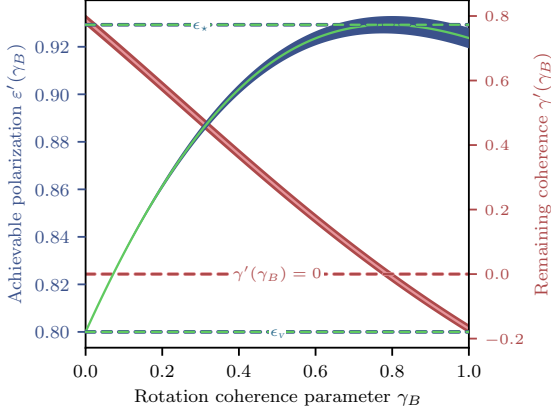
Figure 2.6: Achievable polarization ε', eq. (2.16), (green) after a unitary rotation parametrized by the coherence parameter γ_B for a realistic heat-bath algorithmic cooling protocol using nitrogen-vacancy (NV) centers in diamond. The coherent virtual qubit, with polarization $\varepsilon_v = 0.8$, is engineered by maximally entangling the two reset qubits with 97.6% fidelity. Maximum polarization $\varepsilon_\star$, eq. (2.26), is reached for $\gamma_B \sim 0.79$, a value for which the remaining coherence of the virtual qubit, γ_B, (pink) vanishes; the blue and red shaded areas represent the respective confidence intervals of ε' and γ_B.

Its action on the initial target qubit state is then

$$\begin{aligned}
\Phi_{\mathcal{C}}^{\infty} \vec{\rho}_1(0) &= \begin{pmatrix} \vec{\rho}_v & 0 & 0 & \vec{\rho}_v \end{pmatrix} \cdot \vec{\rho}_1(0) \\
&= \vec{\rho}_v(\langle 0|\rho_1(0)|0\rangle + \langle 1|\rho_1(0)|1\rangle) \\
&= \vec{\rho}_v,
\end{aligned} \tag{2.22}$$

taking the form of a full SWAP unitary gate between target and virtual qubit. Finally, by direct computation of $\Phi_{\mathcal{C}}^{\infty}$ we arrive at a coherent virtual qubit at the steady state, whose polarization is the same as in the incoherent case, eq. (2.4).

The virtual coherences may be engineered by entangling the reset qubits through the off-diagonal elements

$$\langle 00|\rho_{23}|11\rangle = \frac{\xi}{4}e^{-i\eta}\sqrt{(1-\varepsilon_2^2)(1-\varepsilon_3^2)}, \tag{2.23}$$

where $0 \leq \xi \leq 1$. The resulting virtual coherence is

$$\langle 0|\rho_v|1\rangle = \frac{\gamma_v}{2}e^{-i\alpha_v}\sqrt{1-\varepsilon_v^2}, \tag{2.24}$$

as desired. As a result, the steady state coherences, as a function of the engineered coherences, are

$$\begin{aligned} \gamma_v &= \varepsilon_v\xi \\ \alpha_v &= \eta + \frac{\pi}{2}. \end{aligned} \tag{2.25}$$

We immediately see that the rescaling present in eq. (2.25) limits the highest possible virtual qubit coherence. When $\xi = 1$, where the reset qubits are maximally coherent while still being a positive semidefinite matrix, the corresponding virtual qubit coherence is exactly $\gamma = \varepsilon_v$. This means that the maximally coherent virtual qubit at polarization ε_v can be further cooled, in the treatment of the previous section, to a maximum of

$$\varepsilon_\star = \varepsilon_v\sqrt{2-\varepsilon_v^2}, \tag{2.26}$$

as shown in fig. 2.6.

In this study we used the unitary gate U from chapter 1, expression (1.21):

$$U = I_3 \oplus (-\mathrm{i}X_v ir) \oplus I_3. \tag{2.27}$$

(a) (b)
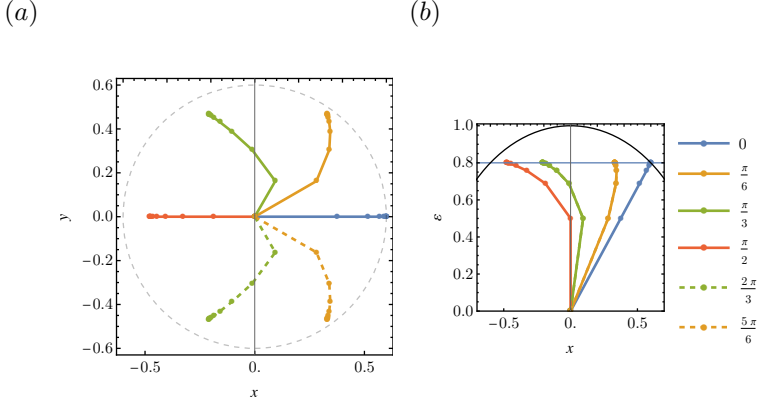
Figure 2.7: Dynamical evolution represented geometrically in the Bloch sphere for multiple values of the engineered virtual qubit phase η, and matching unitary gate phase U'_η according to eq. (2.28). (a) Target qubit dynamics projected on the $X \times Y$ plane at $\varepsilon = \varepsilon_v$. The dashed circle indicates the radius of the Bloch sphere at that height, displaying the difference in the reach of coherence amplitude of the target qubit for different phase values. (b) dynamics projected on the $X \times Z$ plane, displaying the cooling process before the final boost. The best value of coherence amplitude, and therefore the best case scenario for the final boost unitary, happens for parameter values $\eta = 0$, where $\gamma_v = \xi$.

The use of coherences can be improved by considering other gates, however. In fact, the origin of relations (2.25) is a mismatch between the exact details of the unitary gate chosen and the coherence phase of the virtual qubit. In eq. (1.21), the virtual qubit subspace includes a relative phase equal to $e^{-i\pi/2}$ with respect to the other states. If this phase is taken to be more general and to match the coherence phase of the engineered virtual qubit, $e^{-i\eta}$, we arrive at a modified unitary compression gate

$$U'_\eta = I_3 \oplus e^{-i\eta} X_v \oplus I_3. \tag{2.28}$$

This unitary has the potential to utilize the virtual qubit coherence fully: by setting $\eta = 0$, the resulting evolution is again a partial swap at every step, such as described for the incoherent case in eq. (2.7), culminating to a full swap asymptotically. We show the dependence of the full evolution in the Bloch sphere in fig. 2.7.

Resource comparison: coherences *vs* number of qubits. Known cooling limits of HBAC are available for configurations with more than two reset qubits [45], and have correspondence in the general limits [47]. These limits require a compression unitary directly extended from the one studied here, and are known to grow exponentially with the number of reset qubits as

$$\varepsilon_\infty(r, \varepsilon_a) = \varepsilon_v = \frac{(1 + \varepsilon_a)^r - (1 - \varepsilon_a)^r}{(1 + \varepsilon_a)^r + (1 - \varepsilon_a)^r}, \tag{2.29}$$

for a number r of reset qubits all at polarization ε_a. It can be shown that the γ relation in eq. (2.25) is independent of the number of reset qubits, and thus the proposed coherence-sourced cooling step is still applicable, with the difficulty lying in engineering a comparable amount of coherence ξ as the number of ancillas grow. In fig. 2.8 we compare the ratio $\varepsilon_\star/\varepsilon_v$ of the coherence-boosted cooling in the presence of r reset qubits, by the cooling in the presence of $r + 1$ reset qubits. We see that in the minimal case ($r = 2$) adding a new reset qubit is usually better for small polarizations, although being $\sim 1\%$ worse at intermediate values and comparable otherwise. However, already for $r = 3$ and above, the coherence boost is always advantageous for small polarizations, with a robust region of advantage, with an edge of more than 10% at $r > 3$. Furthermore, a trade-off occurs where this region gets smaller at the price of increasing advantage.
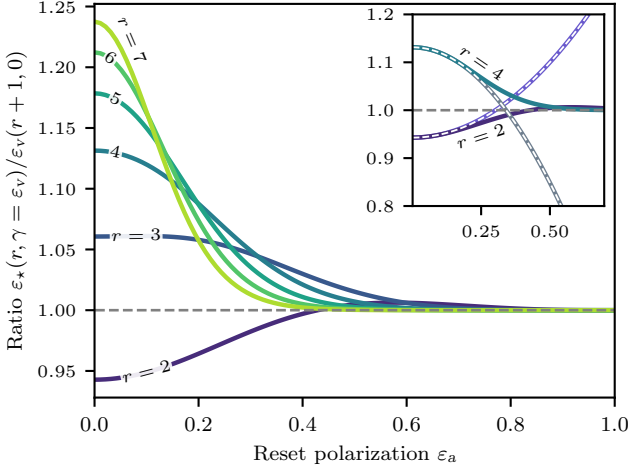
Figure 2.8: Quantum coherence versus one additional reset qubit. Ratio $\varepsilon_\star(r, \gamma = \varepsilon_v)/\varepsilon_v(r+1, \gamma = 0)$ of the maximum polarization attainable with r reset qubits by adding coherence, $\gamma = \varepsilon_v$, and the maximum polarization obtainable by adding one more reset qubit without coherence ($\gamma = 0$), as a function of the reset polarization ε_a, for various values of r. The coherent cooling scheme is better for moderate polarizations ε_a for $r = 2$ and for small polarizations ε_a for $r \geq 3$. For small reset polarizations, the ratio depends quadratically on ε_a (inset).

2.3.1 Full analytical solution in Liouville space

We end the technical part of this chapter providing details of the full analytical solution of the coherent virtual qubit dynamics of HBAC. The dynamical map $\mathcal{C}^{(n)}$ for HBAC is Markovian, and thus at arbitrary cycle number it contains every necessary information of the qubit evolution. Its

nonzero elements are

$$(\Phi_{\mathcal{C}}^n)_{11} = \frac{(1-\varepsilon_2)(1-\varepsilon_3)}{2(1+\varepsilon_2\varepsilon_3)} \frac{(1-\varepsilon_2\varepsilon_3)^n}{2^n} + \frac{(1+\varepsilon_2)(1+\varepsilon_3)}{2(1+\varepsilon_2\varepsilon_3)} \quad (2.30)$$

$$(\Phi_{\mathcal{C}}^n)_{21} = \Big[(\varepsilon_2+\varepsilon_3)(\varepsilon_2\varepsilon_3-1)$$
$$- \big[(\varepsilon_2+\varepsilon_3)(1-\varepsilon_2\varepsilon_3) - n(1-\varepsilon_2)(1-\varepsilon_3)(1+\varepsilon_2\varepsilon_3)\big]$$
$$\times \frac{(1-\varepsilon_2\varepsilon_3)^n}{2^n}\Big] \frac{e^{i\eta}\xi\sqrt{1-\varepsilon_2^2}\sqrt{1-\varepsilon_3^2}}{2(\varepsilon_2\varepsilon_3-1)(1+\varepsilon_2\varepsilon_3)^2}.$$
$$(2.31)$$

These are two elements that will help define ρ_v asymptotically as $n \to \infty$. As such, the rest of the matrix is

$$\Phi_{\mathcal{C}}^n = \begin{pmatrix} (\Phi_{\mathcal{C}}^n)_{11} & 0 & 0 & (\Phi_{\mathcal{C}}^n)_{11} \\ (\Phi_{\mathcal{C}}^n)_{21} & (\Phi_{\mathcal{C}}^n)_{22} & 0 & (\Phi_{\mathcal{C}}^n)_{21} \\ (\Phi_{\mathcal{C}}^n)_{21}^* & 0 & (\Phi_{\mathcal{C}}^n)_{33} & (\Phi_{\mathcal{C}}^n)_{21}^* \\ 1-(\Phi_{\mathcal{C}}^n)_{11} & 0 & 0 & 1-(\Phi_{\mathcal{C}}^n)_{11} \end{pmatrix}. \quad (2.32)$$

The remaining elements $(\Phi_{\mathcal{C}}^n)_{22}$ and $(\Phi_{\mathcal{C}}^n)_{33}$ are

$$(\Phi_{\mathcal{C}}^n)_{22} = (\Phi_{\mathcal{C}}^n)_{33} = \frac{(1-\varepsilon_2\varepsilon_3)^n}{2^n}. \quad (2.33)$$

These elements carry information of initial coherences but vanish asymptotically. However, in the transient dynamics, there are cross contributions from the coherence that was input into the target and the coherence that is yet to come. The full evolution of the target qubit is summarized in the

following two matrix elements:

$$
\langle 0|\rho_1(n)|0\rangle = \frac{(\varepsilon_1(0)\varepsilon_2\varepsilon_3 + \varepsilon_1(0) - \varepsilon_2 - \varepsilon_3)}{2(1 + \varepsilon_2\varepsilon_3)} \frac{(1 - \varepsilon_2\varepsilon_3)^n}{2^n}
$$
$$
+ \frac{(1 + \varepsilon_2)(1 + \varepsilon_3)}{2(1 + \varepsilon_2\varepsilon_3)}
$$
(2.34a)

$$
\langle 1|\rho_1(n)|0\rangle = \left[\frac{(\varepsilon_2 + \varepsilon_3)}{(1 + \varepsilon_2\varepsilon_3)} \right.
$$
$$
- \left(\frac{(\varepsilon_2 + \varepsilon_3)}{(1 + \varepsilon_2\varepsilon_3)} + n(\varepsilon_1(0)\varepsilon_2\varepsilon_3 + \varepsilon_1(0) - \varepsilon_2 - \varepsilon_3) \right)
$$
$$
\left. \times \frac{(1 - \varepsilon_2\varepsilon_3)^n}{2^n} \right] \frac{e^{i\eta}\xi\sqrt{1 - \varepsilon_2^2}\sqrt{1 - \varepsilon_3^2}}{2(1 + \varepsilon_2\varepsilon_3)}
$$
$$
+ \frac{c\sqrt{1 - \varepsilon_1(0)^2}}{2} \frac{(1 - \varepsilon_2\varepsilon_3)^n}{2^n},
$$
(2.34b)

where we here consider the presence of an initially coherent target qubit with coherence $c = |c|e^{-i\arg(c)}$ parametrized as usual in the rest of the paper. This initial target coherence contribution comes from $(\Phi_C^n)_{22}$, and vanishes asymptotically as it is replaced by the virtual qubit coherence.

2.4 Summary of the chapter

In this chapter we have analyzed the notion of a virtual qubit that underpins a powerful way to understand the thermodynamics of quantum systems. With this notion we were able to find that the general cooling limits expected in heat-bath algorithmic cooling are defined from the outset by the state of the reset qubits.

We advance this discussion by reframing the notion of a virtual qubit

in an operational way. We do this by recognizing it as the subsystem in the environment, at a lower temperature state, that is accessed by the refrigeration channel $\mathcal{C}$, and whose state provides the steady state of the target system through a swap [38].

1. With the virtual qubit recognize, we consider adding coherences to it with the goal of exploiting them as resource for enhanced cooling.

2. Relying on virtual qubit coherence, we are able to propose a unitary gate to be applied at the steady state that augments the polarization of the target system, cooling it further. Using this protocol, we find improved cooling bounds that are independent of the platform in which the refrigeration channel is implemented.

3. We study regimes where coherence is not sharply known, instead lying in a confidence interval. We find

   (a) that extra cooling is achievable on average even in the high-uncertainty case of coherence magnitude γ uniformly distributed over the full logical interval, $\gamma_{\min} = 0$ and $\gamma_{\max} = 1$, when the coherence phase α is sharply known,

   (b) and that extra cooling is achievable in a large set of parameter values for the phase lying in a confidence interval when γ is sharply determined.

   With this, we conclude that the protocol is remarkably robust for experimental implementation.

4. To make the proposals concrete, we apply them to heat-bath algorithmic cooling of chapter 1 with one target qubit and two reset qubits.

(a) We find that to achieve a coherent virtual qubit one has to engineer reset qubits with coherence ξ in the subspaces $|00\rangle$ and $|11\rangle$. The engineered coherence is then swapped to the target qubit at the steady state reweighted by the virtual qubit polarization, $\gamma = \varepsilon_v \xi$.

(b) We compare different resources, answering in the affirmative the question: can the addition of coherences in the reset qubits be better than the addition of one more incoherent reset qubit? In the answer, we find that for smaller reset qubit polarizations, adding coherences are generally better, when the number of reset qubits is $r \geq 3$.

Chapter 3

Equilibrium properties of a two-mode Dicke model

3.1 Introduction

Recent developments in fine experimental control of quantum systems allowed for the probing of their characteristic features, such as entanglement or other multipartite correlations and zero-temperature phase transitions, paving the way for enhancing their usage in quantum technologies, from communication to quantum simulations. Stemming from this emerged the interest in studying applications of information-theoretic and open-systems techniques to many-body models of these experimental realizations. This theoretical understanding also contributes towards the possibility of discovering novel quantum phenomena in matter.

The encompassing topic of this thesis is the betterment of cooling designs functioning particularly in the quantum regime, using phenomena that push the boundaries of stochastic thermodynamics, in particular quantum coherences and correlations in general. The previous chapters aimed at controlled quantum systems, but with motivation of simplifying implementation [30], we shift focus to a system that could house autonomous thermal machines, in particular the autonomous quantum absorption refrigerator [28, 35, 121, 122]. Such a refrigerator blueprint requires a three-body Hamiltonian of the type

$$H = \omega_h L_h^\dagger L_h + \omega_c L_c^\dagger L_c + \omega_w L_w^\dagger L_w + \lambda(L_c L_h^\dagger L_w + L_c^\dagger L_h L_w^\dagger), \quad (3.1)$$

where L are ladder operators (such as $\sigma_\pm = X \pm iY$), that are each connected to its own heat bath, indicated by c (cold), h (hot), and w (work). The working principle behind this system, that distinguishes it from controlled ones, is the replacement of an external work source for the work reservoir w, rendering the operation autonomous once the following temperature and gap parameters are met:

$$\beta_c > \beta_h > \beta_w,$$
$$\omega_h = \omega_c + \omega_w. \quad (3.2)$$

With the desired three-body interaction, the quantum absorption refrigerator similarly accesses virtual qubits of the environment, now comprised of levels $|n_h(n_w + 1)\rangle$ and $|(n_h + 1)n_w\rangle$, in contrast to the homogeneous levels 00 and 11 of algorithmic cooling, and where we wrote n levels to accommodate for bosonic modes, which will actually be the case of interest to us in this chapter. See fig. 3.1 for an illustration of the setup.
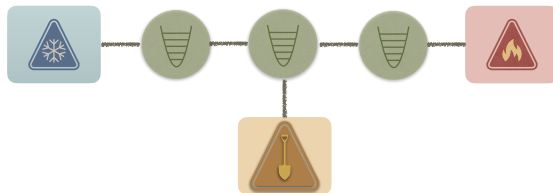
Figure 3.1: Schematic illustration of a quantum absorption refrigerator setup, with the working medium comprised of three harmonic oscillators (in green), each connected to its own heat bath: in blue, the cold bath; in red, the hot reservoir; and in yellow the work reservoir.

Desirable from the standpoint of simplified resource management and avoidance of sources of noise, the quantum absorption refrigerator is nonetheless difficult to engineer, having been realized experimentally only very recently [28, 29], despite its long history [33, 34]. As the structure of quantum coherences and correlations, such as entanglement, becomes richer, and with general interest in applying the new quantum thermodynamic developments to many-body systems, we sought for a system that could house the absorption refrigerator, at the same time it provided interesting quantum phenomena. As we will elaborate in this chapter, a two-mode extension of the commonly known Dicke model is a promising candidate. To pave the way towards realizing the quantum absorption refrigerator blueprint in that system, we study the equilibrium properties in this model, starting from the zero temperature ones, where quantum phase transitions emerge with an interesting profile of quantum correlations. We will study the robustness of these properties as we aim to extend the analysis in future work to a driven-dissipative setup for experimental implementation.

The Dicke model [123–125] often appears in these developments as a

well-established theoretical setup in quantum optics, describing long-range interactions between a bosonic mode and an ensemble of two-level systems. It also displays a quantum phase transition from a normal phase (NP) to a superradiant phase (SP). Albeit known for almost seven decades, the necessity for large spin-boson coupling made the normal-to-superradiant transition difficult to experimentally verify, which was only done so in the early millennium; see review [126] and references therein. Later on, experiments based on a gas of thermal atoms, further refined to a Bose–Einstein condensate, were made [127, 128]; developments starting from this line of approach motivates this thesis.

Recent constructions demonstrating the transition rely on the ability to tune the spin-boson interaction to the deep strong coupling regime [129, 130], which is the region of parameters where the interaction energy is comparable with the cavity mode frequency. Among the many experimental platforms involved in the aforementioned developments, cavity quantum electrodynamics is an example in which the Dicke model appears as an effective description, and where the difficulties with matching energy scales are surmounted.

Based on aforementioned experiments, ultracold atoms in optical lattices are one of the platforms realizing the Dicke model; this is done effectively in systems displaying other phenomena, such as self-organization, supersolid phases, Goldstone modes, and that work under dissipative conditions [131–133]. These references work as inspiration for the results being presented here. The way the difficulties of large coupling are overcome in these experiments is argued through the concept of analogue simulations. The setups implement an open-systems version of the model, but, as shown [134–136], they are in the same universality class albeit being in non-equilibrium, rendering them appropriate; the driven-dissipative dynamics is engineered

to serve as control for the parameters of the system.

Outline of the chapter. In chapter 3 we will elaborate on the Dicke model, an extension of it including an extra bosonic mode, and associated properties which are shared by the original and the extension, while also making evident the interesting aspects that appear after inclusion of the extra degree of freedom. We will also elaborate and use information-theoretic tools to study the models and see what it can tell us about them. In section 3.2, we introduce the original model, discuss its phases and symmetries. We will showcase our approach at this level, which includes novel contributions, because the model is simpler. In section 3.3 we introduce a two-mode Dicke model, extending what was done in the preceding section; this is the main part of this work. The extended model displays new phenomena, which will be highlighted in contrast to what is shown in the first section. The third section involves a discussion of the structure of correlations in the phase diagram of the model. To this end we will take advantage of the fact that the states of interest are Gaussian, and thus we review phase space techniques to treat them and relate them to information-theoretic methods of quantum mechanics.

3.2   The one-mode Dicke model

The original model was introduced in refs. [123–125]. It presumes a range of validity, where a countable set of bosonic modes interact resonantly with two levels of a second composite system through a single coupling parameter, collectively. With these conditions determined, parameters in the Dicke model can be further specified, thus reducing it to simpler models, such as the Rabi model [137, 138]; this includes the rotating-wave approximation and a choice of number of degrees of freedom, cf. table 3.1.

The Dicke Hamiltonian is

$$H = \omega a^\dagger a + \omega_0 J_z + \frac{2\lambda}{\sqrt{2j}}(a^\dagger + a)J_x. \tag{3.3}$$

Where the spin operators $\boldsymbol{J} = (J_x, J_y, J_z)$ are a sum of operators for each individual spin-half system indexed by ℓ:

$$\boldsymbol{J} = \sum_\ell \boldsymbol{\sigma}_\ell, \tag{3.4}$$

where $2\boldsymbol{\sigma}$ are the Pauli matrices obeying $[\sigma_i, \sigma_j] = \mathrm{i}\varepsilon_{ijk}\sigma_k$ at each site.

The Hilbert space of the system is the tensor product of a harmonic oscillator Hilbert space $\mathbf{H}_\omega$, where ω labels the mode, and the Hilbert space of an ensemble of N qubits, $\mathbf{H}_N$, which is itself built from the Hilbert space of each qubit, $\mathbf{H}_\ell = \mathbb{C}^2$; in summary,

$$\mathbf{H} = \mathbf{H}_\omega \otimes \mathbf{H}_N, \quad \mathbf{H}_N = \bigotimes_{\ell=1}^{N} \mathbf{H}_\ell \tag{3.5}$$

This models, for example, a lattice of atoms with two energy levels interacting in resonance with a cavity electromagnetic field.

	Number of two-level systems	
	is larger than 1	is equal to 1
No rotating-wave approx.	Dicke	Rabi
W/ rotating-wave approx.	Tavis–Cummings	Jaynes–Cummings

Table 3.1: Table outline of relations between common interacting spin-boson models, starting from the Dicke model. Firstly, by restricting the number of two-level systems to one, one arrives at the Rabi model. Secondly, when the sum of the energy gaps of the two-level systems and mode is comparatively much higher than their difference, specific channels of the spin-boson interaction average to zero over time and can therefore be neglected in particular time scales; this is the regime of the Tavis–Cummings model, and the simplification is termed rotating-wave approximation. Moreover, the two cases just described can be mixed: when the rotating-wave approximation is valid and there is only one two-level system, one arrives at the Jaynes–Cummings model.

The dimension the Dicke model Hilbert space grows exponentially with lattice size, 2^N. A considerable simplification happens, however, since the Hamiltonian H commutes with the total spin operator $J^2 = \boldsymbol{J} \cdot \boldsymbol{J}$, $\left[H, J^2 \right] = 0$. This means that we can characterize the system by the $2j + 1$ states of fixed total quantum number j, in this case known as *cooperation number* [139].

The subspace with the highest degree of degeneracy is that for which j reaches its maximum at $\sum_\ell s_\ell$, where $\sigma_\ell^2 \left| s_\ell, m_\ell \right\rangle = s_\ell(s_\ell + 1) \left| s_\ell, m_\ell \right\rangle$, in units $\hbar = 1$. In our case of interest we have $s_\ell = 1/2$, which by addition of angular momentum leads to $j = N/2$, with magnetic quantum number taking integer steps in the interval $-N/2 \leq m \leq N/2$, totaling $2(N/2) + 1 = N + 1$ states. We will focus on the problem whose Hilbert space is $(N + 1)$-dimensional and spanned by the Dicke states $\left| j = N/2, m \right\rangle$. This means we are dealing with the first component in a

direct sum decomposition of the lattice Hilbert space,

$$\mathbf{H}_N = \mathbf{H}_{j_{\max}} \oplus \mathbf{H}_{j_{\max}-1} \oplus \cdots \oplus \mathbf{H}_{j_{\min}}, \tag{3.6}$$

where $j_{\max} = N/2$, and $j_{\min} = |\sum_\ell (-1)^\ell s_\ell|$, which is ultimately either 0 if N is even or $1/2$ if N is odd.

3.2.1 Quantum phases

To understand the phases of the Dicke model we first perform a few operations on it. First we rotate about the y-axis by θ and then displace the bosonic subspace by α:

$$\widetilde{H} = e^{\mathcal{N}(\alpha^* a - \alpha a^\dagger)} e^{i\theta J_y} H e^{-i\theta J_y} e^{\mathcal{N}(\alpha a^\dagger - \alpha^* a)}, \tag{3.7}$$

where the normalization factor $\mathcal{N} = \sqrt{2j\omega_0/\omega}$ is introduced to make following expressions tidier.

The rotation will affect the spin operators as

$$J_x \mapsto \widetilde{J}_x = J_x \cos\theta - J_z \sin\theta \tag{3.8}$$

$$J_z \mapsto \widetilde{J}_z = J_x \sin\theta + J_z \cos\theta, \tag{3.9}$$

and we choose the displacement of the ladder operator to be

$$a \mapsto \tilde{a} = a + \sqrt{2}\alpha_{\mathcal{N}}, \tag{3.10}$$

where $\alpha_{\mathcal{N}} = \mathcal{N}\alpha$ and $\alpha \in \mathbb{R}$. Notice that $\alpha_{\mathcal{N}}$ is then proportional to j.

The resulting Hamiltonian is

$$\widetilde{H} = \omega \left[a^\dagger a + \sqrt{2}\alpha_\mathcal{N} \left(a^\dagger + a \right) + 2\alpha_\mathcal{N}^2 \right] + \omega_0 (J_x \sin\theta + J_z \cos\theta)$$
$$+ \frac{2\lambda}{\sqrt{2j}} \left(a^\dagger + a + 2\sqrt{2}\alpha_\mathcal{N} \right) (J_x \cos\theta - J_z \sin\theta). \quad (3.11)$$

Relying on the thermodynamic limit $N \to \infty$, we will apply the Holstein–Primakoff representation (see review [140] and references therein), transforming the spin operator algebra into a bosonic algebra through

$$J_z \mapsto j - b^\dagger b \qquad (3.12\text{a})$$

$$J_+ \mapsto \sqrt{2j}\, b^\dagger \left(1 - \frac{b^\dagger b}{2j} \right)^{1/2} \qquad (3.12\text{b})$$

$$J_- \mapsto \sqrt{2j} \left(1 - \frac{b^\dagger b}{2j} \right)^{1/2} b. \qquad (3.12\text{c})$$

This representation utilizes the ladder operators $J_\pm$, such that

$$J_x = \frac{J_+ + J_-}{2}. \qquad (3.13)$$

By expanding the square roots in the definition of $J_\pm$, we can simplify the problem at the thermodynamic limit by ignoring contributions with overall j in the denominator, reducing the Holstein–Primakoff representation effectively to

$$J_+ \approx \sqrt{2j}\, b^\dagger, \qquad (3.14\text{a})$$
$$J_- \approx \sqrt{2j}\, b. \qquad (3.14\text{b})$$

The Hamiltonian becomes

$$
\begin{aligned}
\widetilde{H} \approx{} & \omega \left[a^\dagger a + \sqrt{2}\alpha_{\mathcal{N}} \left(a^\dagger + a \right) + 2\alpha_{\mathcal{N}}^2 \right] \\
& + \omega_0 \left(\sqrt{2j}\frac{(b^\dagger + b)}{2} \sin\theta - (b^\dagger b - j)\cos\theta \right) \\
& + \lambda(a^\dagger + a + 2\sqrt{2}\alpha_{\mathcal{N}}) \left(\frac{(b^\dagger + b)}{\sqrt{2}}\cos\theta - \frac{1}{\sqrt{j}}(b^\dagger b - j)\sin\theta \right).
\end{aligned}
\tag{3.15}
$$

For the next step we will also ignore the cubic term in quadratures,

$$
\widetilde{H}_{(3)} = \frac{2\lambda(a + a^\dagger)bb^\dagger \sin\theta}{\sqrt{2j}},
\tag{3.16}
$$

which carries an overall power of the spin quantum number in the denominator; in comparison with the other contributions, this is the most feeble at large j and for consistency with the thermodynamic limit taken in eq. (3.14a). In addition to this, we regroup to better identify the linear contributions in the bosonic algebra,

$$
\begin{aligned}
\widetilde{H} \approx{} & \omega a^\dagger a + \left(\frac{4\lambda}{\sqrt{2j}}\alpha_{\mathcal{N}}\sin\theta - \omega_0\cos\theta \right) b^\dagger b \\
& + \lambda\cos(\theta)(a^\dagger + a)(b^\dagger + b) \\
& + \left(\omega\alpha_{\mathcal{N}} - \lambda\sin(\theta)\sqrt{2j} \right)(a^\dagger + a) \\
& + \left(\frac{\omega_0\sin(\theta)}{2}\sqrt{2j} + 2\lambda\alpha_{\mathcal{N}}\cos\theta \right)(b^\dagger + b) \\
& + \omega\alpha_{\mathcal{N}}^2 + \omega_0 j\cos\theta - 2\sqrt{2j}\lambda\alpha_{\mathcal{N}}\sin\theta.
\end{aligned}
\tag{3.17}
$$

By demanding that the coefficients of linear terms vanish, we find equations

that will determine $\alpha = \alpha_{\mathcal{N}}/\mathcal{N}$ and θ. We thus have,

$$\alpha\sqrt{\omega\omega_0} - \lambda\sin\theta = 0 \qquad (3.18a)$$

$$4\alpha\lambda\cos\theta + \sqrt{\omega\omega_0}\sin\theta = 0, \qquad (3.18b)$$

whose solutions for α and θ lead to different phases of the system. By isolating α in the first equation, the second one can be rewritten as

$$\omega\omega_0\sin\theta + 4\lambda^2\sin\theta\cos\theta = 0, \qquad (3.19)$$

and then solved for θ. A trivial solution is found for $\theta = \pi$, further implying that $\alpha = 0$: a solution that simply returns the original Dicke Hamiltonian; a non-trivial solution for θ is

$$\begin{aligned} \cos\theta &= -\frac{\omega\omega_0}{4}\frac{1}{\lambda^2} \\ &= -\frac{\lambda_c^2}{\lambda^2}, \end{aligned} \qquad (3.20)$$

where we defined $\lambda_c = \sqrt{\omega\omega_0}/2$. Only for $\lambda > \lambda_c$ this solution is defined. In order to find α we plug this back into eq. (3.18a), yielding

$$\alpha = \frac{\sqrt{\lambda^4 - \lambda_c^4}}{2\lambda\lambda_c}. \qquad (3.21)$$

Notice that for α to take on real values, the coupling parameter also must obey $\lambda > \lambda_c$.

What are these manipulations giving us? By defining $\widetilde{H}$ with respect to the unitaries representing displacement in the bosonic algebra and rotation

in the spin algebra, we equivalently introduce the variational family of states

$$|\alpha, \theta\rangle = e^{-i\theta J_y} e^{\mathcal{N}(\alpha a^\dagger - \alpha^* a)} |0, \uparrow\rangle, \qquad (3.22)$$

where the fiducial state is $|0, \uparrow\rangle = |0\rangle \otimes |\uparrow\rangle$: the tensor product of the ground state of the free Hamiltonian $\omega a^\dagger a$ and the eigenstate of $\omega_0 J_z$ with the largest eigenvalue $|\uparrow\rangle = |j, m = j\rangle$.[a]

The term proportional to the identity in $\widetilde{H}$, call it $\mathcal{V}(\alpha, \theta)$, turns out to be $\langle \alpha, \theta | H | \alpha, \theta\rangle$: the expectation value of energy on bosonic and spin coherent states.[b] In a variational approach the ground state energy E_0 works as a lower bound to $\mathcal{V}(\alpha, \theta) \geq E_0$. Therefore, by minimizing $\mathcal{V}$ we can find the ground state energy, and for as long as the manifold of ground states is a submanifold of the coherent states, we can find the coordinates (α, θ) for the ground state itself [141].

How was this done? We have minimized the term $\mathcal{V}$ by finding the zeros of the coefficients of the linear terms $\#(a + a^\dagger)$ and $\#(b + b^\dagger)$. The fact that higher-order polynomial terms in the algebra of operators come accompanied by gradients of the corresponding group variables is made evident by using the Baker–Campbell–Hausdorff (BCH) formula, $e^{xX} Y e^{-xX} = Y + x[X, Y] + (x^2/2!)[X, [X, Y]] + \ldots$; from this, we can see that higher-order commutators come alongside cumulative integrations of the coefficients over the variable x. Commutators, on the other hand, are derivations in the algebra of operators, so the effect of higher-order commutators in X is to

---

[a]This family are the group-theoretic coherent states of the Heisenberg algebra $\mathfrak{h}$ and the spin $\mathfrak{su}(2)$ algebra. See [141] for a treatment of variational methods that introduces these states.

[b]In fact, it already involves a particular choice of parameters. The spin coherent states are parametrized by two variables, θ and ϕ, but the second ends up not playing a role because of the breaking of a symmetry, and so we set it $\phi = 0$, which hides a factor $\cos \phi = 1$ from the $\sin \theta$ term; more on this later.

decrease the monomial order of Y in X, e.g. $\left[a^n, a^\dagger\right] = \partial a^n / \partial a = n a^{n-1}$. In our case, the BCH formula soon truncates in the bosonic algebra, whilst culminating in a rotation in the spin algebra. Although not as clear in terms of $\boldsymbol{J}$, the Holstein–Primakoff representation and the thermodynamic limit make this effect evident.

To conclude, define $\widetilde{H}$ (in the thermodynamic limit) as

$$\widetilde{H} = \widetilde{H}^{(0)} + \widetilde{H}^{(1)} + \widetilde{H}^{(2)}, \tag{3.23}$$

where k in $\widetilde{H}^{(k)}$ is the monomial order in the variables $(a, a^\dagger, b, b^\dagger)$, with coefficients $\widetilde{K}^{i_1, \dots, i_n, \dots i_k}$. From this definition we see that $\widetilde{H}^{(2)}$ is the original Dicke Hamiltonian, with $\widetilde{K}^{ij}$ its coefficients. If we now make the following identification:

$$\widetilde{K}^{ij} = \frac{\partial^2 \mathcal{V}}{\partial z_i \partial z_j}, \tag{3.24}$$

where $z = (\alpha, \alpha^*, \theta, \phi)$, then the other terms are $\widetilde{K}^i = \partial \mathcal{V} / \partial z_i$ and, ultimately, $\widetilde{K} = \mathcal{V}$. In summary, because the Hamiltonian is quadratic, we have the whole set of derivatives of $\mathcal{V}$ to solve a minimization problem over it.

Why is this minimization important? Phase transitions are then identified by non-analytic behavior of the free energy $F = -\beta^{-1} \ln Z$, for partition function $Z = \operatorname{tr} e^{-\beta H}$, in the thermodynamic limit. In the low temperature limit, $\beta \to \infty$, the ground state energy equals the free energy, $e^{-\beta F} = e^{-\beta E_0} + e^{-\beta E_1} \dots$, because larger spectral values are exponentially suppressed. Thus, by finding non-analytic behavior of E_0, we interpret it as a region of quantum phase transition.

We have just shown two things: first, the minimization over $\psi = (\alpha, \theta)$ implies that the ground state energy depends on this coherent state

parameter; secondly, the solution of the minimization problem shows that $\psi = \psi(\lambda)$. But more importantly, the ground state energy may change with the parameters in the Hamiltonian; in particular $E_0 = E_0(\lambda)$. Therefore, we find $E_0(\lambda)$ by finding $E_0(\psi)$ and knowing $\psi(\lambda)$, that is: $E_0(\lambda) = E_0(\psi(\lambda))$. This minimum of the energy functional is found to be

$$(2j)^{-1} \min_{(\alpha,\theta)} \mathcal{V} = (2j)^{-1} E_0(\lambda) = \begin{cases} -\dfrac{2\lambda_c^2}{\omega}, & \text{if } \lambda < \lambda_c, \\ -\dfrac{(\lambda^4 + \lambda_c^4)}{\lambda^2 \omega}, & \text{if } \lambda \geq \lambda_c. \end{cases} \tag{3.25}$$

Whilst E_0 is continuous at the point of transition, $\lambda = \lambda_c$, its first derivative with respect to λ is discontinuous: this is a first-order quantum phase transition.

Crucially, the solution $\psi = (0, \pi)$ is valid for every parameter λ, not only for those greater than the critical value, but it can be shown to be a local maximum instead of a minimum in that region (a full treatment of the minimization problem, resolving this issue, would also involve an analysis of the second derivatives, determining which values correspond to saddle points, maxima, etc.). See section 3.2.2, fig. 3.2, for a graphical visualization of this.

Diagonalizing the Hamiltonian. Instead of going straight for the full solutions $\psi_i = (\alpha_i, \theta_i)$, where $i = \text{NP, SP}$, we aim at a partial solution in α by writing $\theta = \theta(\alpha)$, such that $\theta(\alpha_i) = \theta_i$. This leads to

$$\widetilde{H} = \mathcal{V}(\alpha) + \omega a^\dagger a + \Omega(\alpha) b^\dagger b + \Lambda(\alpha)(a^\dagger + a)(b^\dagger + b), \tag{3.26}$$

where

$$\Omega(\alpha) = \frac{4\lambda_c^2}{\omega}\left(4\alpha^2 - \sqrt{1 + \frac{\alpha^2\lambda_c^2}{\lambda^2}}\right) \tag{3.27a}$$

$$\Lambda(\alpha) = \lambda\sqrt{1 + \frac{\alpha^2\lambda_c^2}{\lambda^2}}, \tag{3.27b}$$

and not forgetting that $\alpha = \alpha(\lambda)$. By diagonalizing this Hamiltonian, we will have the diagonalized form in both phases, provided that we plug the appropriate solution form of α in each case.

This may be identified with a general two-mode squeezed Hamiltonian. The diagonalization of this operator is achieved after introducing the quadratures

$$q_a = \frac{a^\dagger + a}{\sqrt{2\omega}}, \quad p_a = i\sqrt{\frac{\omega}{2}}\left(a^\dagger - a\right) \tag{3.28}$$

$$q_b = \frac{b^\dagger + b}{\sqrt{2\Omega}}, \quad p_b = i\sqrt{\frac{\Omega}{2}}\left(b^\dagger - b\right). \tag{3.29}$$

In these coordinates, the Hamiltonian is

$$\widetilde{H} = \mathcal{V}(\alpha) + \frac{\boldsymbol{p}^\mathsf{T}\boldsymbol{p}}{2} + \frac{1}{2}\boldsymbol{q}^\mathsf{T}V\boldsymbol{q}, \quad \boldsymbol{q} = \begin{pmatrix} q_a \\ q_b \end{pmatrix} \quad \text{and} \quad \boldsymbol{p} = \begin{pmatrix} p_a \\ p_b \end{pmatrix}, \tag{3.30}$$

where

$$V = \begin{pmatrix} \omega^2 & -2\Lambda\sqrt{\omega\Omega} \\ -2\Lambda\sqrt{\omega\Omega} & \Omega^2 \end{pmatrix} \tag{3.31}$$

By rotating the canonical coordinates with the matrix

$$S = \begin{pmatrix} \cos\chi & -\sin\chi \\ \sin\chi & \cos\chi \end{pmatrix}, \tag{3.32}$$

by the angle χ such that

$$\tan\chi = \frac{4\Lambda\sqrt{\omega\Omega}}{\Omega^2 - \omega^2 + \sqrt{16\Lambda^2\omega\Omega + \omega^4 - 2\omega^2\Omega^2 + \Omega^4}}, \tag{3.33}$$

thus defining $Q = Sq$ and $P = Sp$. This leads to the diagonal Hamiltonian

$$\widetilde{H} = \frac{1}{2}\sum_{k\in\{+,-\}} P_k^2 + \nu_k^2 Q_k^2, \tag{3.34}$$

with

$$\nu_\pm^2 = \frac{\omega^2 + \Omega^2}{2} \pm \frac{1}{2}\sqrt{16\Lambda^2\omega\Omega + \omega^4 - 2\omega^2\Omega^2 + \Omega^4}. \tag{3.35}$$

The values corresponding to each phase is found by plugging in $\Omega(\alpha_{NP,SP})$ and $\Lambda(\alpha_{NP,SP})$.

3.2.2 Symmetries of the model

The original Dicke Hamiltonian,

$$H = \omega a^\dagger a + \omega_0 J_z + \frac{2\lambda}{\sqrt{2j}}\left(a^\dagger + a\right) J_x,$$

is invariant under the transformations

$$a \mapsto -a \tag{3.36}$$

$$J_x \mapsto -J_x, \tag{3.37}$$

thus constituting the $\mathbb{Z}_2$ parity symmetry of the system. The generator of this symmetry is

$$N = a^\dagger a + J_z + j, \tag{3.38}$$

which exponentiates to the unitary transformation

$$\Pi = e^{-\mathrm{i}\pi N}. \tag{3.39}$$

Because this is a symmetry, $[H, \Pi] = 0$.

Recall now that the following form of the Hamiltonian,

$$\widetilde{H} = \mathcal{V}(\alpha, \theta) + \omega a^\dagger a + \Omega(\alpha) b^\dagger b + \Lambda(\alpha)(a^\dagger + a)(b^\dagger + b) \tag{3.40}$$

is *not* invariant under the same symmetry. To better compare the symmetries and phases, the parity symmetry operator in the Holstein–Primakoff representation is

$$\Pi = \exp\big[-\mathrm{i}\pi(a^\dagger a + b^\dagger b)\big]. \tag{3.41}$$

This breaking of symmetry follows because Π must also be rotated and displaced. In the Holstein–Primakoff representation, the rotation about the y axis corresponds to a displacement of the b ladder operators, i.e.

$$
\begin{aligned}
\widetilde{\Pi} &= e^{\alpha^* a - \alpha a^\dagger} e^{\beta^* b - \beta b^\dagger} \Pi e^{\beta b^\dagger - \beta^* b} e^{\alpha a^\dagger - \alpha^* a} \\
&= \exp\big(-\mathrm{i}\pi[a^\dagger a + \alpha(a^\dagger + a) + 2\alpha + b^\dagger b + \beta(b^\dagger + b) + 2\beta]\big).
\end{aligned}
\tag{3.42}
$$

The transformed parity $\widetilde{\Pi}$ involves linear terms in a and b, hence it affects $\widetilde{H}$ in non-trivial ways. In the new variables $\tilde{a}$ and $\tilde{b}$, this is just $\widetilde{\Pi} = \exp[-i\pi(\tilde{a}^\dagger \tilde{a} + \tilde{b}^\dagger \tilde{b})]$.

We could however write a *new* unitary transformation in the a and b algebras,

$$\Pi' = \exp\left[-i\pi(a^\dagger a + b^\dagger b)\right], \tag{3.43}$$

that transforms by conjugation $\widetilde{H}$ exactly as Π previously transformed H. In summary, $[H, \Pi] = 0$ leads to $[\widetilde{H}, \widetilde{\Pi}] \neq 0$, whilst $[\widetilde{H}, \Pi'] = 0$.

Let us look now at the constant term in the Hamiltonian, this is the energy in absence of fluctuations:

$$\frac{\mathcal{V}(\alpha, \theta)}{2j} = \frac{4\lambda_c^2}{\omega}\alpha^2 - \frac{4\lambda\lambda_c}{\omega}\alpha \sin\theta + \frac{2\lambda_c^2}{\omega}\cos\theta. \tag{3.44}$$

Rewriting θ in terms of α,

$$\begin{aligned}
\sin\theta &= \sin(\pi - \arcsin(2\alpha\lambda_c/\lambda)) \\
&= \frac{2\alpha\lambda_c}{\lambda},
\end{aligned} \tag{3.45}$$

leads to

$$\frac{\mathcal{V}(\alpha, \theta(\alpha))}{2j} = \frac{\mathcal{V}(\alpha)}{2j} = -\frac{2\lambda_c^2}{\omega}\left(2\alpha^2 + \sqrt{1 - \frac{4\alpha^2\lambda_c^2}{\lambda^2}}\right), \tag{3.46}$$

ultimately reducing to the minimum of energy we had in eq. (3.25).

For $\alpha \ll 1$, and neglecting the constant term, we can approximate $\mathcal{V}(\alpha)$ as

$$\mathcal{V}(\alpha) = -\frac{2\lambda_c^2}{\omega}\left[1 + \left(2 - \frac{2\lambda_c^2}{\lambda^2}\right)\alpha^2 - \frac{2\lambda_c^4}{\lambda^4}\alpha^4 + O(\alpha^6)\right], \tag{3.47}$$

and recognize a quartic potential paradigmatic of spontaneous symmetry breaking and the theory of phase transitions of Landau. It is important to notice that $\alpha \ll 1$ means different things in each phase, i.e. whether $\lambda > \lambda_c$ or $\lambda < \lambda_c$. In the normal phase α is identically zero, so the expression above is exact there. In the superradiant phase, however, α depends on λ: being small translates to small $\lambda^{-1}\sqrt{\lambda^4 - \lambda_c^4} \ll 2\lambda_c$; the expression will give decent approximations in this regime. Nonetheless, we plot the full potential as function of α in fig. 3.2 and show the appearance of two minima when λ is varied and reaches the superradiant phase.

Although not visible from the plot, by varying λ a second-order phase transition is displayed, meaning that the second derivative of E_0 with respect to the coupling parameter is discontinuous at the point of transition.

3.3 A two-mode Dicke model

We can consider a modified version of the Dicke Hamiltonian (3.3), whose symmetry group is larger, namely the continuous group U(1). It is usual to discuss this group in the context of the Dicke model under the rotating wave approximation, for which the counter-rotating terms $a^\dagger b^\dagger$ and ab are neglected; we consider instead a model with *more* degrees of freedom:

$$H = \omega a_x^\dagger a_x + \omega a_y^\dagger a_y + \omega_0 J_z + \frac{\lambda_x}{\sqrt{2j}}(a_x^\dagger + a_x)J_x + \frac{\lambda_y}{\sqrt{2j}}(a_y^\dagger + a_y)J_y,$$
$$(3.48)$$

representing a sum of Dicke models, one for each component of the collective spin. That is, $H = H_x + H_y$ where each H_i is similar to eq. (3.3), but with each mode coupling to different sectors of the spin degrees of
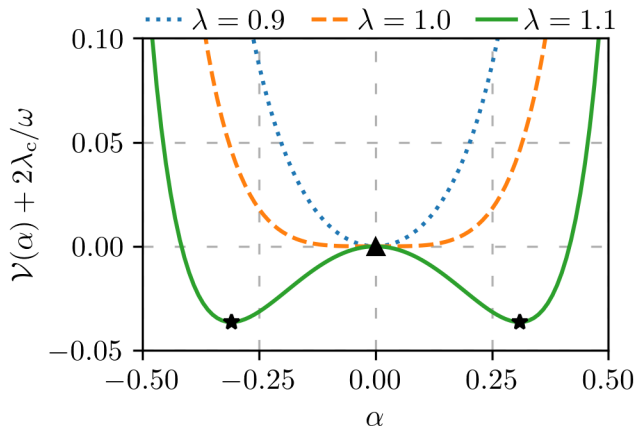
Figure 3.2: Plot of the energy functional $\mathcal{V}(\alpha) = \mathcal{V}(\alpha, \theta(\alpha))$. The minima occur at different α (and θ) for different λ. Below the critical point there is a unique minimum, indicated by a triangle, whilst above that point there are two (with star labels), thus breaking the parity symmetry of the Hamiltonian. The plot is shifted with respect to the normal phase ground state, meaning the minimum happens at zero in this phase. But the shift taking E_0 to zero cannot be done simultaneously for every α, and thus E_0 is non-zero in the superradiant phase. Plot made for $\lambda_c = 1$ and $\omega = 1$.

freedom.

We can treat this Hamiltonian by considering quadratures associated to the field ladder operators,

$$q_i = \frac{a_i + a_i^\dagger}{\sqrt{2}}, \quad p_i = \frac{a_i - a_i^\dagger}{i\sqrt{2}}, \tag{3.49}$$

as well as for the spin operators,

$$J_x = Q\sqrt{j}, \quad J_y = P\sqrt{j}, \quad J_z = j - \frac{(Q^2 + P^2)}{2}, \tag{3.50}$$

reproducing the ladder-to-quadrature relations for the Holstein–Primakoff representation at large j: $J_+ \approx \sqrt{2j}\, b^\dagger$, $J_- = J_+^\dagger$ and $J_z = j - b^\dagger b$.

3.3.1 Quantum phases on two coupling parameters

The same steps we had for the $\mathbb{Z}_2$-invariant Dicke model apply here, with slight modifications. First, since we have more degrees of freedom, we need more variables in order to identify the phase transitions. Define a new family of Hamiltonians as

$$\widetilde{H} = D^\dagger(\alpha_y)D^\dagger(\alpha_x)e^{i\phi J_z}e^{i\theta J_y}He^{-i\theta J_y}e^{-i\phi J_z}D(\alpha_x)D(\alpha_y), \tag{3.51}$$

for

$$D(\alpha_i) = \exp\left(\mathcal{N}(\alpha_i^* a_i - \alpha_i a_i^\dagger)\right), \quad \text{for } i = x, y, \tag{3.52}$$

and where $\mathcal{N} = 2\sqrt{j\omega_0/\omega}$. As in section 3.2.1, one arrives at $\widetilde{H}$ whose cubic term in the ladder operators (and quadrature) has an overall suppression of j in the numerator, and at equations determined by vanishing linear

terms.

We are interested in the different solutions available for different values of ϕ. These possibilities are linked to the parameters λ_x and λ_y, as we show in the sections below. On top of this, when working with the quadratures defined above, we perform the rotations

$$q_x \mapsto \cos(\nu)q_x - \sin(\nu)q_y, \quad q_y \mapsto \sin(\nu)q_x + \cos(\nu)q_y. \quad (3.53)$$

This will help us simplify the transformed Hamiltonian at a later stage.

Different coupling across modes.   Let us start again from the transformed Hamiltonian

$$\widetilde{H} = D^\dagger(\alpha_y)D^\dagger(\alpha_x)e^{i\theta J_y}He^{-i\theta J_y}D(\alpha_x)D(\alpha_y), \quad (3.54)$$

which is the same as in eq. (3.51) but with $\phi = 0$ from the outset. We have seen in earlier sections that the value of ϕ is a phase on the (α_x, α_y) plane. We associate this choice of ϕ with the condition $\lambda_x > \lambda_y$, without loss of generality. A second option would be given by $\phi = \pi/2$, for which the condition $\lambda_y > \lambda_x$ would yield equivalent results but for a second phase and phase transition.

We repeat the process of section 3.2.1, finding the conditions under which the linear part $\widetilde{H}_{(1)}$ vanishes, corresponding to a minimization of $\mathcal{V} = \widetilde{H}_{(0)}$ over the family of coherent states $(\alpha_x, \alpha_y, \theta)$. With the chosen set of parameters, there are two possible sets of solutions for these parameters as functions of (λ_x, λ_y). The normal phase solution is given by $(\alpha_x, \alpha_y, \theta) = (0, 0, \pi)$. There are two other solutions, but both for the superradiant phase. They are equivalent; given the arbitrary choice of

positive θ solutions, they are

$$\alpha_x = \alpha_x^+ = \frac{\sqrt{\lambda_x^4 - \lambda_c^4}}{2\lambda_x\lambda_c} \tag{3.55a}$$

$$\alpha_y = 0 \tag{3.55b}$$

$$\theta = \theta_x = \arccos\left(-\frac{\lambda_c^2}{\lambda_x^2}\right). \tag{3.55c}$$

The other solution exchanges the sign of α_x and θ. We notice that this solution only yields a value for $0 \le \theta \le \pi$ when $\sqrt{\omega\omega_0} \le \lambda_x$, which is an indicator of the phase transition. We thus define the critical value $\lambda_c = \sqrt{\omega\omega_0}$, which is twice that for the one-mode Dicke model in section 3.2.

In this case, the ground state energy is

$$(2j)^{-1} E_0(\lambda_x) = \begin{cases} -\dfrac{\lambda_c^2}{2\omega}, & \text{if } \lambda_x < \lambda_c, \\[2ex] -\dfrac{(\lambda_x^4 + \lambda_c^4)}{4\lambda_x^2\omega}, & \text{if } \lambda_x \ge \lambda_c, \end{cases} \tag{3.56}$$

which is independent of λ_y.

These steps are completely analogous for $\phi = \pi/2$ by exchanging x for y, with slight changes in the values of minimizing variables:

$$\alpha_x = 0 \tag{3.57a}$$

$$\alpha_y = \alpha_y^- = -\frac{\sqrt{\lambda_y^4 - \lambda_c^4}}{2\lambda_y\lambda_c} \tag{3.57b}$$

$$\theta = \theta_y = \arccos\left(\frac{\lambda_c^2}{\lambda_y^2}\right), \tag{3.57c}$$

where we have chosen the solution with positive θ.

Normal modes. By choosing the set of values corresponding to the $\lambda_x > \lambda_y$ superradiant phase, $\alpha_x \ (= \alpha_x^+)$ and its accompanying θ, the quadratic Hamiltonian is

$$\widetilde{H}(\alpha_x^+, 0, \theta_x) = H_{SPx}$$

$$= \mathcal{V} + \frac{\omega}{2} \left(p_x^2 + p_y^2 + q_x^2 + q_y^2 \right) + \frac{\lambda_x^2}{2\omega}(P^2 + Q^2) \quad (3.58)$$

$$+ \lambda_y P q_y - \frac{\lambda_c^2}{\lambda_x} Q q_x,$$

Our goal is to find the variables under which the Hamiltonian is expressed as a set of harmonic oscillators, i.e. its normal modes. Let us write H_{SPx} in concise form using matrices

$$H_{SPx}(\boldsymbol{R}) = \frac{1}{2} \boldsymbol{R}^\intercal \widetilde{K} \boldsymbol{R}. \quad (3.59)$$

More explicitly, we have

$$\widetilde{K} = \begin{pmatrix} \omega & 0 & 0 & 0 & -\frac{2\lambda_c^2}{\lambda_x} & 0 \\ 0 & \omega & 0 & 0 & 0 & 0 \\ 0 & 0 & \omega & 0 & 0 & 2\lambda_y \\ 0 & 0 & 0 & \omega & 0 & 0 \\ 0 & 0 & 0 & 0 & \frac{\lambda_x^2}{\omega} & 0 \\ 0 & 0 & 0 & 0 & 0 & \frac{\lambda_x^2}{\omega} \end{pmatrix}, \quad \boldsymbol{R} = \begin{pmatrix} q_x \\ p_x \\ q_y \\ p_y \\ Q \\ P \end{pmatrix}. \quad (3.60)$$

It can be checked that $\widetilde{K}$ is a positive-definite matrix. By Williamson's theorem it is therefore possible to find degrees of freedom through which

$\widetilde{K}$ has a diagonal form. The theorem states that, given a symmetric positive-definite matrix, there exists a symplectic transformation S such that

$$K = S\widetilde{K}S^{\mathsf{T}} \tag{3.61}$$

is diagonal [142]. The diagonal elements are known as symplectic eigenvalues, and we will denote them by ν. See appendix C for an algorithm to find the symplectic eigenvalues and S, and which serves as background for the following discussion.

Before studying S itself, which will ultimately lead us to the eigenstates of $\widetilde{H}$, we can already see the frequencies of oscillations of the normal modes associated to $\widetilde{H}$; they are $\sqrt{r_i}/\lambda_x\omega$, where r_i are the three roots of the following polynomial:[c]

$$r^3 - r^2 \left(2\omega^4\lambda_x^2 + \lambda_x^6\right) + r\left(\omega^4 + 2\lambda_x^4 - \lambda_c^4 - \lambda_x^2\lambda_y^2\right)\lambda_x^4\omega^4$$
$$- \omega^8\lambda_x^4(\lambda_x^4 - \lambda_c^4)(\lambda_x^2 - \lambda_y^2) = 0. \tag{3.62}$$

In the transformed representation, for which the Hamiltonian is

$$\widetilde{H}(\boldsymbol{R} = S^{\mathsf{T}}\widetilde{\boldsymbol{R}}) = \frac{1}{2}\widetilde{\boldsymbol{R}}^{\mathsf{T}}\widetilde{K}\widetilde{\boldsymbol{R}}, \tag{3.63}$$

these symplectic eigenvalues of $\widetilde{K}$ come in multiplicity two; in fact, they are

$$\nu_i = \left|\pm\frac{\sqrt{r_i}}{\lambda_x\omega}\right| = \frac{\sqrt{r_i}}{\lambda_x\omega}, \quad i = 1, 2, 3, \tag{3.64}$$

---

[c]The explicit values of these roots are not very enlightening, however, and it is sufficient to approach the problem numerically, more on this later.

such that, in block form,

$$K = \begin{pmatrix} k_1 & & \\ & k_2 & \\ & & k_3 \end{pmatrix}, \quad k_i = \begin{pmatrix} \nu_i & 0 \\ 0 & \nu_i \end{pmatrix}. \tag{3.65}$$

The doubling of these eigenvalues is justified in the algorithm in appendix C.

Explicitly in these variables, the Hamiltonian is

$$\widetilde{H}(\boldsymbol{R} = S^\mathsf{T}\widetilde{\boldsymbol{R}}) = \mathcal{V} + \frac{\nu_1}{2}(\tilde{p}_x{}^2 + \tilde{q}_x{}^2) + \frac{\nu_2}{2}(\tilde{p}_y{}^2 + \tilde{q}_y{}^2) + \frac{\nu_3}{2}(\widetilde{P}^2 + \widetilde{Q}^2), \tag{3.66}$$

This transformation can be equivalently described in terms of unitaries implementing an active transformation, thereby using the original variables $\boldsymbol{R}$. The unitary action implementing this procedure define a third Hamiltonian $\hat{H}$ as follows:

$$\hat{H}(\boldsymbol{R}) = U^\dagger \widetilde{H}(\boldsymbol{R}) U = \widetilde{H}(U^\dagger \boldsymbol{R} U), \tag{3.67}$$

where $U^\dagger \boldsymbol{R} U = S^\mathsf{T} \boldsymbol{R}$, and we then absorb S into $\widetilde{K}$, finally getting $\hat{H} = \boldsymbol{R}^\mathsf{T} K \boldsymbol{R}/2$. The Hamiltonian $\hat{H}$ is a set of three mutually commuting harmonic oscillators, thus having known spectrum:

$$E(n_x, n_y, n_j) = \nu_1\left(n_x + \frac{1}{2}\right) + \nu_2\left(n_y + \frac{1}{2}\right) + \nu_3\left(n_j + \frac{1}{2}\right) + \mathcal{V}. \tag{3.68}$$

This procedure is general and does not depend on parameters in the Hamiltonian. It is thus applicable to the case where $\lambda_y > \lambda_x$, and also in both normal and superradiant phases. It will only fail at the Goldstone line, $\lambda_x = \lambda_y > \lambda_c$ because there the coupling matrix is not positive-definite, and therefore Williamson's theorem does not apply. We will deal with

this case in the next section. For now, I close this part with the coupling matrices in the remaining regions of the phase diagram: the normal phase and the superradiant phase at $\lambda_y > \lambda_x$.

$$
\begin{aligned}
\widetilde{K}_{\mathrm{NP}} &=
\begin{pmatrix}
\omega & 0 & 0 & 0 & \lambda_x & 0 \\
0 & \omega & 0 & 0 & 0 & 0 \\
0 & 0 & \omega & 0 & 0 & \lambda_y \\
0 & 0 & 0 & \omega & 0 & 0 \\
\lambda_x & 0 & 0 & 0 & \frac{\lambda_c^2}{\omega} & 0 \\
0 & 0 & \lambda_y & 0 & 0 & \frac{\lambda_c^2}{\omega}
\end{pmatrix}, \\[2mm]
\widetilde{K}_{\mathrm{SP}y} &=
\begin{pmatrix}
\omega & 0 & 0 & 0 & 0 & \lambda_x \\
0 & \omega & 0 & 0 & 0 & 0 \\
0 & 0 & \omega & 0 & \frac{\lambda_c^2}{\lambda_y} & 0 \\
0 & 0 & 0 & \omega & 0 & 0 \\
0 & 0 & \frac{\lambda_c^2}{\lambda_y} & 0 & \frac{\lambda_y^2}{\omega} & 0 \\
\lambda_x & 0 & 0 & 0 & 0 & \frac{\lambda_y^2}{\omega}
\end{pmatrix}.
\end{aligned}
\tag{3.69}
$$

Equal coupling across modes.   Let us take a step back to eq. (3.51). We can keep the ϕ rotation arbitrary, and ask for what values of the remaining parameters $(\alpha_x, \alpha_y, \theta)$ the linear part of the Hamiltonian vanishes. A new set of solutions exists in this case, when $\lambda_x = \lambda_y = \lambda$.

The solutions come with redundancy, and by choosing the set with

(a)

(b)

(c)

(d)
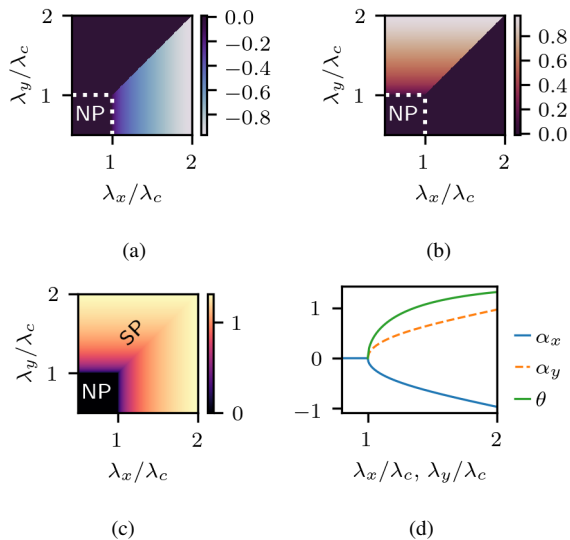
Figure 3.3: Plot of order parameters for the Dicke model displaying the normal, the two superradiant phases and their split at the diagonal line, region of broken continuous symmetry.

positive θ, for convention, we have

$$\alpha_x = \frac{\cos\phi}{2\lambda\lambda_c}\sqrt{\lambda^4 - \lambda_c^4} \tag{3.70a}$$

$$\alpha_y = -\frac{\sin\phi}{2\lambda\lambda_c}\sqrt{\lambda^4 - \lambda_c^4} \tag{3.70b}$$

$$\theta = \arccos\left(-\frac{\lambda_c^2}{\lambda^2}\right), \tag{3.70c}$$

for $0 \le \phi < 2\pi$.

We can repeat the analysis of the constant term in $\widetilde{H}$, $\mathcal{V}$. By eliminating θ and ϕ in favor of α. The ϕ dependence on α will depend on which quadrant it lies. Without loss of generality, by choosing $0 \le \phi < \pi/2$, we have

$$\theta = -\arctan\left(\frac{2\lambda_c\sqrt{\alpha_x^2 + \alpha_y^2}}{\lambda}\right) \tag{3.71}$$

$$\phi = -\arctan\left(\frac{\alpha_y}{\alpha_x}\right), \tag{3.72}$$

one finds

$$\frac{\mathcal{V}}{2j} = -\frac{\lambda_c^2}{2\omega}\left(\sqrt{1 - \frac{4\lambda_c^2(\alpha_x^2 + \alpha_y^2)}{\lambda^2}} + 2(\alpha_x^2 + \alpha_y^2)\right), \tag{3.73}$$

which turns out to be rotationally invariant in the (α_x, α_y) plane. Let us complexify this plane by working with the new coordinate $\Phi = \alpha_x + i\alpha_y$. In these terms, the potential is just a function of $|\Phi|^2$, being once again a potential with symmetry-breaking, non-trivial minima at $|\Phi| \ne 0$ for $\lambda > \lambda_c$. See fig. 3.4 for a plot of this function over the complex (α_x, α_y)
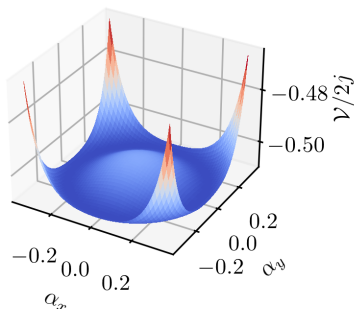
Figure 3.4: Plot of $\mathcal{V}(\alpha)/2j$ potential with parameters $\lambda_c = 1$, $\lambda = 1.1$, and $\omega = 1$. The minimum occurs at a circle in the dark shaded region. Provided $\alpha_x^2 + \alpha_y^2$ is small, meaning $\lambda \approx \lambda_c$, this potential can be approximated by the paradigmatic Mexican hat potential.

plane.

But that is not all. Differently from the one-mode Dicke model, the degenerate ground states at the superradiant phase form a smooth manifold, a consequence of breaking the continuous $U(1)$ symmetry of the Hamiltonian. We thus see, in accordance with Goldstone's theorem, that the system becomes gapless in this $\lambda_x = \lambda_y = \lambda \geq \lambda_c$ regime. The different ϕ values label each point in the ground state manifold, and we can then write $\Phi = \left|\alpha_x^2 + \alpha_y^2\right| e^{-i\phi}$. At any of these points the potential is minimized and equals the value in eq. (3.56) for the $\lambda_x = \lambda_y$ limit, being

$$(2j)^{-1} E_0(\lambda) = -\frac{(\lambda^4 + \lambda_c^4)}{4\lambda^2 \omega}, \tag{3.74}$$

where $\lambda_x = \lambda_y = \lambda \geq \lambda_c$.

Phase diagram. In any region in the parameter manifold the Hamiltonian can be defined through the following quadratic form in the quadrature basis:

$$
\widetilde{K} =
\begin{pmatrix}
\frac{\omega}{2} & 0 & 0 & 0 & \Lambda_1 & \Lambda_2 \\
0 & \frac{\omega}{2} & 0 & 0 & 0 & 0 \\
0 & 0 & \frac{\omega}{2} & 0 & \Lambda_3 & \Lambda_4 \\
0 & 0 & 0 & \frac{\omega}{2} & 0 & 0 \\
\Lambda_1 & 0 & \Lambda_3 & 0 & \frac{\Omega}{2} & 0 \\
\Lambda_2 & 0 & \Lambda_4 & 0 & 0 & \frac{\Omega}{2}
\end{pmatrix},
\tag{3.75}
$$

with some coefficients vanishing at specific parts of the phase diagram. It is particularly important to point out that $\Omega \to 0$ in the limit $\lambda_x = \lambda_y \geq \lambda_c$ (the Goldstone line).

This quadratic form can generally be diagonalized by symplectic matrices. These values represent the energy of collective spin-boson excitations. The lowest eigenvalue in each phase, which we will take to be ν_3,[d] gives the excitations which least departs from the ground state, yielding the first gap in the energy spectrum. The ground state energies, eq. (3.56) and its y variant, are of the order of $\mathcal{O}(j^1)$ whilst the rest of the Hamiltonian used to numerically obtain ν_3 is of order $\mathcal{O}(j^0)$, implying that at $j \to \infty$ they are quasi-continuous compared to $\mathcal{V}$, cf. [139]. In this sense we are modelling small quantum excitations over the classical ground state of each phase.

Figure 3.5 shows the low-lying excitation energy ν_3 as a function of the coupling parameters. The lines separating the phases form a square at $\lambda_{x,y} = \lambda_c$ for $\lambda_{y,x} < 1$. The region adjacent to the origin is the normal phase, and for the complement of this region the system is in the superradiant phase. At the critical lines ν_3 vanishes as a sign of the phase transition.

---

[d]The index represents the relative position in the ordered phase space basis. Since it is the smallest value, it is placed last.
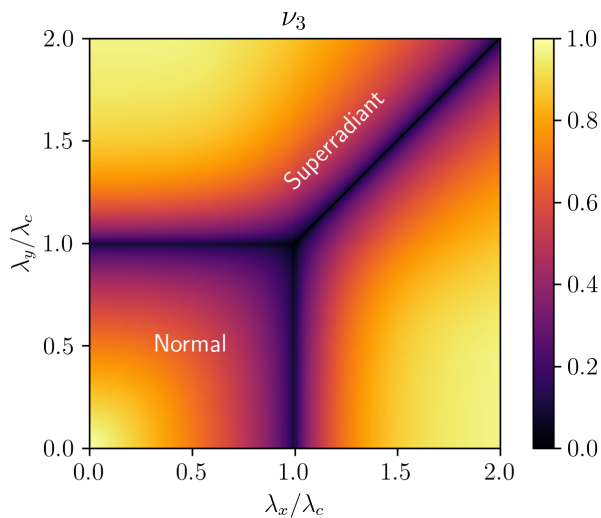
Figure 3.5: Phase diagram for the smallest symplectic eigenvalue ν_3. The region $(\lambda_x < \lambda_c, \lambda_y < \lambda_c)$ shows this excitation energy at the normal phase, whilst for any one of the couplings that cross the value of λ_c, the diagram represents the superradiant phase. $\omega = 1$.
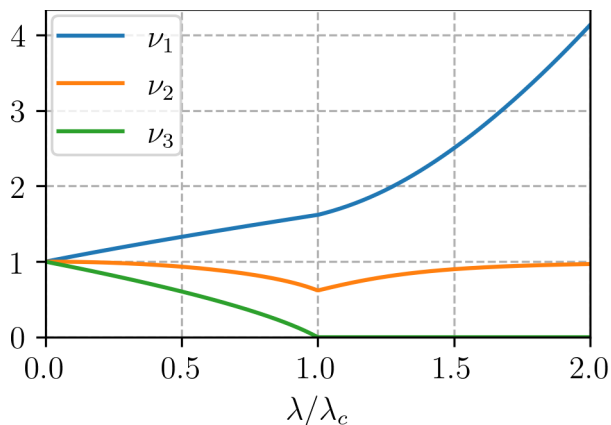
Figure 3.6: Modes along the diagonal, for $\omega = 1$ and in both phases.

At the superradiant regime, the diagram is split at $\lambda_x = \lambda_y$ by a line where the $U(1)$ symmetry is spontaneously broken. The vanishing of ν_3 on this line of the parameter manifold stem from the breaking of the continuous symmetry as dictated by Goldstone's theorem. On this region the ν_3 excitations are massless Goldstone modes. By slicing the plots of ν_i along the diagonal, we can also see the gap behavior at a transition from the normal phase to the Goldstone line, see fig. 3.6.

3.4   Correlation profile of the two-mode model

Since the Hamiltonians are unitarily equivalent, they share the same eigenvalues, and the eigenkets of H are

$$|0\rangle = U_1^\dagger U_2^\dagger |\hat{0}\rangle , \qquad (3.76)$$

where

$$U_1^\dagger = e^{-i\theta J_y} D(\alpha_x) D(\alpha_y), \tag{3.77}$$

and U_2 can be determined by finding the symmetric matrix M such that

$$S = e^{\Omega M} \tag{3.78}$$

and writing

$$U_2 = \exp\left(\frac{i}{2} \boldsymbol{R}^\intercal M \boldsymbol{R}\right). \tag{3.79}$$

We are interested in the properties of a ground state

$$\varrho = |0\rangle\langle 0|, \tag{3.80}$$

but with the form H takes through the unitaries indicated above, we can write a second state

$$\hat{\varrho} = U_2 U_1 |0\rangle\langle 0| U_1^\dagger U_2^\dagger. \tag{3.81}$$

Since they are connected through unitaries, we can relate expectation values simply. Let $\langle \mathcal{O} \rangle = \mathrm{tr}(\mathcal{O}\varrho)$ and $\langle \mathcal{O} \rangle_{\hat{\varrho}} = \mathrm{tr}(\mathcal{O}\hat{\varrho})$, we have for instance,

$$
\begin{aligned}
\langle f(\boldsymbol{R}_i) \rangle &= \langle U_2^\dagger U_1^\dagger f(\boldsymbol{R}_i) U_1 U_2 \rangle_{\hat{\varrho}} \\
&= \langle f(U_2^\dagger U_1^\dagger \boldsymbol{R}_i U_1 U_2) \rangle_{\hat{\varrho}} \\
&= \langle f(\hat{\boldsymbol{R}}_i) \rangle_{\hat{\varrho}}.
\end{aligned}
\tag{3.82}
$$

By knowing the action of the unitaries on the quadratures, $\hat{\boldsymbol{R}}_i = S_{ij}(\boldsymbol{R}_j + A_j)$, where A_j is the column matrix that translates $\boldsymbol{R}$ according to U_1, we can express $\langle f(\boldsymbol{R}_i) \rangle$ with the help of S and A, and with the knowledge of relevant expectation values of observables in the thermal state of a harmonic

oscillator (as this is the form $\hat{\varrho}$ takes). The simplest example is

$$\langle \boldsymbol{R}_i \rangle = \langle [U_2^\dagger (\boldsymbol{R} + A)U_2]_i \rangle_{\hat{\varrho}} \tag{3.83}$$

$$= \langle (U_2^\dagger \boldsymbol{R} U_2)_i + A_i \rangle_{\hat{\varrho}} \tag{3.84}$$

$$= \langle S_{ij} \boldsymbol{R}_j + A_i \rangle_{\hat{\varrho}} \tag{3.85}$$

$$= S_{ij} \langle \boldsymbol{R}_j \rangle_{\hat{\varrho}} + A_i. \tag{3.86}$$

We can simplify this by expressing $\boldsymbol{R}$ as creation and annihilation operators, from what follows that $\langle \boldsymbol{R}_j \rangle_{\hat{\varrho}} = \text{tr}(\boldsymbol{R}_j \hat{\varrho}) = 0$, evident when the trace is computed in terms of eigenvalues of the number operator. Therefore,

$$\langle \boldsymbol{R}_i \rangle = A_i. \tag{3.87}$$

A more interesting computation is

$$\begin{aligned} \langle \boldsymbol{R}_i \boldsymbol{R}_j \rangle &= \langle (S_{ik} \boldsymbol{R}_k + A_i)(S_{jl} \boldsymbol{R}_l + A_j) \rangle_{\hat{\varrho}} \\ &= S_{ik} S_{jl} \langle \boldsymbol{R}_k \boldsymbol{R}_l \rangle_{\hat{\varrho}} + S_{ik} \langle \boldsymbol{R}_k \rangle_{\hat{\varrho}} A_j + S_{jl} A_i \langle \boldsymbol{R}_l \rangle_{\hat{\varrho}} + A_i A_j \\ &= S_{ik} S_{jl} \langle \boldsymbol{R}_k \boldsymbol{R}_l \rangle_{\hat{\varrho}} + A_i A_j. \end{aligned} \tag{3.88}$$

We can express these quantities more concisely in terms of the covariance matrix $\text{cov}(\boldsymbol{R}_i, \boldsymbol{R}_j) = \langle \{ \boldsymbol{R}_i - \langle \boldsymbol{R}_i \rangle, \boldsymbol{R}_j - \langle \boldsymbol{R}_j \rangle \} \rangle$. In the $\hat{\varrho}$ state it is

$$\text{cov}_{\hat{\varrho}}(\boldsymbol{R}_i, \boldsymbol{R}_j) = \langle \{ \boldsymbol{R}_i, \boldsymbol{R}_j \} \rangle_{\hat{\varrho}}, \tag{3.89}$$

since $\langle \boldsymbol{R}_j \rangle_{\hat{\varrho}} = 0$. The first moments in the state ϱ do not vanish however,

and hence the associated covariance is more complicated:

$$
\begin{aligned}
\mathrm{cov}(\boldsymbol{R}_i, \boldsymbol{R}_j) &= \langle \boldsymbol{R}_i \boldsymbol{R}_j + \boldsymbol{R}_j \boldsymbol{R}_i - 2 \langle \boldsymbol{R}_i \rangle \boldsymbol{R}_j \\
&\quad - 2 \langle \boldsymbol{R}_j \rangle \boldsymbol{R}_i - 2 \langle \boldsymbol{R}_i \rangle \langle \boldsymbol{R}_j \rangle \rangle \\
&= \langle \{ \boldsymbol{R}_i, \boldsymbol{R}_j \} \rangle - 2 \langle \boldsymbol{R}_i \rangle \langle \boldsymbol{R}_j \rangle ,
\end{aligned}
\tag{3.90a}
$$

which can be expressed in terms of A as

$$
= \langle \{ \boldsymbol{R}_i, \boldsymbol{R}_j \} \rangle - 2 A_i A_j.
\tag{3.90b}
$$

From eq. (3.88) we can infer that

$$
\langle \{ \boldsymbol{R}_i, \boldsymbol{R}_j \} \rangle = S_{ik} S_{jl} \langle \{ \boldsymbol{R}_k, \boldsymbol{R}_l \} \rangle_{\hat{\varrho}} + 2 A_i A_j.
\tag{3.91}
$$

Inserting this in the expression for $\mathrm{cov}(\boldsymbol{R}_i, \boldsymbol{R}_j)$ yields, in terms of $\mathrm{cov}_{\hat{\varrho}}(\boldsymbol{R}_i, \boldsymbol{R}_j)$,

$$
\mathrm{cov}(\boldsymbol{R}_i, \boldsymbol{R}_j) = S_{ik} S_{jl} \, \mathrm{cov}_{\hat{\varrho}}(\boldsymbol{R}_k, \boldsymbol{R}_l).
\tag{3.92}
$$

The covariance of quadratures in the ground state of three harmonic oscillators is simple, being just an identity matrix, $\mathrm{cov}_{\hat{\varrho}}(\boldsymbol{R}_k, \boldsymbol{R}_l) = \delta_{kl}/2$. With this given the quadratures have, in ground state of H, the following covariance matrix:

$$
\mathrm{cov}(\boldsymbol{R}_i, \boldsymbol{R}_j) = S_{ik} S_{jk}/2.
\tag{3.93}
$$

Notice that here we are taking a different path from the transformations introduced when doing the symplectic diagonalization. There, the symplectic S transforms a non-diagonal quadratic form to its diagonal counterpart. Here we are writing the non-diagonal covariance matrix, starting from its

(a)

(b)
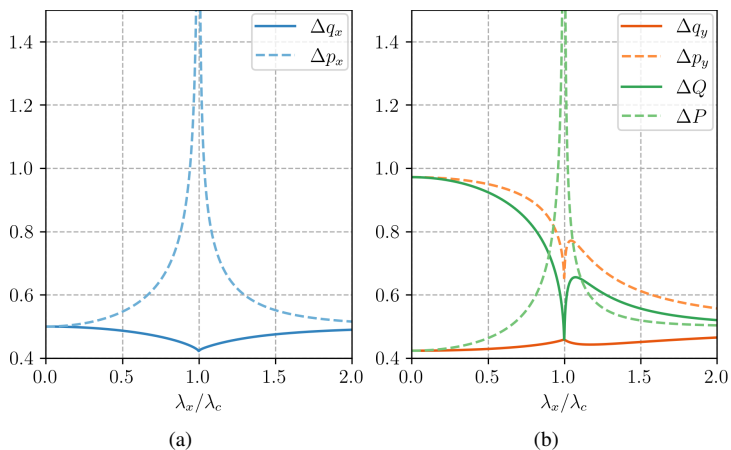
Figure 3.7: Variances for each configuration and momentum, corresponding to the diagonal elements in $\mathrm{cov}(\boldsymbol{R}_i, \boldsymbol{R}_j)$, at $\lambda_y = 0.9\lambda_c$ and $\omega = 1$.

diagonal counterpart: the ground state covariance matrix of a harmonic oscillator. This means that the equivalent treatment in this section, when starting from the input given by introducing the normal modes, leads to the relevant covariance matrix written as

$$C = \frac{(SS^{\mathsf{T}})^{-1}}{2}, \tag{3.94}$$

where S now is the matrix built from considerations of Williamson's theorem.

The diagonal elements of the covariance matrix are plotted in fig. 3.7 for each canonical coordinate. As the λ_x coupling vanishes the X degrees of freedom form a harmonic oscillator, whose ground state variance saturates the uncertainty principle as expected. After the critical point, in the deep-

strong coupling regime where $\lambda_x \gg \omega, \omega_0$ this saturation is again achieved; in fact, this strong coupling drives every degree of freedom to small uncertainty values as all variances approach $1/2$. The critical point occurs in the ultrastrong coupling regime, where $\lambda_x \approx \omega, \omega_0$. In this transition, the Y sector remains at finite uncertainty as the other bosonic mode and the collective lattice spins have their momentum variance divergent.

Subsystem parametrization. Given the covariance matrix of a state, the task of finding the corresponding covariance of subsystems is achieved by extracting the appropriate submatrix. We introduce the notation of partition subsets in typewriter font to refer to the three subsystems of interest: X for structures related to the algebra q_x, p_x; Y for the algebra q_y, p_y; and J for Q, P; in the matrix R notation, these symbols correspond to the indices $X = \{1, 2\}$, $Y = \{3, 4\}$ and $J = \{5, 6\}$. Phase space matrices indexed by these subsets, such as C_{XY} or $C_X = C_{XX}$, are meant to be corresponding block submatrices, whilst density operators refer to reduced states with the complementing subsystems traced out, for instance, $\varrho_X = \mathrm{tr}_{YJ}\, \varrho$.

The pure ground state ϱ, as well as its subsystems restricted to single degrees of freedom, are Gaussian state. The full system, being in an entangled state, yields mixed subsystems. A single-mode Gaussian covariance matrix has been fully parametrized in terms of the squeezing parameter and a mean quanta number, $\tilde{n}$, reflecting temperature or mixedness of the state; with $\tilde{n} = 0$ we are in the pure vacuum state, with no excitations, whilst $\tilde{n} \to \infty$ is a state of infinite temperature or maximum mixedness [143]. Let $C_{ij}^s = \mathrm{cov}(\boldsymbol{R}_i, \boldsymbol{R}_j)$, where s determines the range of indices (and hence
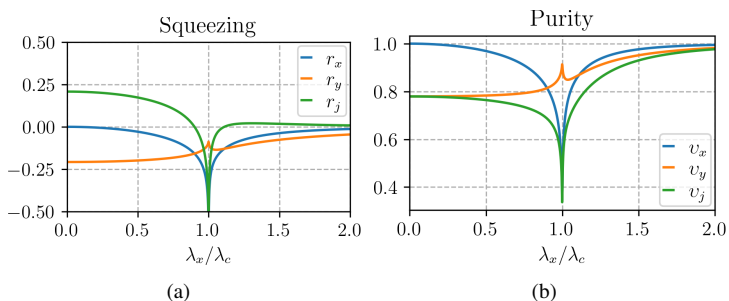
Figure 3.8: Squeezing parameter and purity of the respective one-mode reduced state at $\lambda_y = 0.9\lambda_c$ and $\omega = 1$. Positive r indicates squeezing in the configurations. With the relation (3.97) we see that the purity is a compactification (by inversion) to the unit interval of product of momentum and configuration variances in each subsystem, given that the covariance matrix is diagonal.

the subsystem), then

$$C^s = \left(\tilde{n}_s + \frac{1}{2}\right)\begin{pmatrix} e^{2r_s} & 0 \\ 0 & e^{-2r_s} \end{pmatrix}, \tag{3.95}$$

with r being a squeezing parameter. Equating this to each 2×2 block diagonals of the covariance matrix determines these variables as functions of λ_x and λ_y.

The squeezing parameter plotted in fig. 3.8a complements fig. 3.7 with information about the combined behavior of variances. Without the λ_x coupling the X system is a simple harmonic oscillator in its ground state, whilst the remaining non-zero coupling between Y and J indicates non-zero squeezing, defined as

$$r_s = \frac{1}{4}\ln\frac{C^s_{11}}{C^s_{22}}. \tag{3.96}$$

At the critical point $\lambda_x \to \lambda_c$ the X squeezing dips to arbitrary negative values, showing that momentum variance in that degree of freedom diverges and the configuration variance reaches a minimum. The other subsystems have somewhat opposing behavior near $\lambda_x = 0$, with Y reaching a local maximum at a cusp as $\infty > \Delta p_y > \Delta q_y$, and with J changing between net momentum to net configuration squeezing near λ_c. The crossing point is at $\lambda_x = \lambda_y (= 0.9$ in this case).

The ε parameter introduced in eq. (3.95) encodes mixedness in the subsystems. A better way to visualize its behavior, however, is to study the associated purity, defined as

$$v_s = \mathrm{tr}\, \varrho_s^2 = (\det 2C^s)^{-1/2}. \tag{3.97}$$

With the covariance matrix having the form eq. (3.95), we can make explicit v_s as a monotonically increasing function of ε_s:

$$v_s = \frac{1}{2\tilde{n} + 1}. \tag{3.98}$$

In fig. 3.8b we see that for $\lambda_x \to 0$ the purity v_x reaches its maximum. Since the X sector couples to the rest of the system through λ_x, in this limit the correlations between the parts vanish and the reduced state ϱ_X is pure, and hence uncorrelated to the other subsystems (as the full state is separable: $\varrho = \varrho_X \otimes \varrho_{YJ}$). This is suggested by the fact that $\tilde{n}_x \to \infty$ for vanishing λ_x, as it is monotonic with the inverse of temperature.

As λ_x approaches 0 for fixed λ_y these two subsystems remain coupled, leading to $v_y = v_j$ as the limit is reached. At this point, the X sector is independent, and the state is again separable. Since the bipartite state ϱ_{YJ} is pure and uncorrelated to ϱ_X, the entanglement entropy of its parts are equal

and therefore also the corresponding υ as both quantities depend solely on the symplectic eigenvalues of their corresponding reduced covariance matrix.

At λ_c all three subsystems reach a cusp, with both X and J at a minimum, and Y at a local maximum. In the superradiant regime all systems approach $\upsilon = 1$, with X and J doing so monotonically whilst Y first passes through a point of local minimum near λ_c.

Mutual information and entanglement. Aiming at ultimately computing tripartite entanglement measures, we introduce here the family of Rényi entropies. First, the general Rényi-α entropy is defined as[e]

$$S_\alpha(\rho) = \frac{1}{1-\alpha} \ln(\mathrm{tr}\,\rho^\alpha). \tag{3.99}$$

Similarly to how bipartite mutual information for the von Neumann entropy constructed, we can introduce the Rényi-α mutual information, that is, $\mathcal{I}_\alpha(A_i{:}A_j) = S_\alpha(A_i) + S_\alpha(b) - S_\alpha(A_iA_j)$.[f] Notice that in the case for the Rényi-2 entropy, this measure can be put in terms of purity υ:

$$S_2(\rho) = -\frac{1}{2} \ln[\upsilon(\rho)]. \tag{3.100}$$

The corresponding mutual information of a bipartition A_iA_j is, therefore,

$$\mathcal{I}_2(A_i{:}A_j) = -\ln\left(\frac{\upsilon_{A_i}\upsilon_{A_j}}{\upsilon_{A_iA_j}}\right). \tag{3.101}$$

For Gaussian states these measures have an expression in terms of the

---

[e]The von Neumann entropy is the limit Rényi-$(\alpha \to 1)$.

[f]We use partitions as argument for information-theoretic measures interchangeably with states as argument, when the latter is implied by context.

covariance matrix, stemming from the corresponding expression for purity, eq. (3.97). With $S_2(\rho) \mapsto S_2(C_\rho) = \ln(\det C_\rho)/2$, the mutual information is

$$\mathcal{I}_2(A_i{:}A_j) = \frac{1}{2} \ln\left(\frac{\det C_{A_i} \det C_{A_j}}{\det C_{A_i A_j}} \right). \tag{3.102}$$

Using the formulae we plot in fig. 3.9 the mutual information for two bipartitions, grouping the both field modes in subfigure (a), and one field mode plus the Holstein–Primakoff boson in subfigure (b). These figures and other conclusions in this section are reproduced from ref. [39].

For the first bipartition the density plot is symmetric by reflections through the diagonal, indicating the symmetric coupling of the field modes with the spin system. The diverging values across both phase transitions are similar in this case. In the second case, the singular behavior is distinguishable, being continuous at a cusp in the normal-to-superradiant transition, and only being divergent at decreasing λ_x across the Goldstone line.

To achieve a more thorough understanding on the correlation structure of the model, and to compare with the mutual information just computed, we also study entanglement. For pure states, particularly Gaussian ones, entanglement of two parties can be taken to mean the *entropy of entanglement*, which in terms of the Rényi-α entropy is $\mathcal{E}_\alpha(A_i{:}A_j) = S_\alpha(\text{tr}_{A_j} \rho)$.

For mixed states, which possibly also display other kinds of correlations, distinguishing entanglement from them is more difficult, and other measures exist to solve this task; they are, however, generally difficult to compute [143, 144]. We choose to work with the *entanglement of formation*, which for Gaussian states have an explicit analytical formula. Based on Rényi-2
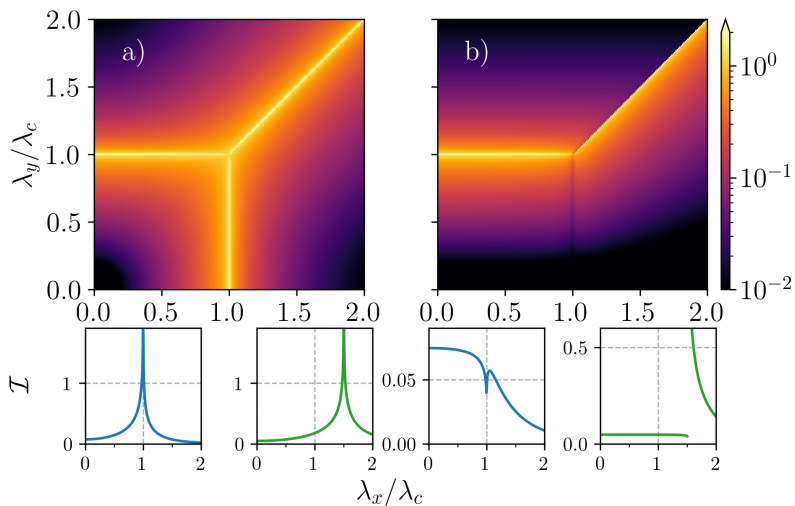
Figure 3.9: Phase diagram for Rényi-2 mutual information of bipartitions (a) $(XY{:}J)$ and (b) $(JX{:}Y)$, and accompanying slices at $\lambda_y = 0.5\lambda_c$ (left) and $\lambda_y = 1.5\lambda_c$ (right) below each density plot. Energy of field modes set at $\omega = 1$.

entropy, this measure is

$$\mathcal{E}_2(A_i{:}A_j) = \inf\left\{\frac{\ln(\det 2\Sigma_A)}{2} \mid 0 < \Sigma_{A_i A_j} \leq C_{A_i A_j}, \det \Sigma_{A_i A_j} = 1\right\}.$$
(3.103)

This is known as a convex roof construction, under which the pure state entanglement monotone $S_2(C_\rho)$ is extended to mixed states by minimizing over their decomposition into convex combination of pure states, Gaussian in the present case. From the construction above it is also evident that entanglement of formation is an upper bound to the entanglement of the system.

If $C_{A_i A_j}$ is itself a pure state, the entanglement measure $\mathcal{E}_2$ coincides, as expected, with entropy of entanglement:

$$\mathcal{E}_2(A_i{:}A_j) = S_2(C_{A_i}) = \frac{1}{2}\ln(\det 2C_{A_i}).$$
(3.104)

Since for a pure state $\det C_{AB} = 1$, implying that the Rényi-2 entropy vanishes and thereby that the entropy of the two subsystems are equal (from a singular value decomposition), there is no ambiguity in choosing with which party to compute $\mathcal{E}_2$. In this pure state case we also have that $\mathcal{I}_2(A_i{:}A_j) = 2S_2(C_A) = 2\mathcal{E}_2(A_i{:}A_j)$.

The measure eq. (3.103) is valid for any Gaussian state, including mixed ones. It simplifies for pure Gaussian states as described above, and the minimization can also be put in closed form for general two-mode Gaussian states, where the subsystems A and B each consist of a single mode. To

this end we must put the covariance matrix in its *standard form*:

$$
C =
\begin{pmatrix}
a_1 & 0 & c_3^+ & 0 & c_2^+ & 0 \\
0 & a_1 & 0 & c_3^- & 0 & c_2^- \\
c_3^+ & 0 & a_2 & 0 & c_1^+ & 0 \\
0 & c_3^- & 0 & a_2 & 0 & c_1^- \\
c_2^+ & 0 & c_1^+ & 0 & a_3 & 0 \\
0 & c_2^- & 0 & c_1^- & 0 & a_3
\end{pmatrix}.
\tag{3.105}
$$

In terms of C in the introduced standard form, the minimization in eq. (3.103) can be brought to the form

$$
\mathcal{E}_2(A_i{:}A_j) = \frac{1}{2} \ln g_k,
\tag{3.106}
$$

where

$$
g_k =
\begin{cases}
1, & \text{if } a_k \geq \sqrt{a_i^2 + a_j^2 - 1}; \\[2mm]
\dfrac{\beta}{8a_k^2}, & \text{if } \alpha_{ij} < a_k < \sqrt{a_i^2 + a_j^2 - 1}; \\[3mm]
\left(\dfrac{a_i^2 - a_j^2}{a_k^2 - 1}\right)^2, & \text{if } a_k \leq \alpha_{ij}
\end{cases}
,
\tag{3.107}
$$

and

$$\alpha_{ij} = \frac{1}{\sqrt{2(a_i^2 + a_j^2)}} \left(2(a_i^2 + a_j^2) + (a_i^2 - a_j^2)^2 \right.$$

$$\left. + |a_i^2 - a_j^2| \sqrt{(a_i^2 - a_j^2)^2 + 8(a_i^2 + a_j^2)} \right)^{\frac{1}{2}} \qquad (3.108a)$$

$$\beta = 2a_1^2 + 2a_2^2 + 2a_3^2 + 2a_1^2 a_2^2 + 2a_1^2 a_3^2 + 2a_2^2 a_3^2$$

$$- a_1^4 - a_2^4 - a_3^4 - \sqrt{\delta} - 1 \qquad (3.108b)$$

$$\delta = \prod_{\mu,\nu=0}^{1} \left[(a_1 + (-1)^\mu a_2 + (-1)^\nu a_3)^2 - 1 \right]. \qquad (3.108c)$$

With this general formula for bipartite entanglement, we can compare the generation of correlations in reduced parts of the system. With the symmetric coupling between the bosonic modes and the collective spin excitations with respect to parameters λ_x and λ_y, it suffices to check the partitions $(X{:}J)$ and $(X{:}Y)$. In fig. 3.10 we compare the measures of mutual information and entanglement with λ_y fixed, as a function of λ_y in both superradiant phases.

In fig. 3.10 we compare mutual information and bipartite entanglement in four instances. The left panes display these measures for the partition $(J{:}X)$. Notice how, for $\mathcal{I}_2$, this plot is similar to fig. 3.9(a), implying that the correlations of X and Y are small. Furthermore, the complete picture of bipartition $(XY{:}J)$ can be obtained by superposing the correlations of reduced systems; this is a consequence of the fact that, since the global state is pure, many of the measures simplify. For example, we have $\mathcal{I}_2(XY{:}J) = \mathcal{I}_2(Y{:}J) + \mathcal{I}_2(J{:}X)$.

For this choice still the entanglement measure in subfigure (c) is a
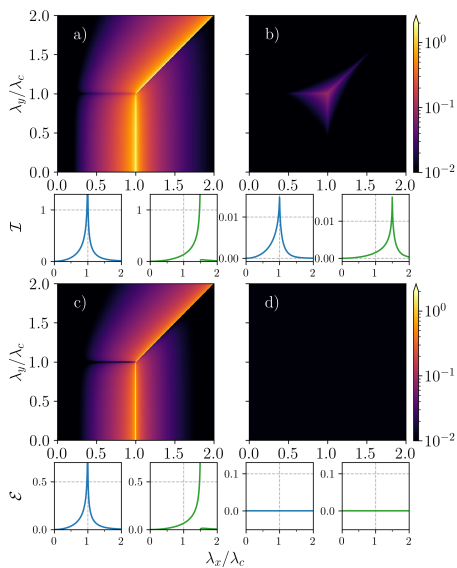
Figure 3.10: Density plots for (a) $\mathcal{I}_2(J{:}X)$ (b) $\mathcal{I}_2(X{:}Y)$ (c) $\mathcal{E}_2(J{:}X)$ (d) $\mathcal{E}_2(X{:}Y)$, at $\omega = 1$. Below each diagram there are slices at $\lambda_y = 0.5$ (left) and at $\lambda_y = 1.5$ (right).

suppressed version of the mutual information, which encompasses both quantum and classical correlations; entanglement, on the other hand, is a particular, although paradigmatic, example of quantum correlations.

In fig. 3.10(b) and fig. 3.10(d) the comparison is between measures with the choice of split $(Y{:}X)$. The mutual information in (a) is significantly weaker in comparison with its full system counterpart, confirming the expectations just mentioned above. Moreover, the corresponding bipartite entanglement of formation identically vanishes at all couplings, implying that the indirect interaction between field modes through their coupling with the collective spin excitations is insufficient to entangle them.

Among the commented results this is the strongest one. Entanglement measures are defined to be non-negative, so we have $\mathcal{E}_2 \geq 0$, but since entanglement of formation is an upper bound on entanglement, more definitive statements are limited. What we have shown, however, is that $\mathcal{E}_2 = 0$ for bipartition $(Y{:}X)$, thus saturating both constraints. We then conclude that in this partition, which refers to a mixed state (resulting from tracing out one of the subsystems), entanglement (not only entanglement of formation) is zero for all coupling values.

Tripartite entanglement. Beyond the difficulties present in distinguishing entanglement from other correlations for bipartitions in mixed states, the very network of entanglement of a multipartite system is in general difficult to resolve (see [145, §6.5]), even if the partition refers to a global pure state. For tripartite Gaussian systems this problem was reduced with the computation of analytical expressions also in terms of the entanglement of formation and Rényi-2 entropy; ref. [144] defines the *residual tripartite entanglement* as

$$\mathcal{E}_2(A_i;A_j{:}A_k) = \mathcal{E}_2(A_i{:}BC) - \mathcal{E}_2(A_i{:}A_j) - \mathcal{E}_2(A_i{:}A_k). \qquad (3.109)$$

The choice of subsystem is now unique, but the nature of eq. (3.109) introduces the freedom of what we call a *focus mode*: the single subsystem that appears in each of the entanglement arguments on the right-hand-side. This is a genuine measure of tripartite entanglement for Gaussian states, based on the property of monogamy of entanglement which, in terms of this quantity, is

$$\mathcal{E}_2(A_i;A_j{:}A_k) \geq 0. \qquad (3.110)$$

In terms of the standard form for the covariance matrix introduced
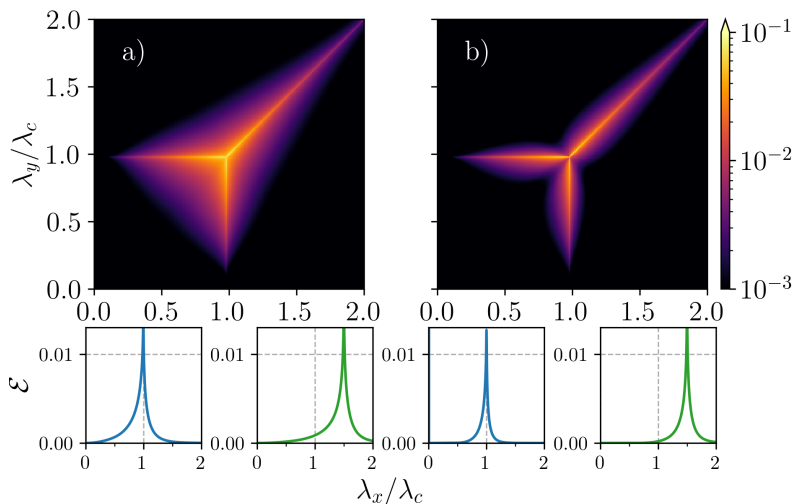
Figure 3.11: Tripartite entanglement.

above, the residual tripartite entanglement takes the form

$$\mathcal{E}_2(A_i;A_j:A_k) = \frac{1}{2}\ln\left(\frac{a_i^2}{g_jg_k}\right). \tag{3.111}$$

We can compute numerically $\mathcal{E}_2(A_i;A_j:A_k)$ with two choices of focus mode, X and J (the measure is symmetric in the other arguments) [39]. We can point out that this quantity becomes permutation invariant in all arguments for fully inseparable states, which is never our case, since $\mathcal{E}_2(X:Y) = 0$ in all parameter regions.

The choices made are shown in fig. 3.11. We show in these figures that, regardless of the choice of focus mode, tripartite entanglement is in general created, although it is significantly weaker when further away from

the critical lines, where the correlation lengths, on the other hand, becomes effectively infinite, hence consistently implying divergent entanglement. It is noticeable, too, that, contrary to bipartite entanglement, the three-party version seems to be insensitive to the order of the phase transition.

3.5   Summary of chapter

We have shown in this work that relevant and non-trivial properties of classical and quantum correlations present themselves in the equilibrium quantum phases of a Dicke model, extended to have two modes coupling with their own strengths to different components of the collective spin degrees of freedom [39].

   As expected from critical phenomena in many-body systems, where diverging correlation lengths emerge, we find that large classical and quantum correlations permeate the system near the regions of phase transition. One of these regions is where the coupling parameters are both equal and above their critical value, where we have shown that a broken continuous symmetry gives rise to a Goldstone bosonic mode.

   We verify that the systems exhibits tripartite entanglement, although it is significantly weak far from the critical points. Similar behavior is found for entanglement in the two collective spin-bosonic mode bipartitions. In contrast to this, bipartite entanglement among the two bosonic modes vanishes identically in every point of the phase diagram, rendering the states of the system separable in this partition.

   We approach the problem from a theoretical standpoint, inspired by the effective models introduced in refs. [131, 132] and others (see [126]). In this way, we hope to foment further studies of information-theoretic aspects of the model in an implementation-independent manner, applicable

to different platforms where the Dicke model interactions may be effectively simulated.

This work sets the stage for further research into developing a design for an autonomous absorption refrigerator. Typically, such a refrigerator uses a three-body interaction, in the shape of $a_c a_h^\dagger a_w + a_c^\dagger a_h a_w^\dagger$, for bosonic modes c, h and w, standing for cold, hot and work baths respectively. The work bath is the highest temperature bath of the three ($\beta_c > \beta_h > \beta_w$), and the interaction is engineered with resonant gaps $\omega_c + \omega_w = \omega_h$ in such a way that heat can only flow from the work bath to the hot bath by also taking quanta from the cold bath alongside it. This construction replaces the necessity of external control, thereby making it autonomous.

The three-body interaction is a necessary condition for the operation of the refrigerator, and the two-mode Dicke model has enough degrees of freedom to allow for that. This three-body interaction, however, marks a departure from our Gaussian treatment of the two-mode Dicke model, and would thus require further techniques. An additional point to note is that the critical point where the Goldstone mode appears is not robust and has been shown to vanish in a driven-dissipative model, which is avoided in the autonomous setting. The absorption refrigerator is thus an interesting setting within which we may study the interplay between thermodynamic protocols and novel phenomena taking place in quantum phases of matter.

Chapter 4

Conclusion

We investigated a diverse set of features of cooling in the heat-bath algorithmic cooling paradigm, ranging from its mechanisms based on computational aspects of the underlying microscopic quantum theory, to promising new phenomena that can fuel further research. With this we indent to help in making quantum refrigeration applicable in practice, and to help bridge the foundations of thermodynamics and its interplay with other theories.

In studying the particular implementation known as heat-bath algorithmic cooling, the task of refrigerating a quantum system was put to test in an experimental setting, where known cooling limits were shown by us to hold even in the presence of error models informed by laboratory settings [27, 36, 45]. We connected these studies to thermodynamic figures of merit, thus measuring algorithmic cooling up against typical thermal machines, establishing this design as a proper and efficient refrigerator with the capacity of achieving the fundamental Carnot bound of thermodynamics in the expected reversible regime.

By analyzing the experimental implementation in an NV center, we have identified two main effects in its performance: the presence of a stochastic activation, which slows down the rate at which the machine reaches a steady state and thus links to the cooling power measure for refrigerator, and amplitude losses, which lowers the cooling limit and thereby decreases the coefficient of performance of the machine. Full analytical solutions of the dynamical evolution were computed and are available in this thesis.

The problem of cooling a physical system can be put in very simple computational terms, which are an effective practical tool for small or simple system, being on of the principles underpinning heat-bath algorithmic cooling and making this thermodynamic task amenable and particularly inviting for quantum computing research. A second principle, that of virtual subsystems, then emerged during these studies and showed potential in applications. Known to be of more general value in quantum thermodynamics [50], and even quantum theory as a whole [101, 107], we sought to bring use of virtual qubits in improving cooling.

Virtual subsystems provide a powerful framework for cooling quantum systems [112], reducing it to a generalized swap operation between the target of refrigeration, and an environment virtual subsystem with the same dimension. Based on this idea we devised a method for boosting a qubit-cooling procedure by enabling the virtual subsystem to have quantum coherences that are transported to the target during the generalized swap of cooling, and which are ultimately used as resource to further polarize the system in the energy basis, driving it closer to the ground state as the purity of the state is maintained [38].

We then moved on to consider our protocol in a more realistic setting, testing its robustness against an experimental implementation. The central object was then not a target state whose coherence (of virtual qubit origin)

was exactly determined, but an ensemble of cooled qubits resulting from that first refrigeration step. Interestingly, we found that the boosting rotation was incredibly robust against uncertainties generated in the coherence values. By sharply identifying the coherence phase, the coherence amplitude could be as uncertain as logically possible, and yet the ensemble of target qubits would, on average, become colder. With improvements of up to 10% for smaller polarization values, we determined that this final coherence boost could be more advantageous than adding a larger number of reset qubits (thus accessing a cooler virtual qubit). This boost can be seen as a means to circumvent previously determined and fairly general cooling limits [47, 48].

A persisting goal of quantum thermodynamics is to test the limits of what thermal machines can do, and exploiting the use of genuine quantum features in their operation, not unlike the algorithmic advantages that have been found for quantum computers. We hope our protocol for use of quantum coherences that boost cooling beyond known limits adds in this endeavor. These efforts are not over, however, and aiming at finding novel quantum phenomena, and at the same time we extend our methods to the many-body regime, we investigated the equilibrium properties at zero temperature of a two-mode Dicke model.

The two-mode Dicke model has the proper degrees of freedom to accommodate a quantum absorption refrigerator. This cooler design works under the assumption of a three-body interaction, and accesses a particular set of virtual qubits of two heat baths, similarly to heat-bath algorithmic cooling [30]. We analyzed the system's parameter space of coupling constants at zero temperature, finding a duplicated region of quantum phase transition, from normal to superradiant phases in each bosonic mode, coupled to their respective collective spin degree-of-freedom [39].

In the thermodynamic limit of many qubits, the Dicke model behaves as

a mean-field theory, and the spin degrees-of-freedom mix with the bosonic modes into three new bosonic ones. We found the Gaussian bosonic ground state and used this to evaluate and build a correlation profile of that state. We find robust regions of bipartite entanglement between all bipartition combinations (spin and bosonic mode, as well as boson-boson). Moreover, we find that near the critical lines of phase transition, genuine tripartite entanglement grow, in accordance with general expectations of phase transitions where the correlation length diverges and the system achieves a highly-correlated state.

These efforts rely on a driven-dissipative version of the model, where the system is left open and thus stays in a non-equilibrium state, to tune and monitor parameters relevant to establish the results here discussed. A natural but important next step of the present investigation is therefore to consider the inclusion of these open-systems aspects and the refrigeration dynamical protocol, and how the phase diagram reacts to that. Recent research has been carried out in this direction for distinct extensions of the Dicke model, such as in refs. [133, 146–149].

This work comes in a wave of recent theoretical and experimental achievements in recent years that push towards finer control of quantum systems, with varying goals, ranging from technological interests in information processing and quantum-thermodynamic engineering, to setups aiming at testing fundamental physics. By advancing our understanding of the non-equilibrium aspects of the two-mode Dicke model as laid out above, we are able to aid directly these novel achievements. In this setup, thermodynamic features of the model are made front and centre, and can be exploited to study foundations of thermodynamics of quantum systems and to build thermal machines operating non-classicaly.

Appendix A

Vectorization

The natural representation of quantum maps. We introduce the vectorization transformations that map density matrices into column matrices and quantum channels into matrix operators, acting on the columns [89, 90, 92, 150, 151]. To set the notation, we define vectorization on states as

$$\text{vec} \colon \rho \mapsto \vec{\rho} = \text{vec}(\rho). \tag{A.1}$$

In the qubit case, the central Hilbert space from which the quantum dynamics are constructed is $\mathbf{H} = \mathbb{C}^2$. Thus, the density matrix of a state is represented an element of $\mathbb{M}_{\mathbb{C}}^{2 \times 2}$: 2-by-2 matrices with complex entries; in particular, they are Hermitian and positive semidefinite. In terms of its elements, a density matrix is mapped by vec by stacking its columns into a single one,

such as in

$$\frac{1}{2} \begin{pmatrix} 1+z & x+\mathrm{i}y \\ x-\mathrm{i}y & 1-z \end{pmatrix} \xrightarrow{\text{vec}} \frac{1}{2} \begin{pmatrix} 1+z \\ x-\mathrm{i}y \\ x+\mathrm{i}y \\ 1-z \end{pmatrix}, \tag{A.2}$$

where $\mathbb{M}_{\mathbb{C}}^{2\times 2} \overset{\text{vec}}{\cong} \mathbb{M}_{\mathbb{C}}^{1\times 4} = \mathbb{C}^4$. We call the resulting column matrix space Liouville space. For a vector in this space to represent a state, it must obey certain conditions. These conditions, however, are more naturally stated in the unvectorized form, as we have listed above. More generally, for a d-dimensional system, vectorization reads

$$\begin{aligned} \rho = \sum_{i=0}^{d-1} \sum_{j=0}^{d-1} \rho_{ij} \left|i\right\rangle\!\left\langle j\right| \xrightarrow{\text{vec}} \vec{\rho} &= \sum_{i,j} \rho_{ij} \left|i\right\rangle\!\left|j\right\rangle \\ &= \sum_{k=0}^{d^2-1} \rho_k \left|k\right\rangle, \end{aligned} \tag{A.3}$$

where in the bottom line of the right-hand side, k goes over the d^2 joint indices ij in anti-lexicographic order, corresponding to the choice of stacking columns. For instance, for $d = 2$,

$$\begin{aligned} ij\colon\ & 00 \to 01 \to 10 \to 11 \\ k\colon\ & 0\ \to\ 1\ \to\ 2\ \to\ 3\,, \end{aligned} \tag{A.4}$$

such as the case of a one-qubit density matrix. Note that each index here refers to rows and columns, not to two qubits.

The vectorization of states induces a second mapping, also known as the natural representation of quantum maps Φ [90]. Quantum maps defined on a state by its operator-sum representation, $\mathcal{E}[\rho] = \sum_\mu E_\mu \rho E_\mu^\dagger$, will obey

the compatibility condition:

$$\Phi_{\mathcal{E}} \vec{\rho} = \text{vec}[\mathcal{E}(\rho)]. \tag{A.5}$$

In words, the compatibility condition is the statement that there exists $\Phi_{\mathcal{K}}$ such that it maps the vectorized input state to the vectorization of the output of $\mathcal{K}$. With the quantum map $\mathcal{E}$ being the action of a semigroup, the vectorization map is known as an intertwiner. The solution to the compatibility condition in these variables is

$$\Phi_{\mathcal{E}} = \sum_{\mu} E_{\mu} \otimes (E_{\mu}^{\dagger})^{\intercal}, \tag{A.6}$$

where the combined adjoints $(E_{\mu}^{\dagger})^{\intercal}$ culminate in simple complex conjugation, E_{μ}^{*} in finite dimensions. As such, a map $\Phi_{\mathcal{E}}$ on a qubit is a matrix element of $\mathbb{M}_{\mathbb{C}}^{4 \times 4}$ that allows rewriting the operator sum representation of $\mathcal{K}$ as simple matrix multiplication. For this reason the natural representation is chosen for most of the practical calculations in this thesis. In forgoing the usual conjugation action of unitaries or the operator-sum representation in favor of regular matrix multiplication, the computations more simply implemented in computer algebra systems, such as Mathematica.

Another advantage of this representation is that quantum channels are unique, which is not true in the operator-sum representation: there are possibly more than one set of Kraus operators E_{μ} that implement the same channel. In contrast, the vectorized representation is not ideal to infer quantum properties of the channel of interest [90]. A third representation that is more suited for this is the Choi representation, where the map is also unique and where the property of being completely positive translates to its Choi representation being positive semidefininte. In fact, the non-

uniqueness of Kraus operators in turn translates to the non-uniqueness in writing the Choi representation as a sum of dyadics. The Kraus operators are the unvectorization of the vectors defining these dyadics.

Appendix B

NV center experimental details

This section provides additional details about the experimental implementation of the three-qubit heat-bath algorithmic cooling refrigerator using a system of a NV center in diamond [27] in direct correspondence to ref. [36], on which chapter 1 is based.

The experimental setup consists of a confocal microscope, a permanent magnet for the creation of the external magnetic field and equipment for electron and nuclear spin manipulation as shown in fig. B.1. The setup operates at room temperature and atmospheric pressure and is used exclusively to work with single NV centers. The diamond sample is embedded into a sapphire waver of $2\mathrm{mm}$ thickness and a diameter of $50\mathrm{mm}$. The sapphire waver is mounted on a 3-axis piezoelectric scanner with a travel range of $100\mu\mathrm{m} \times 100\mu\mathrm{m} \times 25\mu\mathrm{m}$ and subnanometer resolution.
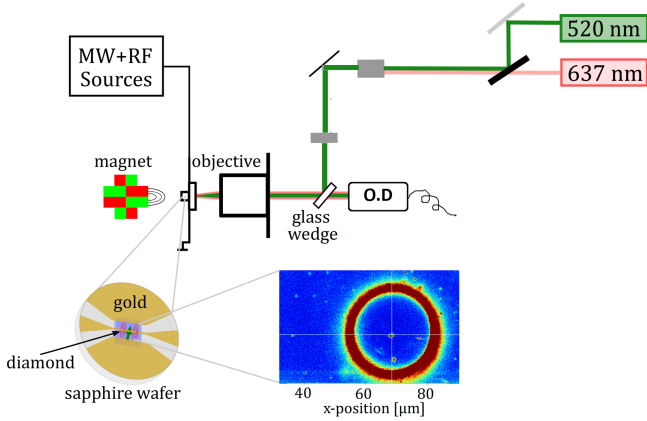
Figure B.1: Sketch of the experimental setup. The setup consists of a homebuilt confocal microscope, a permanent magnet and microwave (MW) and radio frequency (RF) sources. The 520nm laser is operated at a power close to NV center saturation (0.1mW to 0.5mW before the objective). An additional 637nm laser is used for electron spin repolarization (charge state control) and thus has a power of less than 10µW. O.D. is the standard optical detection setup where the fluorescence is filtered by a 650nm long-pass filter and a 50µm pinhole, and then detected by a single-photon-counting avalanche photodiode. At the bottom are shown the sample, substrate and the confocal image displaying the location of the NV center.

Reset polarization. The SWAP gate used for the reset steps is adapted for the efficient generation of a variable degree of nuclear spin polarization. As compared to the implementation of the traditional SWAP gate using three CNOT gates, here only two CNOT gates are enough. The final electron spin state after application of the SWAP gate is indeed irrelevant, as it only acts as source of polarization and can be easily repolarized with a green or red laser pulse into $|m_s = 0\rangle$. Therefore, the third controlled rotation is not required, and the SWAP gate simplifies to two controlled spin rotations. Furthermore, to achieve variable polarization transfer to the nuclear spins,

Figure B.2: Pulse sequence for variable degree polarization transfer from electron spin to the two nuclear spins used in the experiment. The electron initially is in state $|m_s = 0\rangle$, while the target ^{13}C nuclear spin is in a fully mixed state. To remove any remaining polarization, before the polarization step, a 50µs long $\pi/2$-pulse is performed on the nuclear spin. The actual polarization transfer part of the sequence consists of a 80µs red laser pulse for electron reset, a nuclear spin controlled electron π-pulse (6µs/20µs for ^{13}C$_1$/^{13}C$_2$) and an electron spin controlled nuclear spin rotation of variable duration (0µs to 100µs). To increase the nuclear spin polarization, the polarization transfer part can be repeated n-times. Finally, the spin state is read out with single-shot readout (SSR). The experiment was performed for angles θ between 0 and 2π.

the second electron controlled nuclear rotation does not necessarily need to cover the full angle $\theta = \pi$ but can be replaced by a rotation of variable angle, $R_{y,\theta}$ as shown in fig. B.1.

For the choice of the magnetic field (540mT) used in the experiment, direct optical nuclear spin polarization due to GSLAC and ESLAC is not possible as it requires much lower fields ($\sim$50 to 100mT). The choice for such large fields is to achieve high fidelity single shot readout of the nuclear spins, by improving the nuclear spin life-time that scales quadratically with the field strength [152]. The ^{14}N nuclear spin lifetime reaches close to a millisecond at such field strengths.

Gate implementation.   The total gate duration of cooling operation U is $\sim$284µs. An optimal pulse-duration for the nuclear spin gates was chosen

to be around 50μs to omit heating of the sample due to the large RF power and to omit crosstalk to other nuclear spin transitions. The electron spin controlled nuclear spin phase gates do not change the state of the electron spin, thereby avoiding any decoupling errors during the gate operation. Furthermore, the electron spin state remaining in state $|m_s = 0\rangle$ during the long nuclear spin operations will preserve its coherence over the electron spin relaxation timescales of $T_{1,e} \sim 5.7$ms. The electron spin 2π-pulses take at total duration of 84µs [27]. While the coherences decay on a timescale of $T_{2,e}^{\text{Hahn}} \sim 395$µs. The electron spin gates were optimized with help of the optimal control platform DYNAMO [153] to realize fast and robust Hahn gates despite electron decoherence on timescales of $T_{2,e}^{\text{Hahn}}$ and a dense electron spin spectrum [154].

Appendix C

Williamson's theorem

We develop here an adapted version of the arguments leading to the expression of S in section 3.3.1 as shown in [142, §3.2.3].

Williamson's theorem.   Let K be a symmetric positive-definite matrix. There exists a real symplectic matrix S such that

$$SKS^\mathsf{T} = V, \tag{C.1}$$

where V is a diagonal matrix with positive components.

An algorithm for symplectic diagonalization.   Williamson's theorem provides an algorithm to construct the linear symplectic transformation that puts these operators in their normal mode form. Their ground state is thereby found to be the tensor product of vacuum states of each of the normal modes under the inverse transformation.

The theorem states that a positive-definite symmetric $2N \times 2N$ matrix K can be put in diagonal form $V = \text{diag}(\nu_1, \nu_1, \ldots, \nu_N, \nu_N)$, where $\nu_i \geqslant 0$ are the symplectic eigenvalues, through a symplectic matrix M:

$$K = MVM^\mathsf{T}. \tag{C.2}$$

A proof of this theorem yields the algorithm to construct M; we follow Appendix A of [155] to show this below.

We first note that the symplectic eigenvalues defining V can be computed through regular diagonalization with unitary matrices. Consider the matrix $\widetilde{K} = iK^{1/2}\Omega K^{1/2}$, where Ω is the symplectic form. $\widetilde{K}$ is a Hermitian matrix, thus having real eigenvalues.[a] It remains to show how the spectrum and eigenvectors of $\widetilde{K}$ is related to relation (C.2), and this is done by constructing M.

The eigenvalues of $\widetilde{K}$ are split into pairs, $\widetilde{K}u_i = \nu_i u_i$ and $\widetilde{K}u_i^* = -\nu_i u_i^*$. Let U be the unitary matrix diagonalizing $\widetilde{K}$:

$$\widetilde{K} = U \begin{pmatrix} \nu_1 & & & & \\ & -\nu_1 & & & \\ & & \ddots & & \\ & & & \nu_N & \\ & & & & -\nu_N \end{pmatrix} U^\dagger. \tag{C.3}$$

---

[a]An alternative is to find the spectrum of $i\Omega K$, which through a similarity transformation is shown to share the same eigenvalues as $\widetilde{K}$: $K^{-1/2}\widetilde{K}K^{1/2} = i\Omega K$.

Composing U with

$$W = \begin{pmatrix} w & 0 & 0 \\ 0 & \ddots & 0 \\ 0 & 0 & w \end{pmatrix}, \quad \text{where } w = \frac{1}{\sqrt{2}} \begin{pmatrix} 1 & i \\ 1 & -i \end{pmatrix}, \tag{C.4}$$

allows us to find

$$M = K^{1/2} U W \left(\bigoplus_{i=1}^{N} \begin{pmatrix} \nu_i^{-1/2} & 0 \\ 0 & \nu_i^{-1/2} \end{pmatrix} \right), \tag{C.5}$$

which can be shown to be symplectic.

Finally, by inverting the relation (C.2) as $M^{-1} K (M^{-1})^{\mathsf{T}}$, we arrive at

$$V = \begin{pmatrix} \nu_1 & & & & \\ & \nu_1 & & & \\ & & \ddots & & \\ & & & \nu_N & \\ & & & & \nu_N \end{pmatrix}. \tag{C.6}$$

In steps, an algorithm to find the symplectic spectrum of K, namely find V and M, is: 1) Diagonalize $\widetilde{K}$, i.e. find its eigenvalues (seen in (C.3)) and eigenvectors U. 2) Write down M as in (C.5), with W also given above. 3) Write down V as in eq. (C.6), where the diagonal values are pairwise the absolute values of the spectrum of $\widetilde{K}$.

Bibliography

[1] D. P. DiVincenzo and IBM, "The Physical Implementation of Quantum Computation," Fortschr. Phys. **48**, 771–783 (2000).

[2] L. Buffoni, S. Gherardini, E. Z. Cruzeiro, and Y. Omar, "Third law of thermodynamics and the scaling of quantum computers," Phys. Rev. Lett. **129**, 150602 (2022).

[3] J. Preskill, "The Physics of Quantum Information," (2022), 10.48550/arXiv.2208.08064.

[4] D. A. Lidar and K. B. Whaley, "Decoherence-Free Subspaces and Subsystems," (2003), 10.48550/arXiv.quant-ph/0301032.

[5] P. Cappellaro, J. S. Hodges, T. F. Havel, and D. G. Cory, "Control of qubits encoded in decoherence-free subspaces," Laser Phys. **17**, 545–551 (2007).

[6] L.-A. Wu, P. Zanardi, and D. A. Lidar, "Holonomic quantum computation in decoherence-free subspaces," Phys. Rev. Lett. **95**, 130501 (2005).

[7] J. B. Altepeter, P. G. Hadley, S. M. Wendelken, A. J. Berglund, and P. G. Kwiat, "Experimental Investigation of a Two-Qubit Decoherence-Free Subspace," Phys. Rev. Lett. **92**, 147901 (2004).

[8] E. M. Fortunato, L. Viola, M. A. Pravia, E. Knill, R. Laflamme, T. F. Havel, and D. G. Cory, "Exploring Noiseless Subsystems via Nuclear Magnetic Resonance," Phys. Rev. A **67**, 062303 (2003).

[9] M.-D. Choi and D. W. Kribs, "A method to find quantum noiseless subsystems," Phys. Rev. Lett. **96**, 050501 (2006).

[10] P. Zanardi and S. Lloyd, "Topological Protection and Quantum Noiseless Subsystems," Phys. Rev. Lett. **90**, 067902 (2003).

[11] E. Knill, R. Laflamme, and L. Viola, "Theory of Quantum Error Correction for General Noise," (1999), 10.48550/arXiv.quant-ph/9908066.

[12] E. Knill and R. Laflamme, "A Theory of Quantum Error-Correcting Codes," Phys. Rev. Lett. **84**, 2525–2528 (2000).

[13] C. E. Wieman, D. E. Pritchard, and D. J. Wineland, "Atom cooling, trapping, and quantum manipulation," Rev. Mod. Phys. **71**, S253–S262 (1999).

[14] J. I. Cirac and P. Zoller, "Quantum Computations with Cold Trapped Ions," Phys. Rev. Lett. **74**, 4091–4094 (1995).

[15] C. Monroe, D. M. Meekhof, B. E. King, W. M. Itano, and D. J. Wineland, "Demonstration of a Fundamental Quantum Logic Gate," Phys. Rev. Lett. **75**, 4714–4717 (1995).

[16] M. Popp, J. J. Garcia-Ripoll, K. G. H. Vollbrecht, and J. I. Cirac, "Ground state cooling of atoms in optical lattices," Phys. Rev. A **74**, 013622 (2006).

[17] E. Zohar, J. I. Cirac, and B. Reznik, "Quantum simulations of lattice gauge theories using ultracold atoms in optical lattices," Reports Prog. Phys. **79**, 014401 (2016).

[18] D. Jaksch, C. Bruder, J. I. Cirac, C. W. Gardiner, and P. Zoller, "Cold bosonic atoms in optical lattices," Phys. Rev. Lett. **81**, 3108–3111 (1998).

[19] M. Greiner, O. Mandel, T. Esslinger, T. W. Hänsch, and I. Bloch, "Quantum phase transition from a superfluid to a Mott insulator in a gas of ultracold atoms," Nature **415**, 39–44 (2002).

[20] D. G. Cory, A. F. Fahmy, and T. F. Havel, "Ensemble quantum computing by NMR spectroscopy," Proceedings of the National Academy of Sciences **94**, 1634–1639 (1997).

[21] N. A. Gershenfeld and I. L. Chuang, "Bulk Spin-Resonance Quantum Computation," Science **275**, 350–356 (1997).

[22] L. J. Schulman and U. V. Vazirani, "Molecular scale heat engines and scalable quantum computation," in *Proceedings of the Thirty-First Annual ACM Symposium on Theory of Computing - STOC '99* (ACM Press, Atlanta, Georgia, United States, 1999) pp. 322–329.

[23] D. E. Chang, L. M. K. Vandersypen, and M. Steffen, "NMR implementation of a building block for scalable quantum computation," Chemical Physics Letters **338**, 337–344 (2001).

[24] P. O. Boykin, T. Mor, V. Roychowdhury, F. Vatan, and R. Vrijen, "Algorithmic cooling and scalable NMR quantum computers," Proc. Natl. Acad. Sci. U.S.A. **99**, 3388–3393 (2002).

[25] L. J. Schulman, T. Mor, and Y. Weinstein, "Physical Limits of Heat-Bath Algorithmic Cooling," Phys. Rev. Lett. **94**, 120501 (2005).

[26] C. A. Ryan, O. Moussa, J. Baugh, and R. Laflamme, "A spin based heat engine: Demonstration of multiple rounds of algorithmic cooling," Phys. Rev. Lett. **100**, 140501 (2008).

[27] S. Zaiser, C. T. Cheung, S. Yang, D. B. R. Dasari, S. Raeisi, and J. Wrachtrup, "Cyclic cooling of quantum systems at the saturation limit," npj Quantum Inf. **7**, 92 (2021).

[28] G. Maslennikov, S. Ding, R. Hablützel, J. Gan, A. Roulet, S. Nimmrichter, J. Dai, V. Scarani, and D. Matsukevich, "Quantum absorption refrigerator with trapped ions," Nat. Commun. **10**, 202 (2019).

[29] M. A. Aamir, P. J. Suria, J. A. M. Guzmán, C. Castillo-Moreno, J. M. Epstein, N. Y. Halpern, and S. Gasparinetti, "Thermally driven quantum refrigerator autonomously resets superconducting qubit," (2023), 10.48550/arXiv.2305.16710.

[30] M. T. Mitchison, "Quantum thermal absorption machines: Refrigerators, engines and clocks," Contemporary Physics **60**, 164–187 (2019).

[31] R. Kosloff and A. Levy, "Quantum heat engines and refrigerators: Continuous devices," Annu. Rev. Phys. Chem. **65**, 365–393 (2014).

[32] E. Albert and S. Leo, "Refrigeration," (1930).

[33] H. E. D. Scovil and E. O. Schulz-DuBois, "Three-Level Masers as Heat Engines," Phys. Rev. Lett. **2**, 262–263 (1959).

[34] J. E. Geusic, E. O. Schulz-DuBios, and H. E. D. Scovil, "Quantum Equivalent of the Carnot Cycle," Phys. Rev. **156**, 343–351 (1967).

[35] J. P. Palao, R. Kosloff, and J. M. Gordon, "Quantum thermodynamic cooling cycle," Phys. Rev. E **64**, 056130 (2001).

[36] R. Soldati, D. B. R. Dasari, J. Wrachtrup, and E. Lutz, "Thermodynamics of a minimal algorithmic cooling refrigerator," Phys. Rev. Lett. **129**, 030601 (2022).

[37] F. Rempp, M. Michel, and G. Mahler, "Cyclic cooling algorithm," Phys. Rev. A **76**, 032325 (2007).

[38] R. R. Soldati, D. B. R. Dasari, J. Wrachtrup, and E. Lutz, "Cooling advantage of coherent virtual qubits," (2023), Manuscript under review.

[39] R. Soldati, M. T. Mitchison, and G. T. Landi, "Multipartite quantum correlations in a two-mode Dicke model," Physical Review A **104**, 052423 (2021).

[40] R. H. Dicke, "Coherence in Spontaneous Radiation Processes," Phys. Rev. **93**, 99–110 (1954).

[41] K. Baumann, C. Guerlin, F. Brennecke, and T. Esslinger, "Dicke quantum phase transition with a superfluid gas in an optical cavity," Nature **464**, 1301–1306 (2010).

[42] P. Kirton, M. M. Roses, J. Keeling, and E. G. D. Torre, "Introduction to the Dicke model: From equilibrium to nonequilibrium, and vice versa," Adv. Quantum Technol. **2**, 1800043 (2018).

[43] D. K. Park, N. A. Rodriguez-Briones, G. Feng, R. R. Darabad, J. Baugh, and R. Laflamme, "Heat Bath Algorithmic Cooling with Spins: Review and Prospects," (2015).

[44] N. A. Rodriguez-Briones, J. Li, X. Peng, T. Mor, Y. Weinstein, and R. Laflamme, "Heat-Bath Algorithmic Cooling with correlated qubit-environment interactions," New J. Phys. **19** (2017), 10.1088/1367-2630/aa8fe0.

[45] N. A. Rodríguez-Briones and R. Laflamme, "Achievable Polarization for Heat-Bath Algorithmic Cooling," Phys. Rev. Lett. **116**, 170501 (2016).

[46] P. Taranto, F. Bakhshinezhad, P. Schüttelkopf, F. Clivaz, and M. Huber, "Exponential improvement for quantum cooling through finite-memory effects," Phys. Rev. Applied **14**, 054005 (2020).

[47] F. Clivaz, R. Silva, G. Haack, J. B. Brask, N. Brunner, and M. Huber, "Unifying paradigms of quantum refrigeration: A universal and attainable bound on cooling," Phys. Rev. Lett. **123**, 1–6 (2019).

[48] F. Clivaz, R. Silva, G. Haack, J. B. Brask, N. Brunner, and M. Huber, "Unifying paradigms of quantum refrigeration: Fundamental limits of cooling and associated work costs," Phys. Rev. E **100**, 042130 (2019).

[49] N. A. Rodríguez-Briones, E. Martín-Martínez, A. Kempf, and R. Laflamme, "Correlation-Enhanced Algorithmic Cooling," Phys. Rev. Lett. **119**, 050502 (2017).

[50] N. Brunner, N. Linden, S. Popescu, and P. Skrzypczyk, "Virtual qubits, virtual temperatures, and the foundations of thermodynamics," Phys. Rev. E **85**, 051117 (2012).

[51] M. Baldovin, S. Iubini, R. Livi, and A. Vulpiani, "Statistical Mechanics of Systems with Negative Temperature," Physics Reports **923**, 1–50 (2021).

[52] A. Riera-Campeny, A. Sanpera, and P. Strasberg, "Quantum systems correlated with a finite bath: Nonequilibrium dynamics and thermodynamics," PRX Quantum **2**, 010340 (2021).

[53] G. T. Landi and M. Paternostro, "Irreversible entropy production: From classical to quantum," Rev. Mod. Phys. **93**, 035008 (2021).

[54] M. Campisi, J. Pekola, and R. Fazio, "Nonequilibrium fluctuations in quantum heat engines: Theory, example, and possible solid state experiments," New J. Phys. **17**, 035012 (2015).

[55] A. E. Allahverdyan, K. Hovhannisyan, and G. Mahler, "Optimal refrigerator," Phys. Rev. E **81**, 051129 (2010).

[56] O. A. D. Molitor and G. T. Landi, "Stroboscopic two-stroke quantum heat engines," Phys. Rev. A **102**, 042217 (2020).

[57] J. Baugh, O. Moussa, C. A. Ryan, A. Nayak, and R. Laflamme, "Experimental implementation of heat-bath algorithmic cooling using solid-state nuclear magnetic resonance," Nature **438**, 470–473 (2005).

[58] M. Popp, K. Vollbrecht, and J. Cirac, "Ensemble quantum computation and algorithmic cooling in optical lattices," Fortschr. Phys. **54**, 686–701 (2006).

[59] W. S. Bakr, P. M. Preiss, M. E. Tai, R. Ma, J. Simon, and M. Greiner, "Orbital excitation blockade and algorithmic cooling in quantum gases," Nature **480**, 500–503 (2011).

[60] S. Raeisi and M. Mosca, "Asymptotic Bound for Heat-Bath Algorithmic Cooling," Phys. Rev. Lett. **114**, 100404 (2015).

[61] S. Raeisi, M. Kieferová, and M. Mosca, "Novel Technique for Robust Optimal Algorithmic Cooling," Phys. Rev. Lett. **122**, 220501 (2019).

[62] Á. M. Alhambra, M. Lostaglio, and C. Perry, "Heat-Bath Algorithmic Cooling with optimal thermalization strategies," Quantum **3**, 188 (2019).

[63] F. Clivaz, *Optimal Manipulation Of Correlations And Temperature In Quantum Thermodynamics*, Ph.D. thesis, Université de Genève (2020).

[64] R. Laflamme, J. Lin, and T. Mor, "Algorithmic cooling for resolving state preparation and measurement errors in quantum computing," Phys. Rev. A **106**, 012439 (2022).

[65] K. Shende, Arvind, and K. Dorai, "State-independent robust heat-bath algorithmic cooling of nuclear spins," (2023), 10.48550/arXiv.2303.09087.

[66] H. B. Callen, *Thermodynamics and an Introduction to Thermostatistics* (Wiley, New York, 1985).

[67] H. J. Metcalf and P. van der Straten, *Laser Cooling and Trapping* (Springer, Berlin, 1999).

[68] V. S. Letokhov, *Laser Control of Atoms and Molecules* (Oxford University Press, Oxford, 2007).

[69] P. V. E. McClintock, D. J. Meredit, and J. K. Wigmore, *Low-Temperature Physics* (Springer, Berlin, 1992).

[70] C. Ens and S. Hunklinger, *Low-Temperature Physics* (Springer, Berlin, 2005).

[71] M. A. Nielsen and I. L. Chuang, *Quantum Computation and Quantum Information: 10th Anniversary Edition*, 1st ed. (Cambridge University Press, 2012).

[72] E. Desurvire, *Classical and Quantum Information Theory* (Cambridge University Press, Cambridge, 2009).

[73] J. M. Fernandez, S. Lloyd, T. Mor, and V. Roychowdhury, "Algorithmic cooling of spins: A practicable method for increasing polarization," International Journal of Quantum Information **2**, 461 (2004).

[74] L. J. Schulman, T. Mor, and Y. Weinstein, "Physical Limits of Heat-Bath Algorithmic Cooling," SIAM J. Comput. **36**, 1729–1747 (2007).

[75] P. Kaye, "Cooling algorithms based on the 3-Bit majority," Quantum Information Processing **6**, 295 (2007).

[76] G. Brassard, Y. Elias, T. Mor, and Y. Weinstein, "Prospects and limitations of algorithmic cooling," Eur. Phys. J. Plus **129**, 258 (2014).

[77] S. Raeisi, "No-go theorem behind the limit of the heat-bath algorithmic cooling," Phys. Rev. A **103**, 062424 (2021).

[78] D. K. Park, G. Feng, R. Rahimi, S. Labruyere, T. Shibata, S. Nakazawa, K. Sato, T. Takui, R. Laflamme, and J. Baugh, "Hyperfine spin qubits in irradiated malonic acid: Heat-bath algorithmic cooling," Quantum Information Processing **14**, 2435 (2015).

[79] Y. Atia, Y. Elias, T. Mor, and Y. Weinstein, "Algorithmic cooling in liquid-state nuclear magnetic resonance," Phys. Rev. A **93**, 012325 (2016).

[80] Y. Rezek, P. Salamon, K. H. Hoffmann, and R. Kosloff, "The quantum refrigerator: The quest for absolute zero," Europhys. Lett. **85**, 30008 (2009).

[81] O. Abah and E. Lutz, "Optimal performance of a quantum Otto refrigerator," Europhys. Lett. **113**, 60002 (2016).

[82] P. Liuzzo-Scorpo, L. A. Correa, R. Schmidt, and G. Adesso, "Thermodynamics of quantum feedback cooling," Entropy **18**, 48 (2016).

[83] M. J. Ondrechen, B. Andresen, M. Mozurkewich, and R. S. Berry, "Maximum work from a finite reservoir by sequential Carnot cycles," Am. J. Phys. **49**, 681 (1981).

[84] Y. Wang, "Optimizing work output for finite-sized heat reservoirs: Beyond linear response," Phys. Rev. E **93**, 012120 (2016).

[85] H. Tajima and M. Hayashi, "Finite-size effect on optimal efficiency of heat engines," Phys. Rev. E **96**, 012128 (2017).

[86] A. Pozas-Kerstjens, E. G. Brown, and A. K. V. Hovhannisyan, "Quantum Otto engine with finite heat baths: Energy, correlations, and degradation," New Journal of Physics **20**, 043034 (2018).

[87] M. H. Mohammady and A. Romito, "Efficiency of a cyclic quantum heat engine with finite-size baths," Phys. Rev. E **100**, 012122 (2019).

[88] Y. H. Ma, "Effect of finite-size heat source's heat capacity on the efficiency of heat engine," Entropy **22**, 1002 (2020).

[89] J. A. Gyamfi, "Fundamentals of Quantum Mechanics in Liouville Space," Eur. J. Phys. **41**, 063002 (2020).

[90] J. Watrous, *The Theory of Quantum Information*, 1st ed. (Cambridge University Press, 2018).

[91] M. W. Doherty, N. B. Manson, P. Delaney, F. Jelezko, J. Wrachtrup, and L. C. L. Hollenberg, "The nitrogen-vacancy colour centre in diamond," Physics Reports **528**, 1–45 (2013).

[92] A. Gilchrist, D. R. Terno, and C. J. Wood, "Vectorization of quantum operations and its use," (2011), 10.48550/arXiv.0911.2539.

[93] I. Bengtsson and K. Życzkowski, *Geometry of Quantum States: An Introduction to Quantum Entanglement*, 2nd ed. (Cambridge University Press, 2017).

[94] V. Vorobyov, S. Zaiser, N. Abt, J. Meinel, D. Dasari, P. Neumann, and J. Wrachtrup, "Quantum Fourier transform for nanoscale quantum sensing," npj Quantum Information **7**, 124 (2021).

[95] D. Kribs, R. Laflamme, and D. Poulin, "Unified and generalized approach to quantum error correction," Phys. Rev. Lett. **94**, 180501 (2005).

[96] E. Knill, "On Protected Realizations of Quantum Information," Phys. Rev. A **74**, 042301 (2006).

[97] L.-M. Duan and G.-C. Guo, "Preserving coherence in quantum computation by pairing quantum bits," Phys. Rev. Lett. **79**, 1953 (1997).

[98] P. Zanardi and M. Rasetti, "Noiseless quantum codes," Phys. Rev. Lett. **79**, 3306 (1997).

[99] D. A. Lidar, I. L. Chuang, and K. B. Whaley, "Decoherence-free subspaces for quantum computation," Phys. Rev. Lett. **81**, 2594 (1998).

[100] R. Blume-Kohout, H. K. Ng, D. Poulin, and L. Viola, "Characterizing the structure of preserved information in quantum processes," Phys. Rev. Lett. **100**, 030501 (2008).

[101] L. Viola, E. Knill, and R. Laflamme, "Constructing Qubits in Physical Systems," J. Phys. A: Math. Gen. **34**, 7067–7079 (2001).

[102] W. Dür and H.-J. Briegel, "Entanglement purification for quantum computation," Phys. Rev. Lett. **90**, 067901 (2003).

[103] J.-M. Cai, W. Dür, M. V. den Nest, A. Miyake, and H. J. Briegel, "Quantum computation in correlation space and extremal entanglement," Phys. Rev. Lett. **103**, 050503 (2009).

[104] J. Cai, A. Miyake, W. Dür, and H. J. Briegel, "Universal quantum computer from a quantum magnet," Phys. Rev. A **82**, 052309 (2010).

[105] D. Gottesman, "Opportunities and Challenges in Fault-Tolerant Quantum Computation," (2022), 10.48550/arXiv.2210.15844.

[106] P. Zanardi, D. A. Lidar, and S. Lloyd, "Quantum Tensor Product Structures are Observable Induced," Phys. Rev. Lett. **92**, 060402 (2004).

[107] P. Zanardi, "Virtual Quantum Subsystems," Phys. Rev. Lett. **87**, 077901 (2001).

[108] L. Viola, H. Barnum, E. Knill, G. Ortiz, and R. Somma, "Entanglement beyond subsystems," in *Contemporary Mathematics*, Vol. 381, edited by D. Evans, J. J. Holt, C. Jones, K. Klintworth, B. Parshall, O. Pfister, and H. N. Ward (American Mathematical Society, Providence, Rhode Island, 2005) pp. 117–130.

[109] G. Ortiz, R. Somma, H. Barnum, E. Knill, and L. Viola, "Entanglement as an Observer-Dependent Concept: An Application to Quantum Phase Transitions," (2004), 10.48550/arXiv.quant-ph/0403043.

[110] S. M. Carroll and A. Singh, "Quantum Mereology: Factorizing Hilbert Space into Subsystems with Quasi-Classical Dynamics," Phys. Rev. A **103**, 022213 (2021).

[111] L.-A. Wu, D. Segal, and P. Brumer, "No-go theorem for ground state cooling given initial system-thermal bath factorization," Sci Rep **3**, 1824 (2013).

[112] F. Ticozzi and L. Viola, "Quantum resources for purification and cooling: Fundamental limits and opportunities," Sci Rep **4**, 5192 (2014).

[113] F. Ticozzi and L. Viola, "Quantum and classical resources for unitary design of open-system evolutions," Quantum Sci. Technol. **2**, 034001 (2017).

[114] P. Taranto, F. Bakhshinezhad, A. Bluhm, R. Silva, N. Friis, M. P. E. Lock, G. Vitagliano, F. C. Binder, T. Debarba, E. Schwarzhans, F. Clivaz, and M. Huber, "Landauer vs. Nernst: What is the True Cost of Cooling a Quantum System?" PRX Quantum **4**, 010332 (2023).

[115] A. E. Allahverdyan, K. V. Hovhannisyan, D. Janzing, and G. Mahler, "Thermodynamic limits of dynamic cooling," Phys. Rev. E **84**, 041109 (2011).

[116] D. Reeb and M. M. Wolf, "An improved Landauer principle with finite-size corrections," New Journal of Physics **16**, 103011 (2014).

[117] M. T. Mitchison, M. P. Woods, J. Prior, and M. Huber, "Coherence-assisted single-shot cooling by quantum absorption refrigerators," New J. Phys. **17**, 115013 (2015).

[118] P. Kaye, R. Laflamme, and M. Mosca, *An Introduction to Quantum Computing* (Oxford University Press, 2006).

[119] M. Ziman, P. Štelmachovič, V. Bužek, M. Hillery, V. Scarani, and N. Gisin, "Diluting quantum information: An analysis of information transfer in system-reservoir interactions," Phys. Rev. A **65**, 042105 (2002).

[120] F. Ciccarello, S. Lorenzo, V. Giovannetti, and G. M. Palma, "Quantum collision models: Open system dynamics from repeated interactions," Physics Reports **954**, 1–70 (2022).

[121] J. B. Brask and N. Brunner, "Small quantum absorption refrigerator in the transient regime: Time scales, enhanced cooling and entanglement," Phys. Rev. E **92**, 062101 (2015).

[122] L. A. Correa, J. P. Palao, G. Adesso, and D. Alonso, "Performance bound for quantum absorption refrigerators," Phys. Rev. E **87**, 042131 (2013).

[123] R. H. Dicke, "Coherence in Spontaneous Radiation Processes," Phys. Rev. **93**, 99–110 (1954).

[124] Y. K. Wang and F. T. Hioe, "Phase Transition in the Dicke Model of Superradiance," Phys. Rev. A **7**, 831–836 (1973).

[125] K. Hepp and E. H. Lieb, "Equilibrium Statistical Mechanics of Matter Interacting with the Quantized Radiation Field," Phys. Rev. A **8**, 2517–2525 (1973).

[126] P. Kirton, M. M. Roses, J. Keeling, and E. G. D. Torre, "Introduction to the Dicke model: from equilibrium to nonequilibrium, and vice versa," Adv. Quantum Technol. **2**, 1800043 (2018).

[127] K. Baumann, C. Guerlin, F. Brennecke, and T. Esslinger, "Dicke quantum phase transition with a superfluid gas in an optical cavity," Nature **464**, 1301–1306 (2010).

[128] K. Baumann, R. Mottl, F. Brennecke, and T. Esslinger, "Exploring Symmetry Breaking at the Dicke Quantum Phase Transition," Phys. Rev. Lett. **107**, 140402 (2011).

[129] P. Forn-Díaz, L. Lamata, E. Rico, J. Kono, and E. Solano, "Ultrastrong coupling regimes of light-matter interaction," Rev. Mod. Phys. **91**, 025005 (2019).

[130] A. Frisk Kockum, A. Miranowicz, S. De Liberato, S. Savasta, and F. Nori, "Ultrastrong coupling between light and matter," Nat. Rev. Phys. **1**, 19–40 (2019).

[131] J. Léonard, A. Morales, P. Zupancic, T. Esslinger, and T. Donner, "Supersolid formation in a quantum gas breaking a continuous translational symmetry," Nature **543**, 87–90 (2017).

[132] J. Léonard, A. Morales, P. Zupancic, T. Donner, and T. Esslinger, "Monitoring and manipulating Higgs and Goldstone modes in a supersolid quantum gas," Science (80-.). **358**, 1415–1418 (2017).

[133] F. Ferri, R. Rosa-Medina, F. Finger, N. Dogra, M. Soriente, O. Zilberberg, T. Donner, and T. Esslinger, "Emerging dissipative phases in a superradiant quantum gas with tunable decay," (2021).

[134] D. Nagy, G. Szirmai, and P. Domokos, "Critical exponent of a quantum-noise-driven phase transition: The open-system Dicke model," Phys. Rev. A **84**, 043637 (2011).

[135] B. Öztop, M. Bordyuh, Ö. E. Müstecaplıoğlu, and H. E. Türeci, "Excitations of optically driven atomic condensate in a cavity: theory of photodetection measurements," New J. Phys. **14**, 085011 (2012).

[136] E. G. D. Torre, S. Diehl, M. D. Lukin, S. Sachdev, and P. Strack, "Keldysh approach for nonequilibrium phase transitions in quantum optics: Beyond the Dicke model in optical cavities," Phys. Rev. A **87**, 023831 (2013).

[137] Q. Xie, H. Zhong, M. T. Batchelor, and C. Lee, "The quantum Rabi model: solution and dynamics," J. Phys. A Math. Theor. **50**, 113001 (2017).

[138] M.-L. Cai, Z.-D. Liu, W.-D. Zhao, Y.-K. Wu, Q.-X. Mei, Y. Jiang, L. He, X. Zhang, Z.-C. Zhou, and L.-M. Duan, "Observation of a quantum phase transition in the quantum Rabi model with a single trapped ion," Nat. Commun. **12**, 1126 (2021).

[139] C. Emary and T. Brandes, "Chaos and the Quantum Phase Transition in the Dicke Model," Phys. Rev. E **67**, 22 (2003).

[140] A. Klein and E. R. Marshalek, "Boson realizations of Lie algebras with applications to nuclear physics," Rev. Mod. Phys. **63**, 375–558 (1991).

[141] L. Hackl, T. Guaita, T. Shi, J. Haegeman, E. Demler, and I. Cirac, "Geometry of variational methods: dynamics of closed quantum systems," SciPost Phys. **9**, 048 (2020).

[142] A. Serafini, *Quantum Continuous Variables* (CRC Press, Boca Raton, FL, 2017).

[143] C. Weedbrook, S. Pirandola, R. García-Patrón, N. J. Cerf, T. C. Ralph, J. H. Shapiro, and S. Lloyd, "Gaussian quantum information," Rev. Mod. Phys. **84**, 621–669 (2012).

[144] G. Adesso, S. Ragy, and A. R. Lee, "Continuous Variable Quantum Information: Gaussian States and Beyond," Open Syst. Inf. Dyn. **21**, 1440001 (2014).

[145] D. Rossini and E. Vicari, "Coherent and dissipative dynamics at quantum phase transitions," (2021).

[146] M. Soriente, T. Donner, R. Chitra, and O. Zilberberg, "Dissipation-induced anomalous multicritical phenomena," Phys. Rev. Lett. **120**, 183603 (2017).

[147] M. Soriente, R. Chitra, and O. Zilberberg, "Distinguishing phases using the dynamical response of driven-dissipative light-matter systems," Phys. Rev. A **101**, 023823 (2020).

[148] F. Carollo and I. Lesanovsky, "Exactness of Mean-Field Equations for Open Dicke Models with an Application to Pattern Retrieval Dynamics," Phys. Rev. Lett. **126**, 230601 (2021).

[149] M. Boneberg, I. Lesanovsky, and F. Carollo, "Quantum fluctuations and correlations in open quantum Dicke models," Phys. Rev. A **106**, 012212 (2022).

[150] T. F. Havel, "Procedures for Converting among Lindblad, Kraus and Matrix Representations of Quantum Dynamical Semigroups," J. Math. Phys. **44**, 534 (2003).

[151] C. J. Wood, J. D. Biamonte, and D. G. Cory, "Tensor networks and graphical calculus for open quantum systems," (2015), 10.48550/arXiv.1111.6950.

[152] P. N. J. Beck, M. Steiner, F. Rempp, H. Fedder, P. R. Hemmer, J. Wrachtrup, and F. Jelezko, "Single-shot readout of a single nuclear spin," Science **329**, 542 (2010).

[153] S. Machnes, U. Sander, S. J. Glaser, P. de Fouquières, A. Gruslys, S. Schirmer, and T. Schulte-Herbrüggen, "Comparing, optimizing, and benchmarking quantum-control algorithms in a unifying programming framework," Phys. Rev. A **84**, 022305 (2011).

[154] G. Waldherr, Y. Wang, S. Zaiser, M. Jamali, T. Schulte-Herbrueggen, H. Abe, T. Ohshima, J. Isoya, P. Neumann, and J. Wrachtrup, "Quantum error correction in a solid-state hybrid spin register," Nature **506**, 204–207 (2014).

[155] E. Bianchi, L. Hackl, and N. Yokomizo, "Entanglement entropy of squeezed vacua on a lattice," Phys. Rev. D **92**, 1–20 (2015).

Ausführliche deutsche Zusammenfassung

Hintergrund und Motivation

Die Vorbereitung reiner Zustände ist von entscheidender Bedeutung, um Quantentechnologien funktionsfähig zu machen, insbesondere für Quantencomputer [1–3]. Eine hochgenaue Initialisierung eines Mehrqubit-Registers auf den Rechenzustand $|00\ldots0\rangle$ ist der erste Schritt zur Berechnung und wichtig genug, um als einer der Hauptantriebe für den Bau von Quantencomputern in großem Maßstab eingestuft zu werden, wie beispielsweise im zweiten Kriterium von DiVincenzo zusammengefasst [1]. Diese Bemühungen gehen einher mit der Entwicklung von Berechnungen, die fern von fehlerinduzierenden Dynamiken in decoherence-free subspace [4–7] oder innerhalb von noiseless subsystem [8–10] stattfinden, und zusätzlich zur aktiven Implementierung von quantenfehlerkorrigierenden Maßnahmen [11, 12].

In DiVincenzos Kriterien [1] und den anschließenden Charakterisierungen [3] wird die Kühlung in verschiedenen Formen explizit als haupt-

sächlicher Ansatz für das Target der Erzeugung von niederentropischen Referenzzuständen erwähnt. Die Kälteerzeugung bildet somit die Basis für die Durchführung von Experimenten im Allgemeinen. Wir erkennen nun ihre Notwendigkeit in modernen Spitzentechnologien und bemerken ihre Präsenz im Streben nach präziseren Uhren [13], der Vorbereitung kalter und ultrakalter Vielteilchenzustände für Simulationen oder andere Anwendungen in der präzisen Steuerung und Messung von Quantenzuständen [14–19].

Eine Quantenkühlmaschine, die in besonderem Zusammenhang zur Entwicklung von Quantencomputern steht, ist der algorithmische Kühler. Gleichzeitig kann er als eine Art von quantenmechanischer Wärmemaschine betrachtet werden, die jedoch intrinsisch ein algorithmisches Verfahren ist und somit in gewisser Weise eine eigene Berechnungsaufgabe darstellt. Darüber hinaus ist er experimentell realisierbar [22, 23].

Ursprünglich im Zusammenhang mit dem Vorschlag zur Ensemble-Quantenberechnung mittels Kernmagnetischer Resonanz (NMR) vorgeschlagen [20–22], zielte der algorithmische Kühlmaschine darauf ab, ein effektives niedrigdimensionales quantenmechanisches Teilsystem aus dem großen thermischen Zustand zu erzeugen. Dieses sollte dem Grundzustand näher kommen und für Quantenberechnungsaufgaben geeignet sein. Später wurde erkannt, dass für diesen Ansatz eine ausreichend große Menge dieser effektiven Qubits bei niedrigen Temperaturen erforderlich wäre und diese von Dekohärenzeffekten ferngehalten werden müssten.

Fehlertoleranzschätzungen setzten dieser Methode erhebliche Grenzen und waren ein Hindernis. Die Fähigkeit, Mehrqubit-Register laufend zu kühlen, schien vielversprechender zu sein, wie später gezeigt wurde [24, 25]. In dieser Methode, genannt Heat-Bath Algorithmic Cooling (HBAC), erfolgt die Kühlung über einen Zyklus von Operationen unter

Einbeziehung einer separaten Umgebung. Die berechneten Qubits sind das Target eines unitären Gatters, bei dem ebenfalls Qubits aus dem Wärmebad als Eingabe verwendet werden, die jedoch für den nächsten Zyklus verworfen werden. In diesem Sinne findet die Kühlung des Ziels im Kontext eines offenen Quantensystems statt. Dies steht im Gegensatz zum ursprünglichen Vorschlag, bei dem auf die Kühlung des Großteils des Ensembles von Qubits (z.B. das flüssige NMR-Ensemble) eine unitäre Operation folgt, die das Target Qubit initialisiert.

In den folgenden Abschnitten werden wir uns von der Fokussierung auf die Steuerung von Quantensystemen abwenden und einen autonomen Quantenkühler in Betracht ziehen [28–31]. Im Gegensatz zur Gestaltung von kontrollierten Systemen wie HBAC entwickelt und führt ein Absorptionskühler autonom Kühlung auf einem kalten Wärmebad durch, frei von externen Interaktionen abgesehen von denen, die für die Einrichtung der Plattform erforderlich sind. Die ersten Entwürfe einer Absorptionskühlmaschines stammen aus dem 19. Jahrhundert, und eine bemerkenswerte Verbesserung geht auf Einstein und Szilárd zurück, für eine Absorptionskühlmaschine ohne bewegliche Teile [32], sowie später in den Referenzen [33–35], die frühe Beiträge zur Quantenthermodynamik darstellen. Das Arbeitsprinzip eines solchen Systems beruht auf dem Austausch einer Arbeitsquelle (der externen Steuervorrichtung, wie beispielsweise einem Regler in der Hand des Experimentators, der einen Laser abstimmt) gegen ein drittes Wärmebad, das zusätzlich zum kalten Bad platziert wird und von dem die Wärme extrahiert wird, sowie dem heißen Bad, wohin diese Wärme übertragen wird. Dieses zusätzliche Wärmebad, genannt der Arbeitsreservoir, das in der Regel bei einer noch höheren Temperatur als das heiße Bad sitzt, wird verwendet, da das System den kalten-zu-heißen Wärmetransport induziert, indem dieser Prozess mit einem gleichzeitigen Transport von Wärme vom

Arbeitsreservoir zum heißen Bad gekoppelt wird. Die Motivation, mit autonomen Systemen zu arbeiten, insbesondere Kühlern, besteht darin, eine bessere Berechnung der thermodynamischen Kosten dieser Geräte zu liefern und bewegliche Teile in der Konstruktion dieser Geräte zu verwerfen, die genau die Quellen für Rauschen und Fehler darstellen, da sie je kleiner sie gemacht werden, Fluktuationen immer stärker ausgesetzt sind.

Gliederung der Dissertation. Wir beginnen mit Kapitel 1, in der wir recht allgemeine Kühlungsgrenzen beschreiben und uns auf eine spezielle Implementierung des algorithmischen Kühlers konzentrieren, bekannt als Heat-Bath Algorithmic Cooling (HBAC). Algorithmisches Kühlen ist eine besonders minimale Implementierung eines Kühlers, die es ermöglicht, viele steuerbare Parameter zu verfolgen, während sie auf Qubits wirkt. Da es ursprünglich in Bezug auf Zwei-Niveau-Systeme definiert wurde, eignet es sich für Studien zur Quantenzustandsvorbereitung und betont seine Nützlichkeit für Quantencomputer und verwandte Technologien. In diesem ersten Kapitel führen wir eine thermodynamische Analyse von HBAC durch, die umfassender ist als das, was in der Vergangenheit getan wurde [37], und zusätzlich zu einer tatsächlichen experimentellen Implementierung seiner minimalen Version in einer NV-Zentren.

In Kapitel 2 erweitern wir diese Beschreibung und enthüllen die virtuelle Qubit-Natur der Ressourcen, die zur Kühlung des Target-Qubits im algorithmischen Kühlen verwendet werden. Mit diesem Verständnis schlagen wir vor, wie echte quantenmechanische Ressourcen einzubeziehen sind, und wir schlagen ein konservatives Verfahren vor, um diese Ressourcen zu nutzen, um das Zielsystem noch näher an den Grundzustand zu bringen. Dadurch zeigen wir auf, wie die ursprüngliche Idee der zuvor vorgeschlagenen universellen Kühlungsgrenzen umgangen werden kann.

Abschließend richten wir in Kapitel 3 unseren Fokus auf die komplexere Plattform der wechselwirkenden Spin-Boson-Systeme, in denen kollektives Verhalten, Phasen von Materie und Vielteilchenphysik wesentliche Konzepte sind. Das etablierte Dicke-Modell, das oft in der Quantenoptik und Atomphysik nützlich ist [40–42], dient uns zur Untersuchung der Gleichgewichtseigenschaften eines Systems, das für das Design des Absorptionskühlers geeignet ist. Das Dicke-Modell besteht ursprünglich aus einer großen Anzahl von d-Niveau-Systemen, die kollektiv mit einem einzelnen bosonischen Mode gekoppelt sind. Wir analysieren eine Erweiterung davon, die einen neuen bosonischen Mode einschließt, der mit einem neuen Freiheitsgrad der bereits vorhandenen d-Niveau-Systeme gekoppelt ist. Im thermodynamischen Grenzfall zeigen wir, dass die kollektive Kopplung in einem Mittelwert-Feld-Ansatz zu einem System von drei wechselwirkenden harmonischen Oszillatoren vereinfacht werden kann. Dieses erweiterte Modell weist dieselben Eigenschaften im Gleichgewicht auf wie das ursprüngliche Modell, nun mit zwei unabhängigen normal-zu-superradianten Phasenübergängen. Darüber hinaus zeigen wir, dass die Region, die die beiden superradiant Phasen trennt, eine kontinuierliche Symmetrie bricht und somit einen lückenlos Goldstone-Mode hervorruft. Wir schließen mit der Entwicklung eines Korrelationsprofils des Systems im Gleichgewicht, in dem multipartite Verschränkung vorhanden ist.

List of Publications

- *Soldati, R. R.*, Dasari, D. B., Wrachtrup, J., & Lutz, E. (2023). Cooling advantage of coherent virtual qubits. **Manuscript under review**.

- *Soldati, R. R.*, Dasari, D. B., Wrachtrup, J., & Lutz, E. (2022). Thermodynamics of a minimal algorithmic cooling refrigerator. **Physical Review Letters, 129(3), 030601.** [quant-ph:2109.14056].

- *Soldati, R. R.*, Mitchison, M. T., & Landi, G. T. (2021). Multipartite quantum correlations in a two-mode Dicke model. **Physical Review A, 104(5), 052423.** [quant-ph:2105.09260].

- *Soldati, R. R.*, Menicucci, L. S., & Yokomizo, N. (2021). Universal terms of the entanglement entropy in a static closed universe. **Physical Review D, 104(12), 125016.** [hep-th:2106.06803].

- da Paz, I. G., *Soldati, R.*, Cabral, L. A., de Oliveira Jr, J. G. G., & Sampaio, M. (2016). Poisson's spot and Gouy phase. **Physical Review A, 94(6), 063609.** [quant-ph:1609.09023].

Curriculum Vitae

Rodolfo Reis Soldati

▬▬▬ Personal details

○ Date of birth: 12/01/1995.
○ Place of birth: Juiz de Fora, Minas Gerais, Brazil.

▬▬▬ Education

2019 – present **Ph.D. (CNPq/DAAD fellow) – Advisors: Prof. Gabriel Landi, Prof. Eric Lutz**, Universidade de São Paulo, IFUSP, Universität Stuttgart, ITP1
Thesis. *Quantum Cooling: Thermodynamics and Information.*

2017 – 2018 **M.Sc. Physics (CNPq fellow) – Advisor: Prof. Nelson Yokomizo**, Universidade Federal de Minas Gerais, ICEx, Belo Horizonte, MG, Brazil
Dissertation. Entanglement entropy in quantum field theory.

2014 – 2015 **Visiting student – Theoretical Physics**, Durham University, Durham, UK
Awarded with the Science Without Borders scholarship.

2013 – 2016 **B.Sc. Physics**, Universidade Federal de Minas Gerais, ICEx, Belo Horizonte, MG, Brazil

▬▬▬ Teaching

2023 Summer	Teaching Assistant.	University of Stuttgart.	Classical Mechanics.
2022/23 Winter	Teaching Assistant.	University of Stuttgart.	Mathematical Methods of Physics 1.
2022 Summer	Teaching Assistant.	University of Stuttgart.	Electrodynamics.
2021/22 Winter	Teaching Assistant.	University of Stuttgart.	Mathematical Methods of Physics 1.
2020.1	Teaching Assistant.	University of São Paulo.	Physics 1, Classical Mechanics.

▬▬▬ Events and presentations

July 2023	Quantum Thermodynamics Conference 2023	Vienna, Austria	Poster on "Cooling advantage of coherent virtual qubits."
Sep 2022	Qalypso Summer School on Quantum Computation & Open Quantum Systems	Gozo, Malta	Poster and short talk on "Thermodynamics of a minimal algorithmic cooling refrigerator."

Jul 2022	Entropy and the Second Law of Thermodynamics	WE-Heraeus-Seminar 761	Poster on "Thermodynamics of a minimal algorithmic cooling refrigerator."
Jun 2022	Quantum Thermodynamics Conference 2022	QUB/Online	Poster on "Thermodynamics of a minimal algorithmic cooling refrigerator."
Aug 2021	Quantum Thermodynamics Summer School	SwissMap	Poster on "Multipartite quantum correlations in a two-mode Dicke model."
Sep/Oct 2019	Predoc School on Interaction of Light with Cold Atoms	Les Houches	Poster on "Symmetry Breaking in a U(1) Dicke model."
Nov 2018	Workshop Physics in the Department	UFMG, Brazil	Talk delivered on "Universal terms of the entanglement entropy in Einstein space."
Nov 2017	Workshop Physics in the Department	UFMG, Brazil	Talk delivered on "Quantum correlations for scalar field in closed spacetime."
Mar 2016	II Workshop on Quantum Field Theory and Quantum Optics	UESC, Brazil	Talk delivered on "Poisson spot with matter waves."

Eidesstattliche Erklärung

Ich versichere, die vorliegende Arbeit selbstständig und lediglich unter Benutzung der angegebenen Quellen und Hilfsmittel verfasst zu haben. Ich erkläre weiterhin, dass die vorliegende Arbeit noch nicht im Rahmen eines anderen Prüfungsverfahrens eingereicht wurde.

Rodolfo Reis Soldati   Stuttgart, 21. August 2023